Doklady Physics, Vol. 50, No. 9, 2005, pp. 431–433. Translated from Doklady Akademii Nauk, Vol. 404, No. 3, 2005, pp. 326–328.
Original Russian Text Copyright © 2005 by Golub, Aksenov, Baklanov, Volodin, Golovastov, Gubin, Efremov, Savel'ev, Fortov, Sharov.

PHYSICS

Effect of Magnetic Field on the Detonation Initiation by Spark Discharge in Hydrogen–Air Mixture

V. V. Golub*, V. S. Aksenov, D. I. Baklanov*, V. V. Volodin*, S. V. Golovastov*, S. A. Gubin**, V. P. Efremov*, A. S. Savel'ev*, Academician V. E. Fortov*, and Yu. L. Sharov***

Received June 2, 2005

In this paper, we have experimentally studied the effect of magnetic field on the detonation initiation by spark discharge in hydrogen–air mixture. We have shown that the magnetic field imposed on the discharge region affects the shock-wave intensity so that the predetonation distance is reduced by a factor of 5 when the magnetic induction attains 1.5 T.

It is well known that electric discharge is the most propagated method for the ignition of combustible mixtures. The characteristic feature of streamer and arc discharges is the existence of a narrow channel in which breakdown occurs and electric current flows. Gas in the channel is heated up to temperatures of tens thousands of Kelvin, which exceeds by more than an order of magnitude the temperature required for the inflammation of a gas mixture. In addition, as a result of rapidly heating and expanding gas in a channel, a shock wave is formed. This shock wave also is capable of heating the gas mixture up to the inflammation temperature, which eventually leads to the detonation initiation. The parameters of the shock wave are dependent on those of the electric discharge, in particular, on the amplitude and rise time of the electric current, i.e., on its power. Magnetic field significantly affects the electric discharge. The effect of external physical fields on the combustion and explosion of combustible mixtures represents an urgent problem of modern physics [1]. The action of electric fields on burning gases has been thoroughly investigated and is for the most part understood. However, to date, the action of magnetic and electromagnetic fields has not been exhaustively clarified.

The goal of this study is to improve the efficiency of the detonation initiation by increasing the region of the igniting discharge and, thereby, increasing the volume of gas participating in the initiation.

The effect of the initial parameters of the electric discharge on the length of the pre-detonation segment in a hydrogen–air mixture at a pressure of 1 atm and temperature of 20°C was investigated in a cylindrical detonation combustion chamber (cylindrical DCC) 2510 mm in length and 83 mm in internal diameter. The DCC was preliminary evacuated and then filled with the stoichiometric hydrogen–air mixture up to the atmospheric pressure. A spark discharger was positioned at distances of 40 and 175 mm from the DCC lateral surface and DCC end, respectively. The energy that had been accumulated in an electric capacitor and was then transferred to the spark discharger varied within the limits of 0.20 to 1.56 kJ. The energy-release time attained 20 μs. The propagation velocity of shock waves in the DCC and the velocity of the flame-front motion were measured by RSV-113A34 pressure sensors and FD-256 photodetectors, respectively. The measured shock-wave velocity was normalized to the steady-state velocity D_{CJ} of the one-dimensional detonation. This was realized according to the Chapman–Jouguet model based on the equilibrate composition of combustion products beyond the flame front at a given temperature and density of the substance. In the hydrogen–air mixture, $D_{CJ} = 1968$ m s^{-1} at a pressure of 1 atm and temperature of 20°C. We have found that two scenarios of the detonation formation are possible at the shock-wave initial velocity $0.7D_{CJ}$ (Fig. 1).

(a) At a distance of 5–7 DCC calibers, the steady-state detonation with Chapman–Jouguet parameters is formed;

(b) at a distance of 6 DCC calibers, the retardation of the shock-wave front occurs, which is accompanied by the consequent acceleration up to $0.55D_{CJ}$ at a distance of 25 DCC calibers (the length of the DCC measurement section).

At an initial shock-wave velocity higher than $0.7\ D_{CJ}$, the detonation is developed in accordance with the first scenario. In this case, the energy release back of the shock wave exceeds the work spent by the shock wave for gas compression. At an initial shock-wave

* *Institute of Thermal Physics of Extreme States, Joint Institute of High Temperatures, Russian Academy of Sciences, Izhorskaya ul. 13/19, Moscow, 125412 Russia*

e-mail: golub@ihed.ras.ru; golovastov@yandex.ru; fortov@ras.ru

** *Moscow Engineering Physics Institute (State University), Kashirskoe sh. 31, Moscow, 115409 Russia*

1028-3358/05/5009-0431$26.00 © 2005 Pleiades Publishing, Inc.

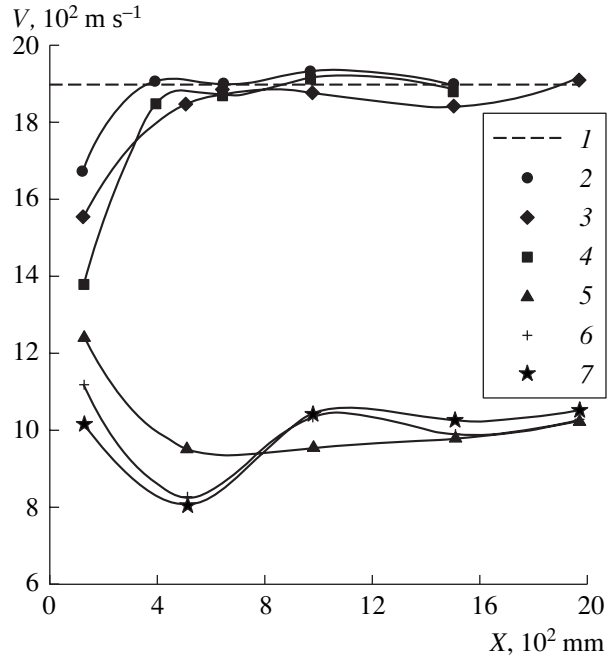

Fig. 1. Effect of the velocity V of the primary shock wave on the transition of deflagration to detonation in the hydrogen–air mixture: (*1*) Chapman–Jouguet detonation velocity, V = (*2*) 1670, (*3*) 1582, (*4*) 1380, (*5*) 1243, (*6*) 1115, and (*7*) 1017 m s^{-1}.

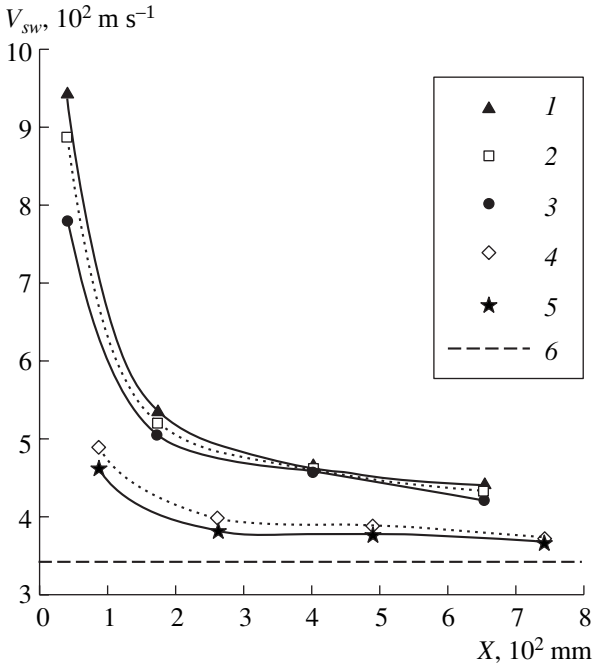

Fig. 2. Distribution of the shock-wave velocity along the axis of the detonation combustion chamber (DCC). (*1*) E = 900 J, B = 1.5 T; (*2*) E = 900 J, B = 1.5 T; (*3*) E = 900 J, B = –1.5 T; (*4*) E = 200 J, B = 1.5 T; (*5*) E = 200 J, B = 0; (*6*) sonic velocity.

velocity lower than $0.7D_{CJ}$, the detonation is developed in accordance with the second scenario. In this case, the chemical energy released in the process of burning a combustible mixture does not compensate the work spent for compression. The intensity of the shock wave drops until the compression work being accomplished by the shock wave becomes lower than the chemical energy released in the combustion process.

The effect of magnetic field on the plasma region formed by the electric discharge was investigated in two steps. At the first step, the spark discharge in air at atmospheric pressure was visualized by the Foucault–Maksutov method [2] based on the light refraction by the density gradient (with application of the knife-and-slit method) in the case of the simultaneous initiation of two dischargers. One of them was subjected to the action of magnetic field produced by the same discharge electric current in a conductor situated close to the discharge gap. It was found that the presence of the magnetic field increased the size of the plasma region near the discharge gap, and the shock-wave velocity at the initial stage was elevated by 10%.

At the second step, the investigation of the effect of the magnetic field on the electric discharge was carried out in the above-described DCC. The magnetic field was produced by two induction coils installed outside the DCC at two sides from the spark discharger, the energy accumulated having been 6 or 3 kJ. The electric energy accumulated and transferred to the spark discharger varied from 0.20 to 1.56 kJ. The electrodes of the spark-discharger inside the DCC had been installed in a position such that the direction of the discharge current was perpendicular to the magnetic field. This ensured the maximum effect of the magnetic field on the discharge current. The results obtained are presented in Fig. 2.

The calculation according to the Biot–Savart–Laplace formula has shown that under the given conditions when the directions of the external (induction coils outside the DCC) and proper (magnetic induction of the spark current) magnetic fields coincide with each other, the magnetic induction inside the discharger increased from 2 to 2.7 T, whereas for their opposite directions, the induction decreased from 2 to 1.3 T.

An effect was also found of the magnetic field on the intensity of the shock wave arising in the DCC as a result of the discharge in air. For coincident and opposite directions of the external magnetic field and of the proper magnetic field of the spark discharger, the shock-wave velocity increased by 50 m s^{-1} and decreased by 100 m s^{-1}, respectively (Fig. 2).

At the third step, we studied an effect of the magnetic field on the length of the pre-detonation segment in the hydrogen–air mixture at a pressure of 1 atm in the case when the electric energy transferred to the spark discharger equaled 0.9 kJ (Fig. 3). Switching on the external magnetic field (measured magnetic induction of 1.5 T) whose direction coincided with the direction

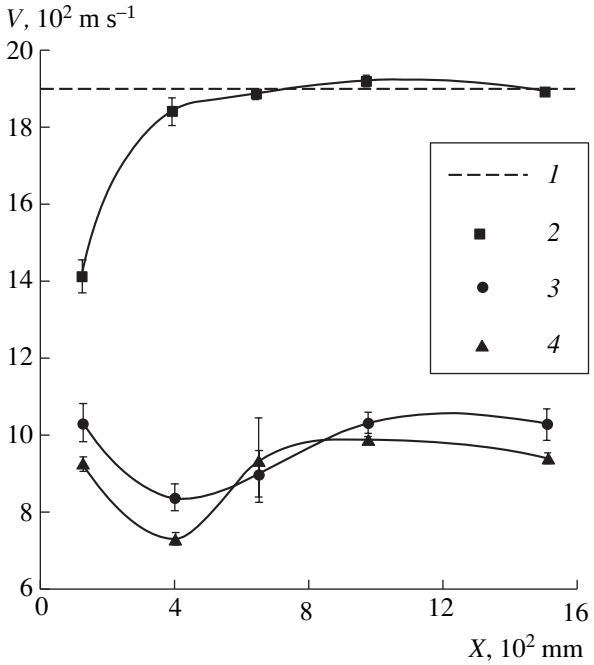

Fig. 3. Effect of external magnetic field on the velocity of a shock wave induced by electric discharge in a hydrogen–air mixture and on the process of passage from deflagration to detonation: (*1*) Chapman–Jouguet detonation velocity; B = (*2*) 1.5 T; (*3*) 0; and (*4*) –1.5 T.

of the proper magnetic field generated by the spark discharger, the formation of the over-compressed detonation was observed at a distance of 8 calibers. In this case, sensors installed at a distance of 9 calibers from the discharger fixed no delay of the flame front the shock wave. At the same time, in the absence of magnetic field, the primary shock wave initially weakened and then in 7 calibers from the ignition point began to rise again. However, in the DCC of 30 calibers in length, the flame front retarded from the shock wave by approximately 100 μs so that the detonation formation failed. Variation of the direction of the magnetic induction for the opposite one resulted in the lowering of the velocity of the primary shock wave by 100 m s^{-1}.

Thus, we have managed to demonstrate that magnetic field imposed on the discharge region affects the shock-wave intensity and, for a magnetic induction of 1.5 T, the pre-detonation distance is reduced by not less than 5 times. The effect discovered makes it possible to both enhance the efficiency and reduce the size of promising devices that utilize detonation combustion of fuels [3].

ACKNOWLEDGMENTS

We are grateful to B. Yankovskiĭ for fruitful discussion of the results of this study and to the Foundation of the Max Planck Award Cooperation Research Project “Physics of High Energy-Density Plasmas.”

REFERENCES

1. *Advanced Combustion Methods*, Ed. by F. J. Weinberger (Academic, New York, 1986).
2. L. A. Vasil’ev, *Schlieren Methods* (Nauka, Moscow, 1968; Israel Program for Scientific Translations, Jerusalem, 1971).
3. V. V. Golub, in *Proceedings of the 23rd International Symposium on Shock Waves, Arlington, USA, 2001* (Arlington, 2001).

Translated by G. Merzon

Doklady Physics, Vol. 50, No. 9, 2005, pp. 434–437. Translated from Doklady Akademii Nauk, Vol. 404, No. 3, 2005, pp. 329–332.
Original Russian Text Copyright © 2005 by Kaplun, Meshalkin.

PHYSICS

Behavior of the Heat Capacity C_V at the Liquid–Vapor Critical Point and in the Two-Phase Region of a Thermodynamic System

A. B. Kaplun and A. B. Meshalkin

Presented by Academician V.P. Skripov January 12, 2005

Received February 15, 2005

Among standard thermodynamic characteristics of a single-component substance in its liquid or gaseous state, the behavior of the specific heat at a constant volume (C_V) is apparently of most interest. At present, there is almost no doubt that C_V exhibits divergence at the critical point of the phase diagram, since both experimental data and theoretical models (see, e.g., [1–3]) present unambiguous evidence that the value of C_V tends to infinity upon approaching the critical point. Of course, physical quantities never reach infinite values in experiment, and the application of laws, established within the framework of theoretical models, to actual systems always implies a certain approximation. In this context, there have been continuous attempts to determine the behavior of the specific heat at a constant volume at the critical point proceeding from the so-called "first principles" based on well-established experimental facts. One recent example is offered by a series of papers by Novikov [4–6], where the divergence of C_V and some other physical quantities at a given critical point has been described within the framework of phenomenological thermodynamics, proceeding from considerations of system stability. The complexity of the theoretical analysis of the behavior of thermodynamic functions in the vicinity of a given critical point is related, in particular, to the fact that the application of the differential equations of thermodynamics to a system in this region of states leads to the appearance of indeterminacies of the 0/0 or ∞/∞ types. This problem has been considered in more detail, in particular, in monograph [7].

This paper presents an attempt to analyze the behavior of C_V at a critical point and in the two-phase region of the phase diagram of a single-component system, proceeding from rigorous differential equations of the phenomenological thermodynamics and from experimental facts that have been reliably established for such regions.

Institute of Thermophysics, Siberian Division, Russian Academy of Sciences, Novosibirsk, Russia

Let us consider the behavior of a thermodynamic system with continuously varying state parameters, assuming that the thermodynamic surface of states exhibits no jumps or discontinuities [8]. At the critical point corresponding to the liquid–vapor phase transition, the first two derivatives of the pressure with respect to volume at a constant temperature vanish by definition:

$$\left(\frac{\partial P}{\partial V}\right)_T^c = \left(\frac{\partial^2 P}{\partial V^2}\right)_T^c = 0. \quad (1)$$

We may regard it as a reliably established fact that the next two derivatives of the pressure with respect to volume at a constant temperature vanish as well:

$$\left(\frac{\partial^3 P}{\partial V^3}\right)_T^c = \left(\frac{\partial^4 P}{\partial V^4}\right)_T^c = 0. \quad (2)$$

Relations (2) were obtained by Novikov (see, e.g., [4]) proceeding from considerations of system stability. The same conclusion follows from an analysis of the equations of the fluctuational theory of phase transitions (the hypothesis of scaling invariance).

In the subsequent analysis of critical phenomena, it is implied that the number of independent coupling relations such as Eqs. (1) and (2) for the equation of state $F(P, V, T; a, b, c, \ldots) = 0$ does not exceed the number of coefficients $a, b, c, \ldots$ entering into this equation.

In order to analyze the behavior of the specific heat at a constant volume at a critical point, let us use the well-known relation for C_V (see, e.g., [9]),

$$C_V = \left(\frac{\partial U}{\partial T}\right)_V = \left(\frac{\partial U}{\partial T}\right)_P - \left(\frac{\partial U}{\partial V}\right)_T \left(\frac{\partial V}{\partial T}\right)_P \quad (3)$$

and perform simple transformations to express C_V as

$$C_V = \left(\frac{\partial P}{\partial T}\right)_V \frac{\left(\frac{\partial U}{\partial V}\right)_T - \left(\frac{\partial U}{\partial V}\right)_P}{\left(\frac{\partial P}{\partial V}\right)_T}, \quad (4)$$

1028-3358/05/5009-0434$26.00 © 2005 Pleiades Publishing, Inc.

where U is the internal energy, T is the absolute temperature, P is pressure, and V is volume. In Eq. (4), the internal energy U in the derivative $\left(\frac{\partial U}{\partial V}\right)_T$ is the function of the independent variables T and V, while in the partial derivative $\left(\frac{\partial U}{\partial V}\right)_P$, this energy is a function of the independent variables P and V.

At the liquid–vapor critical point, the first derivative of the pressure with respect to volume at a constant temperature vanishes, whereas the derivative $\left(\frac{\partial P}{\partial T}\right)_T^c$ has a finite value. If the numerator in Eq. (4) at the critical point also vanishes,

$$\left(\frac{\partial U}{\partial V}\right)_T^c - \left(\frac{\partial U}{\partial V}\right)_P^c = 0, \quad (5)$$

there appears an indeterminacy of the 0/0 type that has to be eliminated, for example, using the L'Hospital rule. This situation can also arise with the higher derivatives, since the derivatives up to the fourth order in the denominator of expression (4) vanish in accordance with Eqs. (1) and (2).

In the general case, the internal energy and its partial derivatives are the functions of two independent variables. Let us consider the behavior of the partial derivative of U with respect to volume at a constant temperature on the critical isotherm $U_1 = U(T_c, V)$ and the behavior of the partial derivative with respect to volume at a constant pressure on the critical isobaric line $U_2 = U(P_c, V)$. In this case, both $U_1 = U(T_c, V)$ and $U_2 = U(T_c, V)$ are the functions of only one variable, namely, the volume (or the density), and the values of T_c and P_c in equations for the internal energy play the role of parameters. Since there are only two independent variables, the relation $U_1^c = U_2^c$ is obviously valid at the critical point. It is also evident that the total derivatives on the isolines at the critical point are equal to the corresponding partial derivatives for the corresponding constants:

$$\left.\frac{d^n U_1}{dV^n}\right|_{V=V_c} = \left(\frac{\partial^n U}{\partial V^n}\right)_T^c, \quad \left.\frac{d^n U_2}{dV^n}\right|_{V=V_c} = \left(\frac{\partial^n U}{\partial V^n}\right)_P^c. \quad (6)$$

We now analyze the behavior of the function $\psi(V)$ defined as the difference of the internal energies on the isotherm and isobar,

$$\psi(V) = U_1(V) - U_2(V), \quad (7)$$

which is also a function of only one variable. Using this function and its derivatives

$$\frac{\partial \psi(V)}{dV} = \frac{dU_1(V)}{dV} - \frac{dU_2(V)}{dV},$$
$$\cdots, \quad (8)$$
$$\frac{d^n \psi(V)}{dV^n} = \frac{d^n U_1(V)}{dV^n} - \frac{d^n U_2(V)}{dV^n},$$

we can try to eliminate the indeterminacy in expression (4) using the L'Hospital rule for the function of one variable.

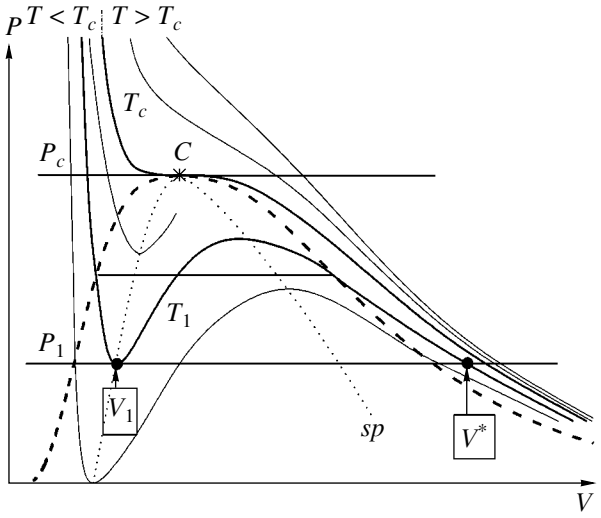

Pressure P as a function of the volume V for a single-component substance at various temperatures T (see the text for explanations).

The behavior of the function $\psi(V) = U_1(V) - U_2(V)$ is elucidated by an analysis of the phase diagram P versus V for a single-component substance (Fig. 1). For any arbitrarily set volume below the critical one ($V < V_c$), the temperature on the critical isobar is always below the critical temperature, whereas for $V > V_c$, the temperature on this isobar is always above the critical value. By virtue of the positive definiteness of C_V (at least, outside the spinodal), the internal energy increases with the temperature. From this it follows that the function $\psi(V)$ defined by formula (7) is positive for $V < V_c$, negative for $V > V_c$, and is zero at $V = V_c$. In other words, the critical point is the point of intersection of the critical isobar and critical isotherm of the internal energy.

In this analysis of the behavior of the function $\psi(V)$ at the critical point, we should take into account certain well-known mathematical statements [10]: if the order of the first nonzero derivative at a given point is even, the function exhibits a maximum at this point; if the order of the first nonzero derivative is odd, the given point is a bending point. Since, according to the above

considerations, the function $\psi(V)$ cannot have a maximum at the critical point, the first case is ruled out.

As is known [1–7], the ratio of the heat capacities $\frac{C_V^c}{C_P^c}$ at the critical point is zero. Then, taking into account the relations

$$C_P = \left(\frac{\partial H}{\partial T}\right)_P = \left(\frac{\partial H}{\partial V}\right)_P\left(\frac{\partial V}{\partial T}\right)_P = -\left(\frac{\partial H}{\partial V}\right)_P\frac{(\partial P/\partial H)_V}{(\partial P/\partial V)_T}$$

(where H is the enthalpy) and using expression (4), we obtain

$$\left(\frac{C_V}{C_P}\right)^c = -\frac{\left(\frac{\partial U}{\partial V}\right)_T^c - \left(\frac{\partial U}{\partial V}\right)_P^c}{\left(\frac{\partial H}{\partial V}\right)_P^c} = 0. \quad (9)$$

Using certain well-known differential equations of thermodynamics, it can be readily shown that, if condition (9) is valid, the derivative $\left(\frac{\partial H}{\partial V}\right)_P^c$ at the critical point is finite and positive. From this it follows that the numerator in Eq. (9) at the critical point vanishes,

$$\left(\frac{\partial U}{\partial V}\right)_T^c - \left(\frac{\partial U}{\partial V}\right)_P^c = 0 \quad (10)$$

and, hence,

$$\left.\frac{d\psi(V)}{dV}\right|^c = \frac{d}{dV}[U_1(V) - U_2(V)]^c = 0. \quad (11)$$

Since the function $\psi(V)$ changes its sign at the critical point, while its first derivative with respect to volume is zero, the second derivative with respect to volume must also vanish at this point:

$$\frac{d^2\psi(V)}{dV^2} = \frac{d^2U_1(V)}{dV^2} - \frac{d^2U_2(V)}{dV^2} = 0.$$

Therefore, the critical point must be a bending point for the function $\psi(V)$ (otherwise, this function would have an extremum at this point), and we have

$$\left(\frac{\partial^2 U}{\partial V^2}\right)_T^c - \left(\frac{\partial^2 U}{\partial V^2}\right)_P^c = 0. \quad (12)$$

(It should be noted that in this equation, it is probable that both second-order partial derivatives of the internal energy with respect to volume vanish at the critical point.)

Thus, our analysis of expression (4) shows that the necessary and sufficient condition for the heat capacity C_V at the liquid–vapor critical point to exhibit infinite growth if conditions (1), (9), (10), (12) are fulfilled, and the first equality (2) is

$$\left(\frac{\partial^3 U}{\partial V^3}\right)_T^c - \left(\frac{\partial^3 U}{\partial V^3}\right)_P^c \neq 0. \quad (13)$$

In this case, the heat capacity C_V according to expression (4) tends to infinity in proportion to $1\Big/\left(\frac{\partial^3 P}{\partial V^3}\right)_T^c$.

We now demonstrate that C_V has a substantially positive nonzero value on the entire thermodynamic surface. This analysis also is based on expression (4), from which it can be seen that a divergence of C_V can only appear on the spinodal. Indeed, there are no other points in the two-phase region where the denominator of expression (4) can acquire zero values.

Since the ratio of the heat capacities $\frac{C_V}{C_P}$ on the spinodal (as well as at the critical point) is zero [2], the expression for C_V at an arbitrary point on the spinodal,

$$C_V^{sp} = \left(\frac{\partial P}{\partial T}\right)_V^{sp}\frac{\left(\frac{\partial U}{\partial V}\right)_T^{sp} - \left(\frac{\partial U}{\partial V}\right)_P^{sp}}{\left(\frac{\partial P}{\partial V}\right)_T^{sp}}, \quad (14)$$

exhibits an indeterminacy of the 0/0 type. In order to find the value of this indeterminate form, we use the same approach as that described above for the critical point. For this purpose, let us draw the isotherm $T = T_1$ and the isobar $P = P_1$ through an arbitrary point of the spinodal (see the figure, where this point is chosen on the liquid branch of the spinodal *sp*) in which the volume has the value $V = V_1(T_1, P_1)$. Obviously, the internal energy on these isolines is a function of the volume alone: $U_3 = U(T_1, V)$ and $U_4 = U(P_1, V)$. An analysis of the behavior of the function

$$\chi(V) = U_3(T_1, V) - U_4(P_1, V),$$

similar to that performed above for the function $\psi(V)$ at the critical point, shows that $\chi(V)$ has a minimum at $V = V_1$, so that $\frac{d^2\chi(V)}{dV^2} > 0$. However, since the second-order derivative in the denominator of expression (14) on the spinodal also is positive, $\left(\frac{\partial^2 P}{\partial V^2}\right)_T^{sp} > 0$, this formula shows that the specific heat at a constant volume does not change sign on crossing the spinodal. Therefore, the heat capacity C_V is finite and positive both on

the spinodal and in the entire region of the thermodynamic surface bounded by the spinodal.

The same conclusion concerning the finiteness of the specific heat at a constant volume on the spinodal was derived by Ivanov [2] who had analyzed the stability of the thermodynamic system. Moreover, the same result can be obtained proceeding from the assumption that C_V cannot vanish on the spinodal, since the temperature on the spinodal is always above zero [11].

Thus, we have demonstrated that one of the two conditions of thermodynamic stability (the mechanical stability criterion is $\left(\frac{\partial P}{\partial V}\right)_T < 0$, and the thermal-stability criterion is $C_V = \left(\frac{\partial U}{\partial T}\right)_V > 0$), namely, the thermal-stability condition is not violated and is valid everywhere on the thermodynamic surface, including the region bounded by the spinodal on the phase diagram P versus V.

The results of our analysis lead to the conclusion that the infinite growth of C_V at the critical point can be provided by describing the thermal and caloric properties in terms of the analytical equations of state (in which the first three derivatives of the pressure with respect to volume at a constant temperature must not diverge), whereby the singularity in C_V appears as a result of the division by zero in these equations. This approach solves the problem of matching the regular and singular parts of the equation of state, which (to our knowledge) has not thus far been solved.

ACKNOWLEDGMENTS

We are grateful to É.V. Matizen and Ya.M. Buzhdan for their help and useful advice.

REFERENCES

1. M. A. Anisimov, *Critical Phenomena in Liquids and Liquid Crystals* (Nauka, Moscow, 1987) [in Russian].
2. D. Yu. Ivanov, *Critical Behavior of Nonideal Systems* (Fizmatlit, Moscow, 2003) [in Russian].
3. A. Z. Patashinskiĭ and V. L. Pokrovskiĭ, *Fluctuation Theory of Phase Transitions* (Pergamon Press, Oxford, 1979; Nauka, Moscow, 1983).
4. I. I. Novikov, *Thermodynamics of Spinodals and Phase Transitions* (Nauka, Moscow, 2000) [in Russian].
5. I. I. Novikov, Teplofiz. Vys. Temp. **39** (1), 47 (2001).
6. I. I. Novikov, Teplofiz. Vys. Temp. **41** (3), 366 (2003).
7. V. V. Sychev, *Differential Equations of Thermodynamics* (Vysshaya Shkola, Moscow, 1991) [in Russian].
8. V. P. Skripov, E. N. Sinitsyn, P. A. Pavlov, *et al.*, *Thermophysical Properties of Liquids in the Metastable (Superheated) State* (Atomizdat, Moscow, 1980; Gordon and Breach, Amsterdam, 1988).
9. V. A. Kirilin, V. V. Sychev, and A. E. Sheĭndlin, *Technical Thermodynamics* (Nauka, Moscow, 1979) [in Russian].
10. I. N. Bronshteĭn and K. A. Semendyaev, *A Handbook on Mathematics for Engineers and Students of High-Education Technical Institutes* (Nauka, Moscow, 1981) [in Russian].
11. L. D. Landau and E. M. Lifshitz, *Course of Theoretical Physics*, Vol. 5: *Statistical Physics* (Pergamon, Oxford, 1980; Nauka, Moscow, 1995).

Translated by P. Pozdeev

Doklady Physics, Vol. 50, No. 9, 2005, pp. 438–440. Translated from Doklady Akademii Nauk, Vol. 404, No. 3, 2005, pp. 333–335.
Original Russian Text Copyright © 2005 by Karpenko, Savintsev, Temrokov.

PHYSICS

On the Possible Change of the Surface-Energy Sign in Ionic Dielectrics under High Pressures

S. V. Karpenko*, A. P. Savintsev, and A. I. Temrokov***

Presented by Academician V.E. Fortov March 4, 2005

Received May 4, 2005

The properties of substances under high pressures are of great interest in the physics of condensed state [1]. In the present paper, we analyze certain unconventional causes for the loss of stability in the crystal lattice of ionic dielectrics.

As is well known, under equilibrium conditions, surface energy is a strictly positive quantity [2]. As follows from the Gibbs formalism [3], in addressing the surface properties of a substance, we must allow for the surface energy in the crystal thermodynamic potential. This corresponds to the fact that the surface-layer particles of a substance tend to penetrate into the interior of a sample in order to reduce the internal energy of the system. In thermodynamics, this phenomenon is referred to as surface tension. However, the surface energy decreases when the external pressure is elevated [4]. Therefore, we can expect that at a certain pressure p_{cr} the surface energy will vanish and that it may even turn out to attain the region of negative values with a further increase in pressure. In this state, it is more profitable for surface-layer particles, from the standpoint of energy, to pass from the bulk of the substance onto the surface, because, in this case, the surface area increases, which results in a decrease in the system's total energy.

The formalism of the method of the electron-density functional [4] makes it possible to calculate the pressure value for which the surface energy can vanish. The corresponding calculation was performed for ionic crystals with a lattice structure of the NaCl type.

We write out the thermodynamic potential of a crystal under pressure as

$$G = \sum_{k=1}^{7} N_k U_k(a_k R) - V\frac{\partial}{\partial V}\left[\sum_{k=1}^{7} N_k U_k(a_k R)\right] - \frac{\alpha_\mu}{R} + 4\pi r^2 k\sigma. \quad (1)$$

Here, α_μ is the Madelung constant; R is the distance between the nearest neighbors; $V = 2R^3$ is the unit-cell volume; $U(R)$ is the potential of the pair interaction; $a_k = \frac{R_k}{R_0}$ is the ratio of the radii of the kth coordination sphere and of the first coordination sphere, respectively; N_k is the coordination number; σ is the surface energy; and k is the numerical coefficient taking into account the deviation of the crystal shape from the spherical one.

In accordance with the Gibbs definition, at the absolute-zero temperature, the surface energy density $\sigma(hkl)$ is of the form [5]

$$\sigma(hkl) = \sum_{i}\sum_{j=0}^{\infty}(W_j^{(i)} - W_\infty^{(i)})n_j(hkl). \quad (2)$$

Here, $\sigma(hkl)$ is the surface-energy density for the (hkl) face; $W_j^{(i)}$ is the energy of one particle in the jth layer, which is caused by the ith type of forces of the interionic interaction; $W_\infty^{(i)}$ is the same quantity related to the bulk of the crystal; and $n_j(hkl)$ is the number of particles per unit area in the jth plane.

We now analyze the approximation being used in more detail. One of the disadvantages of the Gibbs approach is the arbitrariness in the choice of the separating plane. By virtue of this fact, the value of $\sigma(hkl)$ depends on the place where the crystal interface is chosen because, as was emphasized in [6], the particle's density turns out to be different in different planes. A method that allows us to avoid this indeterminacy was developed in [7]. The essence of this method lies in the

* *Research Institute of Applied Mathematics and Automation, Kabardino-Balkar Scientific Center, Russian Academy of Sciences, Nalchik, 360000 Kabardino-Balkariya, Russia*
e-mail: karpenko@mail.ru

** *Berbekov Kabardino-Balkar State University, ul. Chernyshevskogo 173, Nalchik, 360004 Kabardino-Balkariya, Russia*

1028-3358/05/5009-0438$26.00 © 2005 Pleiades Publishing, Inc.

fact that a crystal is divided into plane grids, and the summation in the expression for the surface energy density is performed over the set of such grids. This is the approach that is used below for calculating the surface energy of ionic crystals.

In the zero approximation used here, expression (2) takes the form

$$\sigma(hkl) = n_0(hkl)\sum_i (W_0^{(i)} - W_\infty^{(i)}). \quad (3)$$

We consider a plane grid inside an infinite solid. It is evident that for an undistorted crystal, one can write out

$$W_\infty^{(i)} = W_S^{(i)} + 2W_{V/2}^{(i)}, \quad (4)$$

where $W_S^{(i)}$ is the energy of one particle on the grid, which is stipulated by the *i*th-type interaction forces of the given particle with all other particles belonging to the plane under consideration; and $W_{V/2}^{(i)}$ is the energy of the same particle, which is determined by the interaction with all particles belonging to all planes that lie above or below the given plane. Thus, the energy of one particle lying in the surface plane of an undistorted crystal is

$$W_0^{(i)} = W_S^{(i)} + W_{V/2}^{(i)}. \quad (5)$$

Excluding $W_{V/2}^{(i)}$ from expressions (4) and (5), we arrive at

$$\sigma(hkl) = \frac{1}{2}n_0(hkl)\sum_i (W_S^{(i)} - W_\infty^{(i)}). \quad (6)$$

We now introduce the notation $\beta^{(l)} = \dfrac{W_S^{(i)}}{W_\infty^{(i)}} = \dfrac{A_S^{(i)}}{A_V^{(i)}}$ for the ratio of sums over the infinite plane grid and the infinite lattice for the *i*th-type interaction forces of ions. Then, expression (6) is written out in the form

$$\sigma(hkl) = \frac{1}{2}n_0(hkl)\sum_n (\beta^{(i)} - 1)W_\infty^{(i)}. \quad (7)$$

In particular, for Coulomb forces, β is the ratio of the Madelung constants for the plane grid and three-dimensional lattice. For other forces, the quantity β is the ratio of rapidly converging series whose summing encounters no difficulties.

After the thermodynamic potential (1) has been constructed, we can find the desired equation of state $p = -\dfrac{dG}{dV}$, which allows us to determine the interparticle distance for which the surface energy vanishes. Calculations performed for all alkali-halide crystals yield for the ratio $\dfrac{r_0}{r_{cr}}$ the value of 1.16–1.21. Using the experimental data of [8] for the pressure dependence of the lattice constant, it is easy to find the pressure value for which the surface energy vanishes. The results obtained for infinitely large crystals and samples with a diameter of crystalline grains of 100 μm are presented in the table. For comparison, the values of pressure for the B1–B2 transition in massive samples of the given compounds [11] are also shown in the table. At pressures higher than those indicated in the table, the surface energy of alkali-halide crystals can become negative.

Critical pressure for a number of alkali-halide compounds

Crystal	$\dfrac{r_0}{r_{cr}}$	p_{cr}, kbar		$p_{B1–B2}$, kbar [14]
		$d = \infty$	$d = 10^{-4}$ m	
LiF	1.21	160	180	300
NaF	1.19	140	150	154
NaCl	1.18	110	115	138
NaBr	1.17	29	33	45
KCl	1.16	24	26	29
KBr	1.16	24	26	29

In addition to these calculations, the possibility of the existence of substance states having a negative surface energy was studied in the experiments with the optical breakdown of the bulk and surface of high-quality ionic crystals [9].

In our experiments, pulses 8 ns in duration (at half width) of a neodymium laser operating at a wavelength of 1.06 μm and a repetition frequency of 30 Hz were directed onto samples upon passing a lens with a focal distance of 5 cm.

In further calculations, we used the formula

$$\sigma(hkl) = \frac{n(hkl)E_g^v}{4}\left(1 - \sqrt{\frac{E_{cr}^s}{E_{cr}^v}}\right), \quad (8)$$

where E_g^v is the width of the forbidden zone in the sample volume, E_{cr}^v is the critical strength of the electric field in the volume, and E_{cr}^s is the critical strength of the electric field on the sample surface.

The experiment of [9] with a sodium chloride crystal has shown that $E_{cr}^s < E_{cr}^v$, which, in accordance with relationship (8), yields $\sigma > 0$. However, while investigating the laser breakdown of high-quality potassium chloride crystal, it was found that $E_{cr}^s > E_{cr}^v$; i.e., according to (8), $\sigma < 0$. This testifies to the fact that we have experimentally found conditions for the appearance of the substance state characterized by the negative surface energy.

As was emphasized in [10], for the substance state with a negative energy, which arises at extremely high

pressures, one can expect a sharp variation in the properties of a sample and even its failure. This is the process that occurs in the case of laser-induced breakdown. The pressures calculated in the present study at which the sample can pass to the state with a negative surface energy and pressures that can be obtained in the process of the laser destruction of ionic-dielectric surfaces are close to each other.

Indeed, in order to calculate the ablation pressures arising on the sample surface, while exposing the substance to nanosecond laser pulses, with allowance for the estimates made in [11, 12], and in addition to the scaling laws [13], we can use the formula

$$p_a(\text{kbar}) = 4.8 \times 10^4 \sqrt{I} \ (\text{W/cm}^2), \qquad (9)$$

where I is the power density of laser radiation.

Insofar as we have observed the laser breakdown of potassium chloride for $I_{cr} = (1.4 \pm 0.1) \times 10^{10}$ W cm^{-2}, we obtain $p_a = 57 \pm 4$ kbar. This value exceeds the value of p_{cr} indicated in the table for which the surface energy of an ionic crystal vanishes.

For sodium chloride, we have found in our experiments that $I_{cr} = (1.55 \pm 0.15) \times 10^{10}$ W cm^{-2}, which, in accordance with (9), yields $p_a = 60 \pm 6$ kbar. This value is lower than that of p_{cr} given in the table; i.e., under our conditions for sodium chloride, $\sigma > 0$.

The found values of p_{cr} (see table) for different sizes of the calculation region (d) are somewhat lower than the pressure (p_{B1-B2}) of the polymorphic B1–B2 transition that is realized in ionic crystals also under high pressures [14].

Thus, we have substantiated the possibility of the existence of a state in which a condensed medium can possess a negative surface energy.

REFERENCES

1. A. V. Bushman and V. E. Fortov, Usp. Fiz. Nauk **140**, 177 (1983) [Sov. Phys. Usp. **26**, 465 (1983)].
2. A. I. Temrokov, Teplofiz. Vys. Temp. **38**, 573 (2000).
3. D. V. Gibbs, *Thermodynamic Works* (Inostrannaya Literatura, Moscow, 1953) [in Russian].
4. V. F. Ukhov, R. M. Kobeleva, G. V. Dedkov, *et al.*, *Electron-Statistical Theory of Metals and Ionic Crystals* (Nauka, Moscow, 1982) [in Russian].
5. S. V. Karpenko, A. Kh. Kyarov, A. I. Temrokov, *et al.*, Kristallografiya **47**, 326 (2002) [Crystallogr. Rep. **47**, 291 (2002)].
6. G. G. Benson and K. S. Yun, J. Chem. Phys. **42**, 3085 (1965).
7. S. N. Zadumkin and A. I. Temrokov, Izv. Vyssh. Uchebn. Zaved., Fiz., No. 9, 40 (1968).
8. V. N. Zharkov and V. A. Kalinin, *Equations of State for Solids at High Pressures and Temperatures* (Nauka, Moscow, 1968; Consultant's Bureau, New York, 1971).
9. A. P. Savintsev, *Physics of Extreme States of Medium* (Inst. Prikl. Khim. Fiz. Ross. Akad. Nauk, Chernogolovka, 2005) [in Russian].
10. S. V. Karpenko, A. P. Savintsev, and A. I. Temrokov, in *Proc. Int. Symp. on Optics of the Atmosphere (OMA), Rostov-on-Don, Russia, 2003* (Inst. Prikl. Khim. Fiz. Ross. Akad. Nauk, Rostov-on-Don, 2003).
11. S. I. Anisimov, A. M. Prokhorov, and V. E. Fortov, Usp. Fiz. Nauk **142**, 184 (1984) [Sov. Phys. Usp. **27**, 181 (1984)].
12. N. V. Bugrov and N. S. Zakharov, in *Action of Intense Energy Fluxes on Matter* (Inst. Vys. Tekhnolog. Akad. Nauk, Moscow, 1992), pp. 210–216 [in Russian].
13. V. I. Vovchenko, I. K. Krasyuk, and A. Yu. Semenov, Tr. Inst. Obshch. Fiz. Khim., Akad. Nauk SSSR **36**, 129 (1992).
14. S. V. Karpenko, A. P. Savintsev, and A. I. Temrokov, Dokl. Akad. Nauk **388**, 41 (2003) [Dokl. Phys. **48**, 5 (2003)].

Translated by G. Merzon

Doklady Physics, Vol. 50, No. 9, 2005, pp. 441–443. Translated from Doklady Akademii Nauk, Vol. 404, No. 3, 2005, pp. 336–338.
Original Russian Text Copyright © 2005 by Golikov, Koroza, Polyakov.

TECHNICAL PHYSICS

Self-Consistent Interaction of Photoelectron Pulses with Irregular Waveguides

M. N. Golikov, V. I. Koroza, and A. S. Polyakov

Presented by Academician V.N. Mikhaĭlov January 28, 2005

Received January 31, 2005

The rapid progress that has been made in the area of ultra-wideband electromagnetic pulse (UWB EMP) technology [1, 2] poses new tasks of increasing complexity, which implies the need for the generalization and development of new theoretical and computational methods. One of these tasks is related to the possibility of using the subnanosecond pulsed flows of photoelectrons, emitted from metal walls of irregular waveguide tracts for the generation of UWB EMPs in such systems. The aim of this study was to evaluate this possibility.

Let us consider the device that is schematically depicted in Fig. 1. Here, *A* is the wall of an irregular waveguide, which acts as a photocathode; *B* is an isotropic pulsed source of monoenergetic photons (photoflash) with an energy exceeding the work function of the photocathode; and *C* is the accelerating grid with a high transmission (transparency) coefficient, which is equidistantly spaced from the cathode. Prior to the source flashing, the grid is charged to a sufficiently high voltage *U* relative to the photocathode, so that the flow of photoelectrons emitted from the cathode in the region $0 < z^* < 1$ is virtually perpendicular to the cathode surface.

The spatial coordinates (r and z in Fig. 1) and the other linear quantities (e.g., dimensions of structural elements) are rendered dimensionless by normalizing to a certain natural linear scale L, so that $r^* = r/L$, $z^* = z/L$, etc. In particular, the photocathode surface is described by the equation $r = b(z)$ or $r^* = b^*(z^*)$, where $b^*(z^*) = L^{-1}b(Lz^*)$. The time t is rendered dimensionless by normalizing to the characteristic time L/c, so that $t^* = \frac{ct}{L}$, where c is the velocity of light in vacuum.

According to the theory of the nonstationary excitation of irregular waveguides by TM waves, the device in Fig. 1 can be described in terms of the following set of equations [3]:

$$\frac{\partial}{\partial z^*}\left[G(z^*)\frac{\partial \mathbf{f}}{\partial z^*} + Q(z^*)\mathbf{f}\right] - Q^{\tau}(z^*)\frac{\partial \mathbf{f}}{\partial z^*} - P(z^*)\mathbf{f} - T(z^*)\frac{\partial^2 \mathbf{f}}{dt^{*2}} = L^{-1}\frac{\partial \boldsymbol{\lambda}}{\partial z^*} - \boldsymbol{\rho}. \quad (1)$$

Here, $\mathbf{f}(z^*, t^*)$ is the unknown column vector with the coordinates $f_j(z^*, t^*)$. These coordinates are represented by the coefficients of expansion of the magnetic field (having in this case the only nonzero component $H_\varphi(\mathbf{r}_\perp^*, z^*, t^*)$ with respect to a certain set of the basis functions $\{e_j(\mathbf{r}_\perp^*, z^*)\}$:

$$H_\varphi(\mathbf{r}_\perp^*, z^*, t^*) = \Sigma e_j(\mathbf{r}_\perp^*, z^*) f_j(z^*, t^*). \quad (2)$$

The dimensions of the $[N \times 1]$ column vectors $\mathbf{f}(z^*, t^*)$, $\boldsymbol{\lambda}$, and $\boldsymbol{\rho}$, the $[N \times N]$ square matrices $G(z^*)$, $P(z^*)$, $T(z^*)$, and $Q(z^*)$, and the transposed matrix

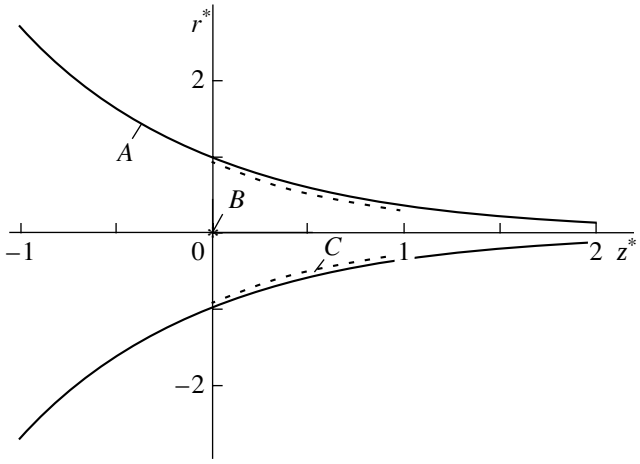

Fig. 1. Schematic diagram of the UWB EMP generator (see the text for explanations).

Institute of Strategic Stability, Moscow, Russia

1028-3358/05/5009-0441$26.00 © 2005 Pleiades Publishing, Inc.

$Q^{\tau}(z^*)$ are determined by the number N of terms in sum (2). The matrix elements are defined as

$$G_{ns}(z^*) = \iint\limits_{S(z^*)} \varepsilon^{-1} e_s e_n dS^*, \quad T_{ns}(z^*) = \iint\limits_{S(z^*)} \mu e_s e_n dS^*,$$

$$Q_{ns}(z^*) = \int\limits_{S(z^*)} \int \varepsilon^{-1} (e_s)_{z^*} e_n dS^*,$$

$$P_{ns}(z^*)$$

$$= \int\limits_{S(z^*)} \int \varepsilon^{-1} \{(e_s)_{z^*}(e_n)_{z^*} + r^{*-2}(r^* e_s)_{r^*}(r^* e_n)_{r^*}\} dS^*$$

and the coordinates of the column vectors $\boldsymbol{\lambda}$ and $\boldsymbol{\rho}$, as

$$\lambda_i = 4\pi L^2 \iint\limits_{S(z^*)} \varepsilon^{-1} \left(\frac{\mathbf{j}}{c}, [\mathbf{z}^0, \mathbf{e}_i]\right) dS^*,$$

$$\rho_i = 4\pi L \iint\limits_{S(z^*)} \varepsilon^{-1} \left(\frac{\mathbf{j}}{c}, \mathrm{rot}^* \mathbf{e}_i\right) dS^*,$$

where $\mathbf{j}$ is the photoelectron-current density; $\mathbf{e}_i = e_i \boldsymbol{\varphi}^0$; $\boldsymbol{\varphi}^0$ and $\mathbf{z}^0$ are the unit vectors of the cylindrical coordinate system; $S(z^*)$ is the integration domain representing a waveguide section perpendicular to the Z axis; ε and μ are the relative permittivity and magnetic permeability of the medium, respectively; and the subscripts z^* and r^* denote differentiation with respect to these variables.

A convenient basis set $\{e_j(\mathbf{r}_\perp^*, z^*)\}$ in expansion (2) is offered by a set of polynomials, which is obtained from the system $(r^{*k}, k = 1, 2, \ldots)$ by the orthogonalization on the segment $[0, b^*, (z^*)]$ with the weight r^* and by subsequent normalization.

The flow of photoelectrons emitted from the cathode in the region $0 < z^* < 1$ can be considered as a sequence of N_q quasi-particles representing thin circular tori with the radii $r_k^* = r_k^*(t^*)$, which are situated in the planes $z_k^* = z_k^*(t^*)$ $(k = 1, 2, \ldots, N_q)$. Photoelectrons generated outside the region $0 < z^* < 1$ are assumed to be slow. These particles produce no significant contribution to the electromagnetic radiation and, hence, can be ignored. In order to describe the flow of quasi-particles, let us divide the region $0 < z^* < 1$ into M equal parts and assume that the middle of each part is the emission center for a group of M_g quasi-particles, which are emitted sequentially with certain time delays so that $M M_g = N_q$. Every kth quasi-particle consists of n_k photoelectrons and carries a charge $q_k = -en_k$. As a result, we obtain the total photoelectron current

$$\mathbf{j} = \sum_{k=1}^{N_q} \mathbf{j}_k,$$

$$\mathbf{j}_k = cL^{-3}\left(\frac{q_k}{2\pi r^*}\right)\left(\frac{d\mathbf{r}_k^*}{dt^*}\right)\delta(r^* - r_k^*)\delta(z^* - z_k^*).$$

The set of equations (1) is solved together with the set of equations describing the motion of quasi-particles. In the relativistic approximation, these equations of motion are of the form

$$\frac{d^2 r_k^*}{dt^{*2}} = -\frac{eL}{m_0 c^2}\left[1 - \left(\frac{dr_k^*}{dt^*}\right)^2 - \left(\frac{dz_k^*}{dt^*}\right)^2\right]^{1/2} \times \left\{E_r - H_\varphi \frac{dz_k^*}{dt^*} - \frac{dr_k^*}{dt^*}\left(E_z \frac{dz_k^*}{dt^*} + E_r \frac{dr_k^*}{dt^*}\right)\right\}, \quad (3a)$$

$$\frac{d^2 z_k^*}{dt^{*2}} = -\frac{eL}{m_0 c^2}\left[1 - \left(\frac{dr_k^*}{dt^*}\right)^2 - \left(\frac{dz_k^*}{dt^*}\right)^2\right]^{1/2} \times \left\{E_z + H_\varphi \frac{dr_k^*}{dt^*} - \frac{dz_k^*}{dt^*}\left(E_z \frac{dz_k^*}{dt^*} + E_r \frac{dr_k^*}{dt^*}\right)\right\}. \quad (3b)$$

The quantities H_φ, E_r, and E_z in the right-hand side of Eqs. (3a) and (3b) can be expressed as functions of f given by Eqs. (1). The calculations involve the averaging of the right-hand side of Eqs. (1) and of the functions H_φ, E_r, and E_z over the computational lattice.

The starting conditions for each quasi-particle are determined by the start time (instant of emission) and the initial velocity. The start time is determined with allowance for a delay that is equal to the sum of the time required for photons to propagate over the distance from the source to the corresponding emission center of the photocathode, the time of quasi-particle formation (dependent on the electromagnetic radiation intensity), and the time required for the quasi-particle to travel over the cathode–grid distance δ^*. The initial quasi-particle velocity is determined by the grid voltage at the emission site at the start time.

Figure 2 shows an example of the results of the calculations performed for $L = 100$ cm, $U = 10^5$ V, and $\delta^* = 0.02$. The number of photons emitted within the solid angle 4π per unit time $(\Delta t^* = 1)$ was calculated as $n(t^*) = A\sin^2\frac{\pi t^*}{T^*}$ $[0 \le t^* \le T^*]$ for $A = 10^{21}$ and $T^* = 10^{-1}$. The quantum yield of photoelectrons was taken equal to 10^{-3} for $N = 15$, $N_q = 5000$ $(M = 500, M_g = 10)$, and the computational lattice parameters were $hz^* = 5 \times 10^{-3}$ and $ht^* = 5 \times 10^{-4}$. The electromagnetic energy excited by photoelectrons was determined by the inte-

gration of the excitation density over the volume. As can be seen from Fig. 2, this energy (curve *1*) initially increases with time (at the expense of the energy taken from the increasing number of accelerated electrons) and then decreases because the energy is returned to accelerated electrons. In Fig. 2, curve *2* shows the sum of the kinetic energies of all quasi-particles, including the loss related to the fraction of quasi-particles returned to the cathode (this loss is shown separately by curve *3*); curve *4* shows the sum of the excited electromagnetic energy (curve *1*) and the total kinetic energy of all quasi-particles (curve *2*). After the process of photoelectron emission to the space behind the grid ($t^* > 1.2$) has been terminated, this curve attains a plateau that corresponds to the electrostatic energy initially stored in the photocathode-grid gap, $W = \frac{1}{2} CU^2$, where C is the gap capacitance. Curve *5* in Fig. 2 corresponds to the total work performed by the Lorentz force for the transfer of all quasi-particles. The accuracy of calculations performed in the approximation used (assuming ideally conducting metal walls) can be judged from the difference between curves *1* and *5* (which must coincide) and from the amplitude of variations at the plateau of curve *4* (~0.2%). Calculations show that, by decreasing the scale of the computational lattice and increasing N, M, and M_g, the accuracy of the results (which was already high) can be further improved.

The obtained results show that the proposed approach ensures a high and controlled accuracy of calculations and can be efficiently used for the investigation and development of a broad class of devices and setups for the UWB EMP technology whose operation principle is based on the self-consistent interaction between the flows of charged particles and irregular waveguides.

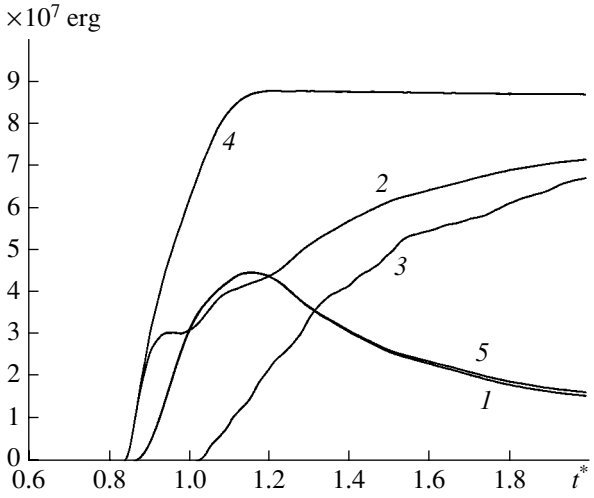

Fig. 2. Electromagnetic energy dynamics calculated using Eqs. (1) and (3) (see the text for explanations).

REFERENCES

1. *Ultra-Wideband, Short-Pulse Electromagnetics 3*, Ed. by C. E. Baum, L. Carin, and A. P. Stone (Plenum, New York, 1997).
2. *Ultra-Wideband, Short-Pulse Electromagnetics 4*, Ed. by E. Heyman, B. Mandelbaum, and J. Shiloh (Plenum, New York, 1999).
3. V. I. Koroza, Pis'ma Zh. Tekh. Fiz. **24**, 60 (1998) [Tech. Phys. Lett. **24** (8), 606 (1998)].

Translated by P. Pozdeev

Doklady Physics, Vol. 50, No. 9, 2005, pp. 444–447. Translated from Doklady Akademii Nauk, Vol. 404, No. 1, 2005, pp. 37–40.
Original Russian Text Copyright © 2005 by Ilgamov.

MECHANICS

Qualitative Analysis of the Evolution of Deviations from the Spherical Shape During the Collapse of a Cavity in a Liquid

Corresponding Member of the RAS M. A. Ilgamov

Received March 31, 2005

The spherical collapse of gas and vapor cavities under pressure in the surrounding liquid has been analyzed in numerous studies, e.g., in [1, 2]. A recent experimental investigation [3] was devoted to achieving a strong compression of bubbles in a cluster in the liquid subjected to acoustic action. The problem concerning the stability of the spherical motion of a cavity is complicated, and the effect of individual factors has not yet been revealed. A rather complete review of investigations on the stability of the spherical shape of small bubbles in the acoustically excited liquid was given in [4]. Linear and nonlinear problems concerning the stability of a spherical cavity are usually solved using numerical methods. In this case, it is difficult to determine the dependence of the solution on the input parameters because of their large number. In view of this circumstance, it is desirable to have simple analytical estimates, although they may be rough.

In this study, the evolution of a small deviation from the spherical shape of the cavity subjected to compression is considered disregarding the counterpressure, surface tension, viscosity, and compressibility of the liquid. This Rayleigh–Plesset problem [5, 6] can be taken as the simplest model for estimating distortions of the spherical shape. A further simplification can be achieved by considering only the final phase of the cavity collapse. As was shown in the numerical simulation [7], the rapid development of the instability of the shape occurs at that time.

Each of the above factors in the model leads to an increase in the stability of the process of the strong compression of the cavity, so that the stability is expected to be maximal when all these factors are taken into account. Thus, the proposed model underestimates the stability of the process of the strong compression of a cavity or overestimates its instability. If such an estimate of the increase in deviations turns out to be acceptable for certain cases, it is not necessary to take into account complex processes in the cavity or the actual properties of the surrounding liquid. This estimate may be used, e.g., to determine the conditions of the fragmentation of gas and vapor cavities up to a certain stage of compression when the characteristic times of formation of a converging spherical shock wave, its separation from the cavity surface, and its focusing at the center of the cavity are compared with the time of the substantial distortion of the spherical shape of the cavity. If this distortion occurs later than the focusing of the shock wave at the center of the cavity, it can be expected that the effect of the distortion of the cavity shape on the extremal values of temperature, pressure, and density will be small. The role of the above factors is significant for cavities with sizes of a millimeter or less (at the beginning of motion). It weakens with an increase in sizes. The role of the counterpressure and compressibility of the liquid is significant only at the final stage of compression.

Deviation from the spherical shape of the phase surface is assumed to be much smaller than the current radius and is taken in the form of spherical harmonics. In the above approximation, the set of the Rayleigh–Plesset equations for describing the motion of the cavity has the form [4–6]

$$R\ddot{R} + \frac{3}{2}\dot{R}^2 + \frac{p_\infty}{\rho} = 0,$$
$$\ddot{\varepsilon}_i + 5\frac{\dot{R}}{R}\dot{\varepsilon}_i + \left[3\left(\frac{\dot{R}}{R}\right)^2 - (i-2)\frac{\ddot{R}}{R}\right]\varepsilon_i = 0, \quad \varepsilon_i = \frac{a_i}{R}. \tag{1}$$

Here, R and a_i are the current radius of the cavity and the amplitude of the ith mode of the deviation of the spherical shape, respectively; ρ and p_∞ are the density and pressure in the liquid, respectively; and a dot over symbols stands for the derivative with respect to time t. The pressure p_∞ can vary with time t. According to the numerical simulation [7], the collapse at the final stage occurs several orders of magnitude faster than change in $p_\infty(t)$. For this reason, when integrating the first of Eqs. (1), the pressure $p_\infty(t)$ is taken as a constant (for the

Institute of Mechanics, Russian Academy of Sciences, ul. Karla Marksa 12, Ufa, 450025 Russia
e-mail: ilgamov@anrb.ru

1028-3358/05/5009-0444$26.00 © 2005 Pleiades Publishing, Inc.

acoustic excitation of pressure oscillations in the liquid, p_∞ can be approximately taken as the sum of the average pressure p_0 and amplitude p_a of the oscillations). In this case, we arrive at the following well-known first integral of the equation of motion [5]:

$$\dot{R}^2 = \frac{2p_\infty}{3\rho}\left[\left(\frac{R_m}{R}\right)^3 - 1\right], \quad (2)$$

where R_m is the initial radius of the cavity (or its maximum radius in the case of spherical oscillations).

We assume that the final stage of the collapse is determined by the radius R_* satisfying the condition $\left(\frac{R_*}{R_m}\right)^3 \ll 1$. Then we take, e.g., $\frac{R_*}{R_m} = 0.1$ and measure time t from the instant at which the radius is equal to R_*. For this radius, the velocity is equal to

$$\dot{R}_* \approx -\left[\frac{2p_\infty}{3\rho}\left(\frac{R_m}{R_*}\right)^3\right]^{\frac{1}{2}}, \quad t = 0, \quad (3)$$

but the time at which the values of R_* and $\dot{R}_*$ vary from R_m is unknown. The determination of this time is not required for further analysis.

Integrating Eq. (2) from R_* to R and from $t = 0$ to t and neglecting the last term, we obtain

$$R = R_*(1-\tau)^{\frac{2}{5}}, \quad \tau = \frac{t}{t_c}, \quad t_c = \frac{2}{5}\left(\frac{3\rho R_*^5}{2p_\infty R_m^3}\right)^{\frac{1}{2}}. \quad (4)$$

Substituting this value of R into Eq. (2) and into the first of Eqs. (1) and neglecting in the latter equation the terms $\left(\frac{R_*}{R_m}\right)^3$ that are much smaller than unity, we arrive at the expressions

$$\frac{\dot{R}}{R} = -\frac{2}{5t_c(1-\tau)}, \quad \frac{\ddot{R}}{R} = -\frac{6}{25t_c^2(1-\tau)^2}. \quad (5)$$

In view of Eqs. (4) and (5), the second equation of Eqs. (1) can be represented in the form

$$(1-\tau)^2\frac{d^2\varepsilon_i}{d\tau^2} - 2(1-\tau)\frac{d\varepsilon_i}{d\tau} + \mu_i\varepsilon_i = 0, \quad \mu_i = 0.24i. \quad (6)$$

The initial deviation ε_i^* from the spherical shape and the corresponding velocity $\dot{\varepsilon}_i^*$ ($\tau = 0$) are specified at the radius R_*. The problem is to determine the evolution of the initial deviation as the cavity surface moves to the center. The dimensionless deviation $\varepsilon_i(\tau)$ increases due not only to an increase in the absolute value of the deviation, but also to a decrease in the average radius $R(\tau)$. There is a certain arbitrariness in the specification of sufficiently small values of ε_i^* and $\dot{\varepsilon}_i^*$, as well as in their specification at the true initial radius R_m or at the equilibrium radius before the expansion of the bubble in the liquid where oscillations are acoustically excited. The following rough estimates are valid:

$$\frac{\varepsilon_i^*}{\varepsilon_i^m} \sim \left(\frac{R_m}{R_*}\right)^2, \left(\frac{R_m}{R_*}\right)^3,$$

where ε_i^m is the deviation at the radius R_m.

The solution of Eq. (6) is well known. It has a singularity as $\tau \longrightarrow 1$ and is expressed in terms of trigonometric functions with an argument containing the function $\ln(1-\tau)$. However, the qualitative behavior can be revealed with less difficulty. Analysis of the solution of Eq. (6) shows that, from $\tau = 0$ to $\tau \approx 0.85$, the function $\varepsilon_i(\tau)$ varies smoothly. Within this range, the effect of the term with the second derivative is relatively small. For $\tau > 0.85$, a sharp increase in ε_i begins. The second derivative also increases, but the factor $(1-\tau)^2$ decreases abruptly. Integrating Eq. (6) without the first term from ε_i^* ($\tau = 0$) to ε_i ($\tau < 1$), we determine the approximate value of the relative deviation

$$\varepsilon_i = \varepsilon_i^*(1-\tau)^{-\frac{\mu_i}{2}}. \quad (7)$$

A somewhat more accurate result can be obtained by substituting Eq. (7) into the correction term containing the second derivative in Eq. (6) and again integrating the equation. Moreover, the initial velocity $\dot{\varepsilon}_i^*$ ($\tau = 0$) can be approximately taken into account by replacing ε_i^* with $(\varepsilon_i^* + c_1\tau)$. Calculating the derivative $\dot{\varepsilon}_i$, we obtain the coefficient c_1. As a result, instead of Eq. (7), we obtain

$$\varepsilon_i = \left[\varepsilon_i^* + \left(\dot{\varepsilon}_i^* - \varepsilon_i^*\frac{3\mu_i}{4}\left(1 + \frac{\mu_i}{4}\right)\right)\tau\right](1-\tau)^{-\frac{3\mu_i}{4}\left(1+\frac{\mu_i}{4}\right)}. \quad (8)$$

A further refinement of the solution may be achieved by seeking it in the form of a series with a singularity at $\tau = 1$, e.g., in the form of the function

$$(\varepsilon_i^* + c_1\tau + c_2\tau^2 + \ldots)(1-\tau)^{-1/2}.$$

Figure 1 shows (for the case $i = 2$) plots for the exact solution of Eq. (6) and approximate solutions of Eqs. (7) and (8). The basic deficiency of the latter solutions is that they do not change the sign as τ increases. For cases in which the absolute value $|\varepsilon_i(\tau)|$ is of real interest, this deficiency is insignificant.

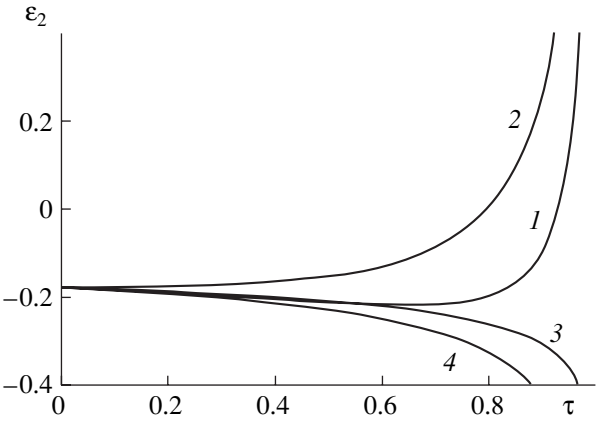

Fig. 1. Amplitude of elliptic ($i = 2$) deviation from the spherical shape of a spherical cavity near its poles vs. dimensionless time measured from the instant when the radius is $R_* = \frac{R_m}{10}$, where R_m is the maximum radius, for the initial conditions $\varepsilon_2^* = -0.1771$ and $\dot{\varepsilon}_2^* = -0.0623$: (*1*) exact solution of Eq. (6), (*2*) the same for $\dot{\varepsilon}_2^* = 0$, (*3*) solution (7), and (*4*) solution (8).

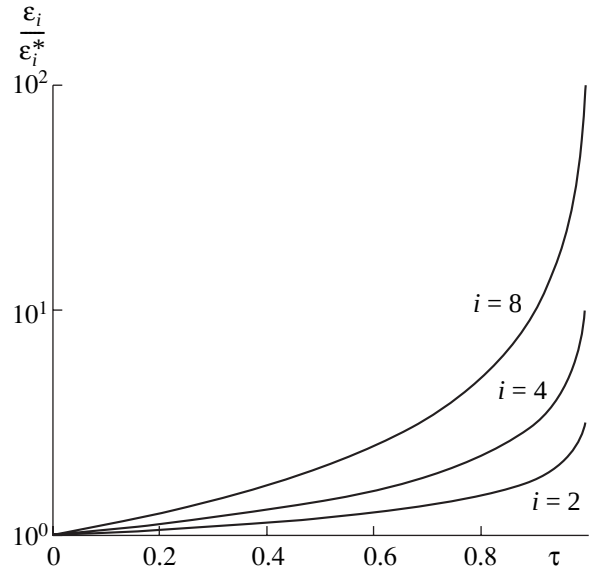

Fig. 2. Dimensionless-time dependence for amplitudes of spherical harmonics.

We note that the substitution of expression for μ_i from Eqs. (6) into Eqs. (7) and (8) reduces the latter expressions to the clearer approximate form

$$\frac{\varepsilon_i}{\varepsilon_i^*} = (1-\tau)^{-\frac{i}{8}},$$
$$\frac{\varepsilon_i}{\varepsilon_i^*} = \left[1 + \left(\frac{\dot{\varepsilon}_i^*}{\varepsilon_i^*} - \frac{3i}{16}\left(1 + \frac{i}{16}\right)\right)\tau\right](1-\tau)^{-\frac{3i}{16}\left(1+\frac{i}{16}\right)}. \quad (9)$$

In particular, for an important applied case of ellipsoidal perturbations $i = 2$, we have $\varepsilon_2 = \varepsilon_2^*(1-\tau)^{-1/4}$. Figure 2 shows the solution yielded by the first of Eqs. (9) for various spherical-harmonic numbers *i*. As is seen in Fig. 2, instability develops rapidly for higher harmonics. This property is consistent with the results obtained in [6] for oscillations and is a consequence of disregarding the factors indicated at the beginning of this paper.

Let us estimate the minimum of the radius $R = R_c$ under the assumption that the counterpressure is formed in the cavity when its initial volume decreases by a factor of 10^6 or more. The order of magnitude of R_c can be used to determine the order of magnitude of the dimensionless time τ_c to which Eqs. (7)–(9) are applicable.

For definiteness, we assume that the average pressure reaches $p_* = p_0$, where p_0 is the equilibrium pressure in the liquid, when the cavity decreases to radius R_* in a rarefied gas medium. For an adiabatic process with the adiabatic index γ, Eq. (2) is replaced by

$$\dot{R}^2 = \frac{2}{3\rho}\left[p_\infty\left(\frac{R_m}{R}\right)^3 - \frac{1}{\gamma-1}\left(p_0 + \frac{2\sigma}{R_*}\right)\left(\frac{R_*}{R}\right)^{3\gamma}\right], \quad (10)$$

where surface tension with the coefficient σ is also taken into account. Setting $\dot{R} = 0$ at $R = R_c$ and $\gamma = \frac{4}{3}$ in Eq. (10), we obtain

$$\frac{R_c}{R_*} = \frac{3}{p_\infty}\left(p_0 + \frac{2\sigma}{R_*}\right)\left(\frac{R_*}{R_m}\right)^3. \quad (11)$$

Thus, if the pressure-oscillation amplitude p_a in the total pressure in the liquid $p_\infty = p_0 + p_a$ is on the order of $2p_0$, then according to Eq. (11), the ratio $\frac{R_c}{R_*}$ is on the order of $\left(\frac{R_*}{R_m}\right)^3$. For the case under consideration, it is on the order of 10^{-3}; i.e., for very small radii R_c counterpressure leads to complete deceleration. Another estimate can be obtained using the van der Waals constant $A \approx \left(\frac{R_c}{R_*}\right)^3$ from which $\frac{R_c}{R_*} = A^{1/3} \approx (8.5^{-3})^{1/3} \approx 10^{-1}$. At the same time, the rapid increase in perturbations (Fig. 1) begins after $\tau \approx 0.85$, which yields $R \approx 0.5R_*$ according to Eq. (4). Therefore, the rapid increase in deviations from sphericity begins much earlier than the deceleration of the spherical motion of the cavity begins and stops. This behavior implies that the above assumptions are acceptable for the qualitative analysis of the phenomenon within the interval $0.5R_* < R < R_*$.

Numerical simulation of the compression of a vapor bubble in deuterated acetone under the conditions of the experiments reported in [3] shows that a convergent spherical shock wave is formed in a bubble at $R \approx 0.8R_*$, and its focusing at the bubble center occurs at $R \approx 0.3R_*$. Thus, near $R \approx R_*$, an interval may exist, where Eqs. (7)–(9) are applicable for the estimation of the shape distortion. Since the wave in the bubble is formed in this case earlier than distortions of its shape begin to rapidly increase (estimates are $R \approx 0.8R_*$ and $R \approx 0.5R_*$, respectively) and it moves faster than the phase surface, the focusing of the shock wave occurs with small deviation from sphericity when the initial dimensionless deviation $\varepsilon_i^{\mathrm{m}}$ is on the order of 10^{-3} or smaller (when $\varepsilon_i^* \sim 10^{-2}$, $\varepsilon_i^{\mathrm{m}}$ is on the order of 10^{-1}). For other input parameters, such estimates may change. In particular, for $\varepsilon_i^{\mathrm{m}} \sim 10^{-2}$, the focusing of the shock wave does not occur.

Thus, a simple model has been developed for the evolution of deviations from the spherical shape in the collapse of a cavity in a liquid. In this model, the pure radial motion is described by a nonlinear equation, whereas deviations from this motion, by a linear equation. According to this model, the collapse of the evacuated cavity is always unstable with respect to deviations from the spherical shape. Therefore, in the classical Rayleigh problem [5], the shape of a cavity in an ideal incompressible liquid is linearly unstable. For the most interesting case of ellipsoidal distortions of the spherical shape, this instability is rapidly developed only at the final stage of the collapse, when the radius reaches one-twentieth of the initial radius. This is an upper estimate (with reserve) of instability. The evolution of deviations from sphericity is approximately described by the very simple formula (7). The more accurate description for smaller radii ($R < \frac{R_{\mathrm{m}}}{20}$) can be obtained only by numerical simulation with the complete inclusion of actual properties of the liquid and gas in the cavity and in the framework of nonlinear theory of deviations from the spherical shape. However, in this case, perturbations also increase strongly only after the phase interface reaches one-twentieth of the initial radius.

ACKNOWLEDGMENTS

I am grateful to A.A. Aganin and V.G. Malakhov for their assistance in the work and to R.I. Nigmatulin for fruitful discussions. This work was supported by the Russian Foundation for Basic Research.

REFERENCES

1. R. I. Nigmatulin, *Dynamics of Multiphase Mediums* (Nauka, Moscow, 1987), Vol. 1 [in Russian].
2. V. K. Kedrinskiĭ, *Hydrodynamics of Explosion: Experiment and Models* (Sib. Otd. Ross. Akad. Nauk, Novosibirsk, 2000) [in Russian].
3. R. P. Taleyarkhan, C. D. West, J. S. Cho, *et al.*, Science **295**, 1868 (2002).
4. A. A. Aganin and M. A. Ilgamov, in *Dynamics of Gas Bubbles* (Kazan. Gos. Univ., Kazan, 2003), pp. 7–22 [in Russian].
5. G. Lamb, *Hydrodynamics* (Cambridge Univ. Press, Cambridge, 1932; Gostekhizdat, Leningrad, 1947).
6. M. S. Plesset, J. Appl. Math. **2** (1), 96 (1954).
7. A. A. Aganin, G. S. Guseva, and M. A. Ilgamov, in *Dynamics of Gas Bubbles* (Kazan. Gos. Univ., Kazan, 2003), pp. 95–32 [in Russian].

Translated by R. Tyapaev

Doklady Physics, Vol. 50, No. 9, 2005, pp. 448–451. Translated from Doklady Akademii Nauk, Vol. 404, No. 1, 2005, pp. 41–44.
Original Russian Text Copyright © 2005 by Petrov, Gruzdkov, Morozov.

MECHANICS

The Principle of Equal Powers for Multilevel Fracture in Continua

Yu. V. Petrov*, A. A. Gruzdkov, and Academician N. F. Morozov****

Received March 5, 2005

INTRODUCTION

Dynamic fracture in continua is a nonequilibrium process occurring at different structure-scale levels in both space and time. Experiments on the dynamic fracture of solids have revealed a number of effects that drastically contradict the classical models of strength properties and crack resistance [1, 2]. The corresponding classical criteria imply that the energy and momentum needed for the formation of new surfaces and fracture domains are spent in a continuous manner in the course of dynamic rupture. In [1], it was shown that introducing physical discreteness (alongside with discreteness related to the spatial geometry, which was discussed in [3–5]), i.e., the discrete consumption of the energy and momentum needed to maintain the process of dynamic rupture, provides the possibility of resolving some discrepancies of classical theory. Similar arguments were later presented in [6]. This approach, which, in fact, corresponds to an allowance for the space-time metrics of the process of dynamic rupture in continua [7], makes it possible to extend the nonlinear mechanics of fracture to dynamic problems [7, 8]. The principal difference of this approach from the others is that it explicitly introduces the concept of an incubation period (characteristic relaxation time for the pre-fracture process [7]), which forms the characteristic time scale. In addition, the corresponding extreme condition (criterion) for the rupture of continua at the given scale level is introduced, which takes into account both the space-time structure and the physical (energy) discreteness of fracture processes.

In the present paper, we demonstrate that the dynamic fracture of materials at different structure scales can be characterized by a constant value of the average power. This quantity can be defined as the ratio of the characteristic energy spent for the fracture of a structure element to the corresponding incubation period determined by the so-called fracture quantum. We also propose the general principle of equal power for the fracture of subsystems. This principle can be used for modeling different transition processes in both mechanics and physics.

THE STATIC LOADING

Let us discuss the slow uniaxial stretching of a sample made of an elastic brittle material. At a sufficiently slow variation of a load (for which the kinetic energy is negligibly low), a uniform stressed state is formed in the sample. In this case, numerous experimental data for different materials are well described by the force criterion of fracture:

$$\sigma \le \sigma_c. \tag{1}$$

The fracture occurs when stress σ attains the critical value σ_c (ultimate tensile strength). For a linearly elastic material, the ultimate specific (per unit volume) elastic energy can be written as

$$W_{sp} = \frac{\sigma_c^2}{2E}, \tag{2}$$

where E is the Young modulus. The critical value of the specific energy characterizes the strength of the material. It seems evident that the fracture is related to the energy consumption insofar as work is performed to break elementary bonds. Thus, it is natural to use the work performed (i.e., the energy spent for fracturing) as a defining characteristic parameter. In the case of an overloaded material, the ratio of the energy spent to the volume of the ruptured material exhibits a clearly pronounced size effect. Figure 1a illustrates the data for rocks on the specific (per unit volume) energy consumption for fracture as a function of the characteristic size of a fragment [9]. These data are well described by the relationship

$$\log\frac{W}{V} + \log d = \text{const}.$$

Taking into account the fact that the volume is proportional to the linear size d cubed, we find that the

* *Institute of Problems in Machine Science, Russian Academy of Sciences, Vasil'evskiĭ Ostrov, Bol'shoĭ pr. 61, St. Petersburg, 199178 Russia*
e-mail: yp@YP1004.spb.edu

** *St. Petersburg State University, Universitetskaya nab. 7/9, St. Petersburg, 199164 Russia*

1028-3358/05/5009-0448$26.00 © 2005 Pleiades Publishing, Inc.

energy consumption W is proportional to d^2, i.e., is determined by the area of the formed surface. This is clearly seen from Fig. 1b, which demonstrates the dependence of the energy per unit area on the linear size of a sample.

Thus, if the fracture occurs as a result of the formation of new surfaces, then the ratio of the accumulated elastic energy to the area of the formed surface attains the critical value. Note that this concept forms the basis of the Griffith theory, according to which the crack growth must begin when the internal energy accumulated in the process of strains is transformed into the energy of new arising surfaces:

$$\frac{dG}{dS} = 2\gamma. \tag{3}$$

Here, γ is the Griffith's constant, i.e., the specific (per unit area) energy spent for the formation of a new surface. All the aforementioned criteria have shown their adequacy in the analysis of experimental data for the case of a sufficiently slow loading. The seeming discrepancy between criteria (2) and (3) is explained in the following way. On the one hand, the fracture is not a local process (the energy needed for the fracture is not concentrated at a single point). On the other hand, this process involves not the entire energy accumulated in the sample, but only a portion concentrated in a region close to the fracture zone. Let S be the area of the surface arising in the course of fracture. Then, according to relationships (2) and (3), the energy spent for fracture can be written in the form

$$G_0 = \gamma S = W_{sp} S\delta = \frac{\sigma_c^2 S\delta}{2E}, \tag{4}$$

where δ is the characteristic linear size of the region involved in the fracture process. From relationship (4), we find $\gamma = W_{sp}\delta$. In the case of a crack loaded according to mode 1, the critical surface energy corresponding to the fracture is expressed in terms of the critical stress-intensity coefficient by the formula $\gamma = \frac{2}{\pi}\frac{K_{ic}^2}{2E}$. Then, the characteristic size of the fracture zone can be represented in terms of the characteristic parameters of the material

$$\delta = \frac{2}{\pi}\left(\frac{K_{ic}}{\sigma_c}\right)^2. \tag{5}$$

The quantity δ features the typical size of a fragment at a quasi-static fracture. Note that relationship (4) implies that the tests for fracture (at the given scale level) in samples with sizes much less than the critical value are incorrect, since they are unable to accumulate a sufficient energy. Note also that similar conclusions were drawn by other authors (see, e.g., [10, 11]).

THE DYNAMIC LOADING

Numerous experimental data demonstrate that criterion (1) is inapplicable in the case of short-time loading. This occurs because the critical stress corresponding to fracture becomes significantly higher with a decrease in the duration of loading and also depends on the fracture history. There is also no reason to believe that the other characteristics of the static fracture, such as δ and γ, remain unchanged.

We now consider the case in which the elastic energy in a sample far exceeds the local kinetic energy, i.e., the kinetic energy determined by the displacement of fixed points in the sample with respect to each other. Note that the local kinetic energy turns out to be dominant for either samples of a larger size or very high strain rates. We discuss the situation when the loading is rapid from the "standpoint" of the material properties, while it is slow (static) from the "standpoint" of the

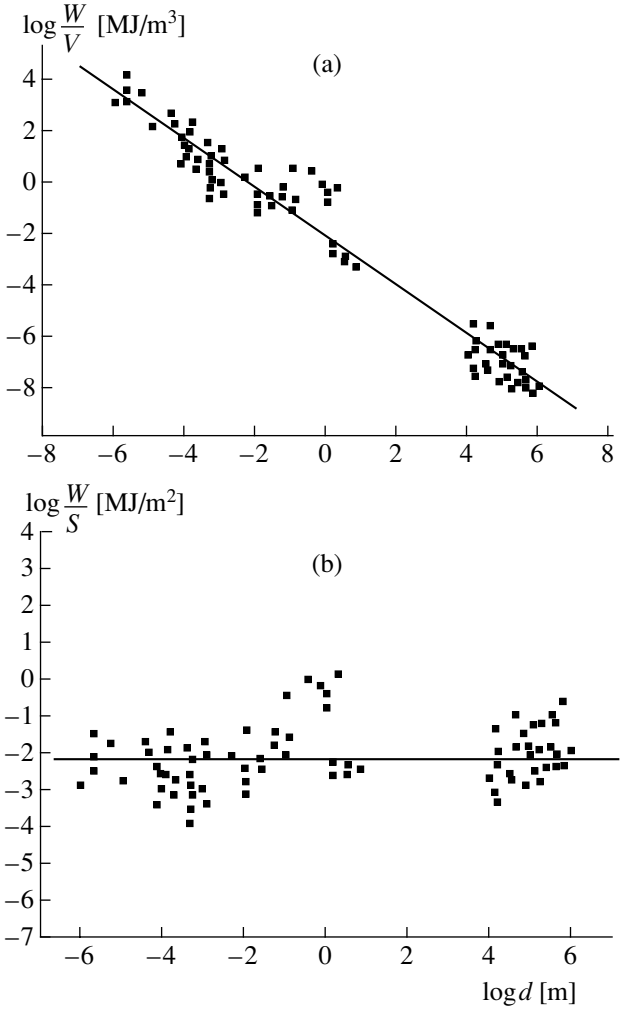

Fig. 1. Specific energy expenditures for the fracture of rocks (a) per unit volume and (b) per unit area as functions of the fragment characteristic size. The data were obtained from the measurements performed under laboratory, industrial, and natural conditions [9].

sample (structure) [12]. In this case, the fracture of the material is determined not only by force-related parameters but also by time characteristics such as the characteristic time τ of incubation processes occurring in the material structure. As the fracture criterion, we use that related to the incubation time [1, 2, 7, 8].

Let us assume that the sample is suddenly loaded by a constant tensile stress $\sigma(t) = PH(t)$ exceeding the static ultimate tensile strength. (Here, $H(t)$ is the Heaviside step function.) The fracture occurs not instantaneously but after a certain time period t_* determined by the incubation-time criterion, i.e., by the condition that the momentum applied during the incubation time τ is equal to the minimum fracturing momentum

$$\int_{t_*-\tau}^{t_*} \sigma(t)dt = \sigma_c\tau. \quad (6)$$

From relationship (6), we have $t_* = \dfrac{\sigma_c\tau}{P}$. The specific elastic energy in the fracture zone is determined by the formula $\tilde{W}_{sp} = \dfrac{P^2}{2E}$, and, hence, $\tilde{W}_{sp} = \dfrac{\sigma_c^2\tau^2}{2Et_*^2}$.

Let δ_* be the size of the region whose energy could be transferred to the fracture zone. Insofar as the transfer of the elastic energy takes place at a finite rate coinciding with the velocity c of an elastic wave, we assume that $\delta_* = ct_*$ [11, 13]. At $P = \sigma_c$, the time t_* elapsed before fracture coincides with the incubation time τ. In this case, denoting the characteristic size of the fracture zone as $\delta_0 = c\tau$, we arrive at the evident relationships

$$\frac{\delta_*}{\delta_0} = \frac{t_*}{\tau}, \quad \delta_* = \frac{\delta_0 t_*}{\tau}. \quad (7)$$

Using formula (7), we rewrite the expression for the specific elastic energy in the form

$$\tilde{W}_{sp} = \frac{\sigma_c^2}{2E}\left(\frac{\delta_0}{\delta_*}\right)^2 = W_{sp}\left(\frac{\delta_0}{\delta_*}\right)^2. \quad (8)$$

To find the energy spent for fracture, we multiply the specific energy by the characteristic volume of the fracture region, which is obviously proportional to δ_*^3:

$$G = \tilde{W}_{sp}\delta_*^3 = W_{sp}\delta_0^2\delta_*.$$

Taking (7) into account, we obtain as a final result

$$G = W_{sp}\delta_0^3\frac{t_*}{\tau}.$$

Dividing both parts of the latter relationship by the time elapsed before fracture, we find the expression for the power, i.e., for the rate at which the elastic energy is liberated:

$$\frac{G}{t_*} = \frac{W_{sp}\delta_0^3}{\tau} = \frac{G_0}{\tau}. \quad (9)$$

THE PRINCIPLE OF EQUAL POWERS

Thus, the ratio of the energy spent for fracture to the time elapsed before fracture, i.e., the average power, remains constant at an arbitrary applied stress exceeding the threshold level for the static case. Let $\gamma = W_{sp}\delta$ be the characteristic energy for the formation of a new surface for a load equal to the static ultimate tensile strength at a given scale level. We assume that the material is characterized by the limiting value of the strain energy density W_{sp} being the same for all scale levels. Nevertheless, this assumption does not exclude a possibility of changing the strength and strain characteristics of the material, while passing from one to another scale level.

We admit that the fracture of a material is constituted by the formation in this material of a defect of the characteristic size δ_1. This process is characterized by the incubation time $\tau_1 = \dfrac{\delta_1}{c}$. In this case, the specific power remains the same as in the situation when δ_0 is chosen as the characteristic scale for fracture. Indeed, taking into account that $\dfrac{\delta_1}{\tau_1} = \dfrac{\delta_0}{\tau} = c$, we find from (9)

$$\frac{G_0}{\tau} = \frac{W_{sp}\delta_0^3}{\tau} = \frac{W_{sp}\delta_1^3\tau^2}{\tau_1^3} = \frac{G_1}{\tau_1}\left(\frac{\tau}{\tau_1}\right)^2 = \frac{G_1}{\tau_1}\left(\frac{\delta_0}{\delta_1}\right)^2.$$

Introducing the characteristic area of the fracture surface by the relationship $S_k = \delta_k^2$, we obtain the following equality for specific powers $\dfrac{G_0}{\tau S_0} = \dfrac{G_1}{\tau_1 S_1}$, or

$$\frac{\gamma_0}{\tau} = \frac{\gamma_1}{\tau_1}. \quad (10)$$

Eventually, we arrive at the conclusion that, at different scale levels (or for subsystems corresponding to the given point in a continuum), the fracture can be characterized by the *principle of equal powers*:

$$\frac{Q_1}{\tau_1} = \frac{Q_2}{\tau_2} = \ldots = \frac{Q_i}{\tau_i} = \ldots = \text{const}, \quad (11)$$

where Q_i is the characteristic energy for the activation of the fracture process, and τ_i is the incubation time for the ith scale level. The above reasoning demonstrates that, for a fracture occurring due to the crack formation,

the quantity Q_i can be treated as the specific surface energy for fracture at the corresponding ith scale level. A particular case of relationship (11) was previously discussed in [14], namely,

$$\frac{Q}{\tau} = \frac{kT}{\tau_0}. \quad (12)$$

Here, $k = 1.3807 \times 10^{-23}$ J/K is the Boltzmann constant, T is temperature, and $\tau_0 \approx 10^{-13}$ s is the period of valence vibrations of atoms in solids (period of elementary fluctuation). It is well known that kT is the energy corresponding to the vibratory degree of freedom in the equilibrium state. Thus, it is the minimum energy required to disturb the elementary bond, i.e., the bond between two atoms. The parameter Q was interpreted as the elementary portion of energy required for fracturing the structure cell at a given scale level. Based on relationship (12) and incubation-time criterion (6), an explanation was given in [14] for both the temperature dependence of the splitting-off strength and anomalous melting points related to the splitting off [15]. The corresponding calculations have also been performed, and their good agreement with experimental data was demonstrated.

The suggested *principle of equal powers* can serve as a tool in modeling both dynamic-fracture processes and phase transitions at different scales of structure-scale levels and for the efficient analysis of transition (nonequilibrium) processes in the mechanics and physics of continuum.

ACKNOWLEDGMENTS

This work was supported by the Russian Foundation for Basic Research (project nos. 03-01-39010, 05-01-01068, and 03-01-00721) and by the Russian Academy of Sciences (Program “The Physics and Mechanics of Strongly Compressed Materials and the Problems of the Internal Structure of the Earth and Planets”).

REFERENCES

1. Yu. V. Petrov, Dokl. Akad. Nauk SSSR **321**, 66 (1991) [Sov. Phys. Dokl. **36**, 802 (1991)].
2. N. F. Morozov and Yu. V. Petrov, Dokl. Akad. Nauk SSSR **324**, 964 (1992) [Sov. Phys. Dokl. **37**, 285 (1992)].
3. V. V. Novozhilov, Prikl. Mat. Mekh. **33** (2), 212 (1969).
4. M. A. Sadovskiĭ, V. F. Pisarenko, and V. N. Rodionov, Vestn. Akad. Nauk SSSR, No. 1, 82 (1983).
5. E. I. Shemyakin, Dokl. Akad. Nauk SSSR **300**, 1090 (1988).
6. Yu. A. Khon and V. E. Panin, Fiz. Tverd. Tela (St. Petersburg) **38**, 1767 (1996) [Phys. Solid State **38**, 974 (1996)].
7. Yu. V. Petrov, Preprint No. 139, IPMash (Inst. Prib. Mashinostr., St. Petersburg, 1996).
8. N. Morozov and Y. Petrov, *Dynamics of Fracture* (Springer, Berlin, 2000).
9. V. N. Bovenko and L. Zh. Gorobets, Probl. Prochnosti, No. 1 (1987).
10. A. G. Ivanov, Prikl. Mekh. Tekh. Fiz., No. 3, 116 (1994).
11. V. A. Ogorodnikov and A. G. Ivanov, Fiz. Goreniya Vzryva **37** (1), 133 (2001).
12. N. F. Morozov and Yu. V. Petrov, Dokl. Akad. Nauk **382**, 206 (2002) [Dokl. Phys. **47**, 87 (2002)].
13. V. A. Bratov, A. A. Gruzdkov, S. I. Krivosheev, *et al.*, Dokl. Akad. Nauk **396**, 345 (2004) [Dokl. Phys. **49**, 338 (2004)].
14. Yu. V. Petrov and E. V. Sitnikova, Dokl. Akad. Nauk **400**, 480 (2005) [Dokl. Phys. **50**, 88 (2005)].
15. G. I. Kanel and S. V. Razorenov, Fiz. Tverd. Tela (St. Petersburg) **43**, 839 (2001) [Phys. Solid State **43**, 871 (2001)].

Translated by K. Kugel

Doklady Physics, Vol. 50, No. 9, 2005, pp. 452–456. Translated from Doklady Akademii Nauk, Vol. 404, No. 1, 2005, pp. 45–49.
Original Russian Text Copyright © 2005 by Chashechkin, Mitkin.

MECHANICS

Formation of Vortices on Soaring Interfaces in Stratified Flows Behind a Cylinder

Yu. D. Chashechkin and V. V. Mitkin

Presented by Academician V.V. Kozlov May 20, 2005

Received May 24, 2005

At present, mechanisms responsible for the formation of fine structures in stable stratified media such as the Earth's atmosphere [1] or hydrosphere [2] with allowance for high-gradient interfaces and thicker homogeneous layers are being intensely studied in natural and laboratory conditions. In the case of flows around obstacles, extended long-life interfaces generated by both vortices and boundary layers appreciably affect flow dynamics and flow structure, as well as the energy and mass transfer. In certain two-dimensional stratified cuts, isolated interfaces having no singularities on their edges are formed immediately in the internal-wave field [3]. In flow-regime diagrams typical of stratified flows near a horizontal circular cylinder, there exist parameter ranges in which isolated interfaces are observed for both pointed and blunted leading edges [4]. The mutual transformation of solitary interfaces and soaring vortices (or vortex systems) has never been considered. In the present study, we analyze the process of soaring-vortex formation in the field of attached internal waves and of reconstructing their structure in the case of the vortex-system generation. We studied experimentally the flow pattern arising at the onset of the uniform motion of a circular cylinder in a linearly stratified fluid.

The dimensional parameters of the problem are the velocity of motion **U**, the obstacle size (cylinder diameter D), fluid density ρ and its gradient $\frac{d\rho}{dz}$, kinematic viscosity ν, diffusivity κ_s of a stratifying admixture, and the free-fall acceleration g. The stratification is characterized by the scale $\Lambda = \left|\frac{1}{\rho}\frac{d\rho}{dz}\right|^{-1}$, the buoyancy frequency N, and the buoyancy period T_b ($N = \frac{2\pi}{T_b} = \sqrt{\frac{g}{\Lambda}}$). The salinity and density are considered to be bound by the linear equation of state, the coefficient of the salt contraction being included in the definition of salinity [2].

The basic components of the flow pattern in front of the obstacle are blocked liquid and advancing unsteady internal waves. Behind the obstacle, the basic components are attached internal waves with the characteristic scale $\lambda = UT_b$ [5] and the wake with immersed and soaring vortices. The family of boundary layers adjoins the obstacle surface [6]. Periodic boundary layers such as flows induced by diffusion on topography are characterized by the universal internal microscales $\delta_\nu = \sqrt{\frac{\nu}{N}}$ for the velocity and $\delta_\rho = \sqrt{\frac{\kappa_s}{N}}$ for the density. The velocity boundary layer and the density boundary layer contacting the uniform flow have the characteristic scales $\delta_u = \frac{\nu}{U}$ and $\delta_s = \frac{\kappa_s}{U}$, respectively.

The ratios of the problem characteristic scales and basic structural flow components form conventional dimensionless flow characteristics, namely, Reynolds number $\mathrm{Re} = \frac{D}{\delta_u} = \frac{UD}{\nu}$, Pecklet number $\mathrm{Pe} = \frac{D}{\delta_s} = \frac{UD}{\kappa_s}$, and Stokes number $\mathrm{St} = \frac{D^2}{\delta_\nu^2} = \frac{ND^2}{\nu}$ (or internal Froude number $\mathrm{Fr} = \frac{\mathrm{Re}}{\mathrm{St}} = \frac{\lambda}{2\pi D} = \frac{U}{ND}$; here, $\lambda = UT_b$ is the wavelength of the attached internal wave). The ratio of the scales $C = \frac{\Lambda}{D}$ characterizes the density variation on the obstacle scale. In the given experiments, the Schmidt number $\mathrm{Sc} = \mathrm{Pe}/\mathrm{Re} = 700$ was constant.

The experimental method and the size of the flow observation domain were chosen based on the conditions of recording large-scale components (internal waves and vortices) and of resolving the most small-scale flow components. The high-sensitivity optical shadow methods [7] entirely satisfy these requirements.

Institute for Problems in Mechanics,
Russian Academy of Sciences,
pr. Vernadskogo 101/1, Moscow, 119526 Russia
e-mail: chakin@ipmnet.ru

1028-3358/05/5009-0452$26.00 © 2005 Pleiades Publishing, Inc.

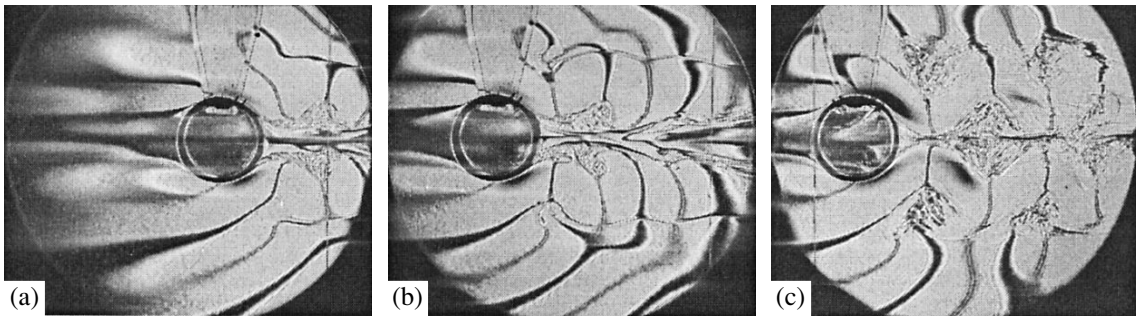

Fig. 1. Evolution of the flow pattern near the horizontal cylinder in a weakly stratified fluid (T_b = 13 s; D = 5 cm; U = 0.35 cm s^{-1}; Fr = 0.14; and Re = 165): (a) soaring interface being formed, $\tau = \frac{t}{T_b} = 3.9$; (b) solitary vortex at the interface leading edge, $\tau = 5.8$; and (c) vortex system on the density interface, $\tau = 65$.

Our experiments were carried out in a basin with a volume of $220 \times 40 \times 60$ cm^3 with transparent optical windows mounted on the side walls. Using the permanent-replacement method, we filled the basin with the stratified solution of common salt at the buoyancy period of 7.4 s < T_b < 23 s. The homogeneity and the stratification value were checked by means of a density marker [8].

Above the basin, a movable carriage was installed to which a plastic horizontal cylinder 5 cm in diameter and of a length equal to the basin width was fixed by means of knives. The cylinder was placed across the basin and was towed in the horizontal direction at a constant velocity. The uniformity of motion and the velocity magnitude U (0.1 cm s^{-1} < U < 6.5 cm s^{-1}) were recorded by optical methods.

The observations were carried out by the shadow IAB-458 device using the method of vertical-slit–filament in focus and a white-light source [7]. The color flow image obtained is determined by the light dispersion in the stratified fluid. This image was recorded by a photographic camera onto a color film. In this paper, we demonstrate black-white versions of the images after they have been modified by a computer.

The experimental method used is based on the previously established reproducibility of both the microstructural and macrostructural components of stratified flows [4, 5]. In the series of sequential experiments, parameters of the stratification and of the body's motion were maintained invariable. The towed obstacle was installed at different distances from the observation domain so that the length of the path passed every time increased by the width of the field of vision. Thus, the flow patterns at the exit of the obstacle from the field of vision in the preceding experiment and at the entrance into the field of vision in the next experiment coincided with each other.

A typical shadow image of flow in the phase of the soaring-interface formation is shown in Fig. 1a. Inclined bands in front of the body (i.e., beams with a step $\lambda \approx UT_b$ = 4.55 cm) illustrate advancing unsteady internal waves. The wedge-shaped perturbation in front of the cylinder corresponds to the blocked liquid that moves together with the obstacle. In contrast to the more widely propagated knife method, the filament method makes it possible to both visualize the general flow structure and recognize delicate flow components such as the high-gradient interfaces that bound blocked fluid immediately in front of the obstacle. These interfaces are located near the contact domains of blocked liquid and free external flow with the cylinder leading edge. The contact points of advancing interfaces with the cylinder are located on beams inclined at an angle $\varphi = \pm 52°$ (here, angles are counted off from the first damping point). These structures increase the effective length of the obstacle and promote the rise of internal-wave amplitudes.

Behind the body, a system of attached internal waves and the density wake are formed [1, 5]. For the latter, the shape of its boundary and its internal structure are dependent on the pattern of immersed vortices. The phase surfaces of attached internal waves are smoothly transformed into the beams of unsteady waves in front of the body.

The wake consists of a sequence of vortices and a system of flows. In Fig. 1a, the most rapid (central) flow is marked by the dark band. The rear vortex directly adjoins the body. The vortex height, like the height of the wake as a whole, rapidly decreases. Further increase in the wake height is stipulated by a pair of immersed vortex bundles (vortex bubbles in the terminology of [1]) stationary with respect to the obstacle and located in parallel with the cylinder generatrix. The vortex leading edge is convex, whereas the trailing edge has a more complicated shape. This is caused by the fact that in the vicinity of the trailing edge fluid moves more rapidly, and here the interfaces are drifted by the flow. At the vortex center, a merging of oppositely moving interfaces occurs, which is confirmed by the characteristic shape of perturbations. Further, the vertical wake size decreases again and attains the minimum at a

distance of $s_3 = 4.9$ cm from the body's trailing edge. The position of vortex pairs immersed in the wake is strongly synchronized with the phase structure of attached waves. Lines of crests (solid dark lines) and of troughs (double grey lines) advance precisely to the center of the vortices immersed in the wake.

In the transition regime, features of all flow components vary with time: the length of the blocked-liquid domain increases, the amplitudes of unsteady advancing and attached internal waves rise, the sizes of vortex systems extend, and the uniformity of the initial density gradient is violated (Figs. 1a and 1b). Each new attached wave is formed after the body has passed a path equal to its wavelength. The shape of the wave corresponds to that calculated according to the linear theory [5]. The position of vortex bundles immersed into the wake, which is synchronized with the field of stationary attached internal waves, remains invariable, whereas their shape and size smoothly vary with time.

The pattern of high-gradient interfaces characterizes the complicated flow structure inside the wake. In its center, there is a relatively rapid jet approaching the obstacle, which is bounded by inclined shells (Fig. 1b). Here, optical inhomogeneities are oriented towards the direction of the body's motion.

The pattern of attached internal waves preserves its regularity until the density-gradient field loses its uniformity. Attached internal waves incident on interfaces are partly reflected and partly transformed into internal boundary currents [9] that, in turn, amplify arising stratification inhomogeneities.

Gradually, distortions of the initially homogeneous stratification gradients become more and more pronounced and begin to be recorded by the shadow device. Novel structure components appear in the flow pattern, namely, solitary isolated interfaces [3]. They are located at both sides at a distance $h = 4.3$ cm from the density-wake axis $\left(\frac{h}{\lambda} = 0.95, \frac{h}{D} = 0.86, \text{Fig. 1a}\right)$ and are formed simultaneously along the entire length. The pointed leading edge of the soaring interface is located on the beam forming the angle $\psi = 48°$ with the axis of motion and at a distance of 6 cm from the body's center (here, angles are measured from the damping back point).

An advancing effect of the soaring interface is manifested in the distortions of the first crest of the attached wave in the lower half-space (dark line) and of the first trough (double grey line) in the upper half-space. Further, the flow pattern is analyzed only in the lower half-space, in which the perturbing action of the supporting knives is not manifested.

The inclination of phase surfaces for short internal waves is determined by the ratio of the local wave frequency ω to the buoyancy frequency N with allowance for the Doppler shift ($\omega = \omega_0 + \mathbf{ku}$, where $\mathbf{u}$ is the fluid-flow velocity, $\mathbf{k}$ is the wave vector of attached internal waves). The inverse inclination of phase surfaces existing between the density wake and the internal interface edge (Fig. 1b) testifies to the formation in the vicinity of the density-layer boundary of a liquid layer with a large shear of velocity.

The wake boundaries are separated by immersed vortices and merge in the domains of jet flows. The height of the attached vortex decreases rather rapidly, and the wake vertical size attains its minimum value $h_z = 2.0$ cm at a distance $s_1 = 1.1$ cm from the body's trailing edge (Fig. 1b). Further, the height smoothly increases and attains its maximum in contact domains with the crest in the upper half-space and the trough of the second attached wave at a distance $s_2 = 3.5$ cm from the trailing edge.

The analysis of changes in the location and shape of the crests and troughs of attached internal waves allows us to reveal the mechanism of the vortex-system formation at the body's leading edge. This mechanism is closely related to the arising spatial homogeneity of the flow structure.

Inhomogeneities of the velocity and density fields behind the obstacle distort the shape of the second attached internal wave. At the external side of the interface, the second trough deviates in the forward direction with respect to the body's motion; at the internal side, within the flow region between the interface and the density wake, it deviates backward (Fig. 1a). In contrast to the trough, the second crest everywhere displaces backward: significantly near the interface external side and negligibly at the internal side. As the gradients increase, these displacements rise, and gradually the intersection domain of the internal wave with the interface acquires new properties. In this domain, a wave crest incoming from the external side turns out to be in contact with a trough incoming from the internal side.

At this stage, in the vicinity of the first vortex immersed in the wake, there exists a trough of the attached wave (its center corresponds to the double grey line in Figs. 1b and 1c) in the layer of liquid between the soaring interface and the density wake. One of its ends adjoins the vortex center, whereas the other end touches the interface and determines its concave shape in this segment.

On the outside of the interface, an internal-wave crest adjoins the same point (the crest center corresponds to the solid dark line). Thus, in the head segment above and below the soaring interface, wave fields are present in which the velocities have oppositely directed vertical components. Counter-running wave motions are transformed into spatially inhomogeneous spreading horizontal flows on the surface of the soaring interface. This complicated flow structure is stabilized by high-density gradients at the interface. All arising inhomogeneities of the density distribution are of a purely deformation nature and have been formed as a result of smooth liquid-particle transfer from different horizons.

In the vicinity of its leading edge, the soaring interface can be considered as an analog of a shock wave, because in its vicinity, the continuity condition for the velocity normal component is violated. In high-velocity hydrodynamics, shock waves separating spatial domains with different values of the velocity normal component have been rather thoroughly studied [10]. In low-velocity hydrodynamics, such flow components have yet to be observed.

The perturbations that arrived at the soaring interface are accumulated with time. The fluid inflow attains the leading edge, interacts with the external flow, and forms a vortex head. The internal vortex is stretched by the accelerated flow between the wake and the interface (Fig. 1b). The external vortex remains more compact. Wave-field structures and wavelengths in the layer between the soaring interface and the density wake, as well as in free space, noticeably differ.

The homogeneity of the phase structure for the attached internal waves is restored with the distance to the body. Here, while intersecting the soaring interface, the crests and troughs conserve their features. As the distance from the obstacle increases, the soaring interface assumes the features of a tangential velocity discontinuity possessing an internal high-gradient interface.

Vortex heads for the leading edges of solitary interfaces, in turn, deform the regular pattern of attached internal waves [3]. The forward shell of the soaring vortex contacts the crest of the first attached internal wave in the lower half-space. The trough of the second wave approaches the interface; it is then curved and merges with the external shell of the pair of soaring interfaces. The crest of the second wave in the vicinity of the soaring interface is split into two parts. One of them is oriented toward the vortex head upstream of the main flow. The second one is directed oppositely. It intersects the soaring interface and attains the wake external shell. Here, it conjugates with the wave trough in the upper half-space (Fig. 1b). These flow components can significantly affect the redistribution and anomalously rapid transfer of passive admixtures, which is often observed in natural systems, e.g., in the atmosphere and ocean.

For all other waves, the phase structure does not vary as it approaches the wake axis, although shear flows cause appreciable deformation of phase surfaces. As the size of the second pair of vortices immersed in the density wake increases, both the internal-wave amplitude and displacements of the soaring interface increase, which promotes the formation of the second soaring vortex. Like the first one, it is localized in the domain of the minimal density-wake height (Fig. 1c).

In stabilized flow, two pairs of soaring vortices (above and below the density wake) correspond to each pair of immersed vortex bundles. The size of central vortices (5 cm) is comparable with the cylinder diameter at a distance of 5.4 cm from its trailing edge, the distance between their centers being 7 cm. The minimal wake height at a distance of 2.2 cm from the obstacle equals 0.8 cm. The vertical size of the soaring vortex is 2.8 cm. In this regime, the total height (11 cm) of the domain of both vortex and small-scale perturbations significantly exceeds the cylinder diameter.

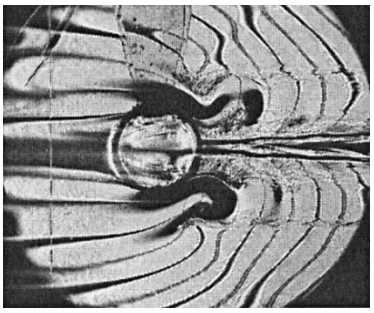

Fig. 2. Solitary vortices near the horizontal cylinder in a strongly stratified fluid (T_b = 7.4 s; D = 5 cm; U = 0.31 cm s^{-1}; Fr = 0.07; and Re = 155).

As the buoyancy period is reduced, the wave length of the attached internal wave that determines the repetition period for vortex systems in the wake also decreases (Fig. 2). The stratification suppresses the vertical motion, and only a single vortex pair is formed in the density wake. In this case, the gradients in the central part of the wake, which map the domain of the incident flow, become sharp. The amplitude of the waves and the corresponding light-beam deviations increase, so that shadowing light beams by the design members of the shadow device occurs, and dark spots are observed in the flow pattern near the cylinder (Fig. 2).

The forward surface of the vortex head becomes denser, and the anticyclonic vortex is flattened, whereas the cyclonic vortex loses its well-defined shape. The waviness system observed in Fig. 2, as opposed to the clear high-gradient interface (Fig. 1), testifies to the flow inhomogeneity along the cylinder generatrix. At the same time, the contrast shape of certain components allows us to make the conclusion that the high-gradient interface remains thin in each vertical cross section.

The range of parameters for the existence of soaring interfaces and solitary vertices, which were found in this experiment, is consistent with the flow-regime diagrams obtained in [1, 4]. As the flow velocity increases, the wake transforms into the narrower turbulent wake. These features disappear in the internal-wave field.

ACKNOWLEDGMENTS

This work was supported by the Russian Academy of Sciences in the framework of the Program “Dynamics and Acoustics of Inhomogeneous Fluids, Gas–Liquid Mixtures, and Suspensions” under the aegis of the OÉMMPU and by the Russian Foundation for Basic Research, project no. 05-05-64090.

REFERENCES

1. D. L. Boyer and P. A. Davies, Annu. Rev. Fluid. Mech. **32** (165), 165 (2000).
2. K. N. Fedorov, *Fine Thermohaline Structure of Ocean Water* (Gidrometeoizdat, Leningrad, 1976) [in Russian].
3. Yu. D. Chashechkin and V. V. Mitkin, Dokl. Akad. Nauk **362**, 625 (1998) [Dokl. Phys. **43**, 636 (1998)].
4. Yu. D. Chashechkin and V. V. Mitkin, Dokl. Akad. Nauk **373**, 767 (2000) [Dokl. Phys. **45**, 430 (2000)].
5. J. Lighthill, *Waves in Fluids* (Cambridge Univ. Press, Cambridge, 1978; Mir, Moscow, 1981).
6. Yu. D. Chashechkin and A. V. Kistovich, Dokl. Akad. Nauk **393**, 776 (2003) [Dokl. Phys. **48**, 710 (2003)].
7. L. A. Vasil'ev, *Schlieren Methods* (Nauka, Moscow, 1968; Israel Program for Scientific Translations, Jerusalem, 1971).
8. S. A. Smirnov, Yu. D. Chashechkin, and Yu. S. Il'inykh, Izmer. Tekh., No. 6, 15 (1998).
9. Yu. V. Kistovich and Yu. D. Chashechkin, Prikl. Mekh. Tekh. Fiz. **39** (5), 88 (1998).
10. L. D. Landau and E. M. Lifshitz, *Fluid Mechanics*, 2nd ed. (Nauka, Moscow, 1986; Pergamon, Oxford, 1987).

Translated by G. Merzon

Doklady Physics, Vol. 50, No. 9, 2005, pp. 457–458. Translated from Doklady Akademii Nauk, Vol. 404, No. 2, 2005, pp. 181–183.
Original Russian Text Copyright © 2005 by Barinov, Kuznetsov, Skomorokhov, Chernyshev.

MECHANICS

Mach Number of Drag Convergence for the Riabouchinsky Nose Part of a Body of Revolution in a Near-Sonic Gas Flow

V. A. Barinov, E. N. Kuznetsov, S. I. Skomorokhov, and I. L. Chernyshev

Presented by Academician G.S. Byushgens April 19, 2005

Received May 14, 2005

Bodies optimal with respect to the critical Mach number were studied in [1]. In particular, it was shown that, in the flow around a body of revolution of a given length and volume, the critical Mach number M_* is maximal when the body is of the Riabouchinsky cavity shape [2]. The speed of sound is reached on the free flow surface connecting the disks. However, in order to solve a number of aerodynamic problems, it is important to know the so-called upper critical Mach number M_{**} above which no continuous flow is possible [3], as opposed to the critical Mach number M_* at which the local velocity reaches the speed of sound. The upper critical Mach number is reached when $\frac{dC_x}{dM} = 0.1$, where C_x is the drag coefficient and M is the Mach number of the airflow [4].

To determine this number, we conduct a wind-tunnel investigation of the flow around the Riabouchinsky disk-shaped nose parts with specific length $\lambda = \frac{L}{D} = 0.87$ and 2.5, where L is the length of the nose part and D is the diameter of its maximum midsection, as well as the ogive nose [4] with $\lambda = 3.5$ coupled to the body of revolution (as is evident from Fig. 1) with total specific length $\Lambda = 8.5$, 9, 10 in the ADT-106M TsAGI wind tunnel. Its working-section diameter is 2.48 m, and its length was 4.84 m. The diameter of the maximum midsection of the model was $D = 0.17$ m. The model was mounted on the strip suspension. The measurement data were corrected for the drag of the suspension rollers by the value of 0.008594, which was constant for different Mach numbers. The instrumental error for drag (in the gas flow) is ±0.05% of the maximum load of the scale. The drag coefficient C_x is related to the midsection area $S = 0.0229$ m^2 of the model. The experimental investigation was carried out for Mach numbers M = 0.7–0.98 and angle of attack $\alpha = 0$. The Reynolds numbers were $Re_D = (3.05–3.34) \times 10^6$ for the Riabouchinsky nose parts and $Re_D = (3.02–3.31) \times 10^6$ for the ogive nose. The values of the Reynolds number Re_D are related to the midsection diameter of the nose part. The point of laminar–turbulent transition is fixed at the distance $X_{tr} = 3\%$ of the model length from the nose by means of rough hills that had a height of 0.1 mm and were spaced by a distance of 2 mm.

Figure 2 shows drag coefficients $C_x(M)$ measured for the model with the Riabouchinsky nose part having $\lambda = 0.87$ in the ADT-106M TsAGI and ADT-112 TsAGI [5] wind tunnels. We took into account that the models in these wind-tunnel experiments had different lengths and, consequently, different drag coefficients. The calculated drag coefficient $C_x(M, M_{**})$ [4] that is also presented in Fig. 2 is in good agreement with experimental data for $M_{**} = 0.815$.

Figure 3 shows drag coefficients $C_x(M)$ measured for the model with the Riabouchinsky nose part with $\lambda = 2.5$ and with the nose ogive with $\lambda = 3.5$. The coef-

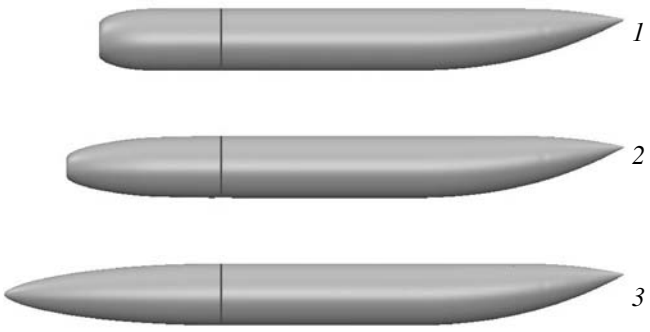

Fig. 1. Models under investigation: (*1*) with the Riabouchinsky nose part, $\lambda = 0.87$, (*2*) with the Riabouchinsky nose part, $\lambda = 2.5$, and (*3*) with the ogive nose, $\lambda = 3.5$.

Central Aerohydrodynamic Institute (TsAGI), Zhukovsky, Moscow oblast, 140180 Russia

1028-3358/05/5009-0457$26.00 © 2005 Pleiades Publishing, Inc.

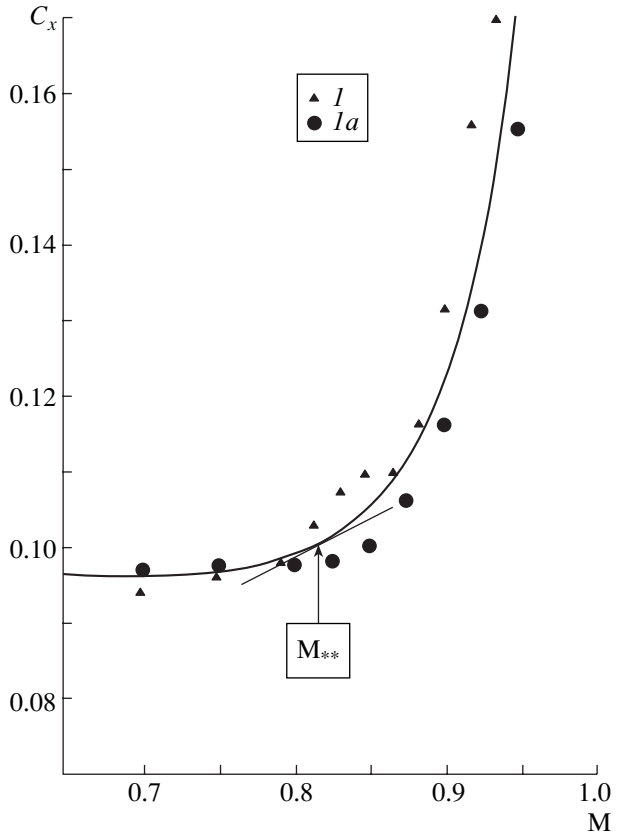

Fig. 2. Drag coefficients (triangles) measured for the model used and the test data (circles) taken from [5].

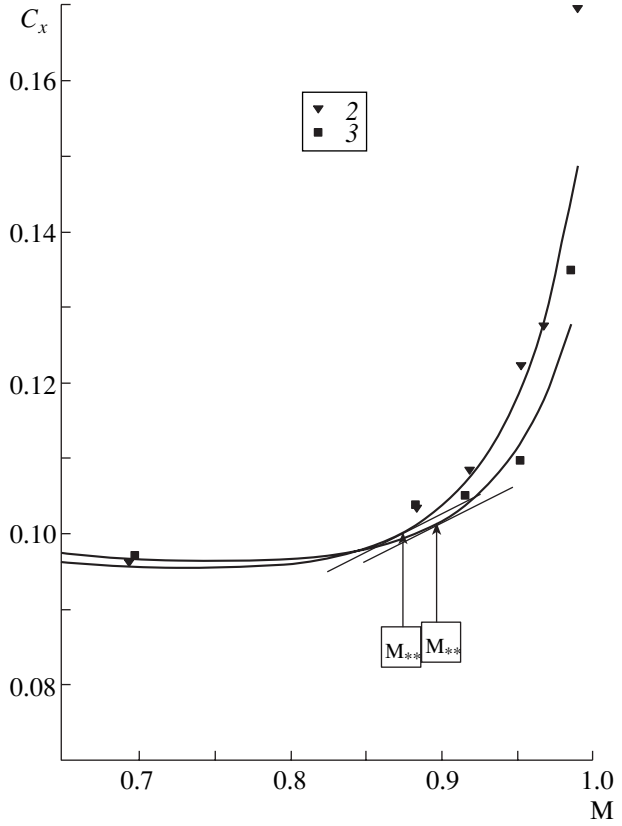

Fig. 3. Drag coefficients as functions of Mach number.

ficients $C_x(M, M_{**})$ calculated at $M_{**} = 0.875$ for the Riabouchinsky nose part and at $M_{**} = 0.895$ for the ogive nose are also presented in Fig. 3.

As follows from Fig. 4, the test data for the nose parts under investigation are in a good agreement (within 3%) with the plot of $M_{**}(\lambda)$ that is often used in applied aerodynamics and for designing aircrafts [6].

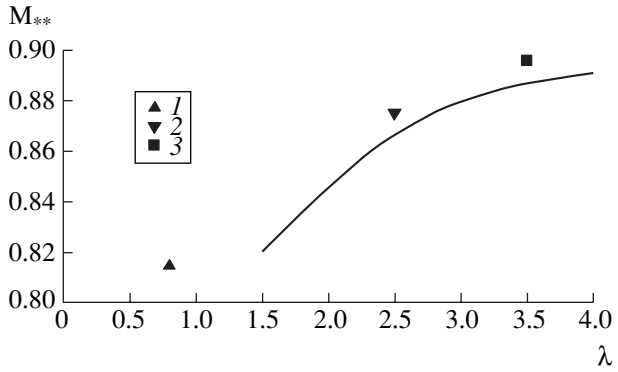

Fig. 4. Upper critical Mach numbers $M_{**}(\lambda)$ for three models and the test data.

REFERENCES

1. D. Gilbarg and M. Shiffman, Arch. Ration. Mech. Anal. **3** (2), 209 (1954).
2. D. Riabouchinsky, Proc. London Math. Soc. **19** (2), 206 (1920).
3. T. Karman, J. Atmos. Sci. **14** (7), 373 (1947).
4. *Machinery Construction. Encyclopedia* (Mashinostroenie, Moscow, 2002), Vol. 4 [in Russian].
5. V. V. Vyshinskiĭ and E. N. Kuznetsov, Dokl. Akad. Nauk SSSR **321** (1), 33 (1991) [Sov. Phys. Dokl. **36**, 731 (1991)].
6. K. P. Petrov, *Aerodynamics of Aircraft Elements* (Mashinostroenie, Moscow, 1985) [in Russian].

Translated by E. Kuznetsov

Doklady Physics, Vol. 50, No. 9, 2005, pp. 459–462. Translated from Doklady Akademii Nauk, Vol. 404, No. 2, 2005, pp. 184–187.
Original Russian Text Copyright © 2005 by Kistovich, Chashechkin.

MECHANICS

Reflection of Capillary-Gravity Waves by Surface Convection Domains

A. V. Kistovich and Yu. D. Chashechkin

Presented by Academician D.M. Klimov March 24, 2005

Received April 1, 2005

The detailed investigation of capillary waves is associated with the search for physical mechanisms of the formation of signals stipulated by the topography [1], internal waves [2], and other processes occurring in the ocean interior. We confront these problems, e.g., in the analysis of radar-image patterns for free ocean surface [3]. A review of the present state of the art for the linear and nonlinear theories of gravity-capillary waves in the vicinity of the phase-velocity minimum is given in [4], and the effect of viscosity on the damping and generation of short waves was considered in [5].

Under actual conditions, the temperature and concentration of substances on the ocean surface is not constant. Near-surface convection processes produce gradients of the surface-tension coefficient, which, in turn, affects the short-wave sea-way [6]. The interaction of waves with regular structures arising as a result of near-surface convection or of rainfalls is of particular interest [3]. In the present paper, we have constructed, for the first time, a model for the propagation of capillary-gravity waves in a viscous temperature-inhomogeneous medium with allowance for the corresponding near-surface boundary layers.

We consider the transformation of a surface wave of frequency ω, which propagates from the left to the domain $x \in [0, D]$ containing N identical cells of size L, $D = NL$, with a quasi-stationary temperature distribution. In the absence of waves, the water surface is assumed to be planar: $z = 0$, z being the vertical axis aligned oppositely to the gravity-force vector **g**. The fluid-surface temperature that determines the kinematic viscosity $\nu(x) = \nu(T(x))$ and the surface-tension coefficient $\alpha(x) = \alpha(T(x))$ is given by the spectral expansion

$$T(x) = T_0 + \begin{cases} \Delta T \sum_{n=1}^{\infty} c_n \sin(2\mu n x), & x \in [0, D] \\ 0, & x \in (-\infty, 0] \cup [D, +\infty). \end{cases} \quad (1)$$

Institute for Problems in Mechanics,
Russian Academy of Sciences,
pr. Vernadskogo 101/1, Moscow, 119526 Russia
e-mail: chakin@ipmnet.ru

Here, ΔT is overheating inside a cell, $\mu = \dfrac{\pi}{L}$ is the wave number of a periodic convective structure, and c_n are the spectral coefficients.

For small deviations $\zeta(t, x)$ of the disturbed surface, the set of equations of motion and of boundary conditions is linearized and takes the form [7]

$$\begin{gathered} u_t' = -p_x' + 2[\nu u_x']_x' + [\nu(u_z' + w_x')]_z', \\ w_t' = -p_z' + [\nu(u_z' + w_x')]_x' + 2[\nu w_z']_z' - g, \\ u_x' + w_z' = 0, \quad p - p_0 + \alpha\zeta_{xx}'' - 2\nu w_z'\big|_{z=\zeta} = 0, \\ \nu(u_z' + w_x') + \alpha_x'\big|_{z=\zeta} = 0, \quad w - \zeta_t' - u\zeta_x'\big|_{z=\zeta} = 0. \end{gathered} \quad (2)$$

Here, $\mathbf{u} = (u, w)$ is the fluid-velocity vector; p is pressure in water; p_0 is atmospheric pressure; and α is the surface-tension coefficient. All the quantities are normalized to the average fluid density ρ. Under actual conditions, temperature variations ΔT are small, and the values of ν and α inside the convection domain are given in the form of expansions in the vicinity of the basis temperature T_0 [8]:

$$\begin{aligned} \nu(T(x)) &= \nu\left(T_0 + \Delta T \sum_{n=1}^{\infty} c_n \sin(2\mu n x)\right) \\ &\approx \nu(T_0) + \nu_T'(T_0)\Delta T \sum_{n=1}^{\infty} c_n \sin(2\mu n x), \\ \alpha(T(x)) &= \alpha\left(T_0 + \Delta T \sum_{n=1}^{\infty} c_n \sin(2\mu n x)\right) \\ &\approx \alpha(T_0) + \alpha_T'(T_0)\Delta T \sum_{n=1}^{\infty} c_n \sin(2\mu n x). \end{aligned} \quad (3)$$

Using small parameters

$$\varepsilon = \left|\frac{\nu_T'(T_0)\Delta T}{\nu(T_0)}\right| \ll 1, \quad \delta = \left|\frac{\alpha_T'(T_0)\Delta T}{\alpha(T_0)}\right| \ll 1, \quad \nu = \nu(T_0), \quad \alpha = \alpha(T_0), \quad (4)$$

1028-3358/05/5009-0459$26.00 © 2005 Pleiades Publishing, Inc.

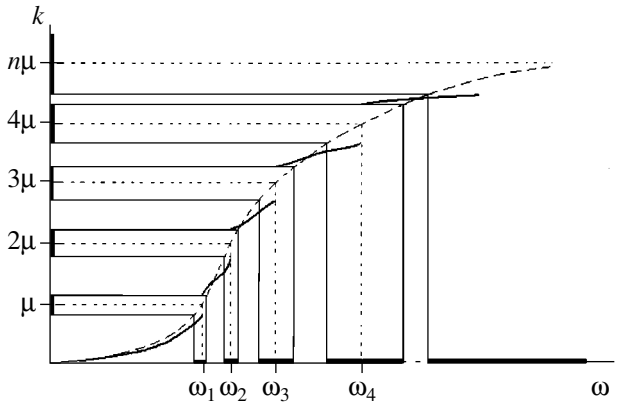

Dispersion curves for nonuniformly heated liquid (dashed lines) and periodically uniformly heated liquid (solid lines). Forbidden zones are shown by thick segments in the coordinate axes.

we can represent these formulas in the more compact form:

$$\nu(x) = \nu(1 + \varepsilon\tau(x)), \quad \alpha(x) = \alpha(1 + \delta\tau(x)),$$
$$\tau(x) = \sum_{n=1}^{\infty} c_n \sin(2\mu n x). \tag{5}$$

Introducing the stream function Ψ ($u = \Psi'_z$, $w = -\Psi'_x$), substituting $p = p_0 + g(\zeta - z) + \tilde{p}$, linearizing and reducing boundary conditions to the level $z = 0$, and allowing for (4), (5), we can reduce Eqs. (2) to the form

$$\left(\frac{\partial}{\partial t} - \nu\Delta\right)\Delta\Psi = \nu\varepsilon(\Delta(\tau\Delta\Psi) - 2\tau''_{xx}\Psi''_{zz}),$$

$$\Psi''_{zz} - \Psi''_{xx}\big|_{z=0} = 0,$$
$$g\Psi''_{xx} - \Psi'''_{ztt} + \nu\Delta\Psi''_{zt} - \alpha\Psi^{\mathrm{IV}}_{xxxx} + 2\nu\Psi^{\mathrm{IV}}_{xxzt} \tag{6}$$
$$+ \nu\varepsilon(4\tau'_x\Psi'_x + \tau\Delta\Psi + 2\tau\Psi''_{xx})''_{zt} - \alpha\delta(\tau\Psi'''_{xxx})'_x\big|_{z=0} = 0.$$

If the viscosity and surface tension are independent of temperature ($\varepsilon = \delta = 0$), then expressions (6) are transformed into the standard set of equations for short surface waves [7]. We find the solution to Eqs. (6) in the class of harmonic oscillations, namely,

$$\Psi(x, z, t) = \Psi(x, z)e^{-i\omega t}.$$

In the convection domain, ($\varepsilon = \delta = 0$), waves of amplitudes A_+ and A_- with associated periodic boundary layers (of amplitudes B_+ and B_-) propagate, respectively, along the positive and negative directions of the x axis. Outside of this domain, the stream function Ψ is of the form

$$\Psi = e^{kz}(A_+e^{ikx} + A_-e^{-ikx}) + e^{k_b z}(B_+e^{ikx} + B_-e^{-ikx}),$$
$$k_b^2 = k^2 - i\frac{\omega}{\nu}, \quad \mathrm{Re}k, \quad \mathrm{Im}k > 0, \quad \mathrm{Re}k_b > 0. \tag{7}$$

The choice of signs for the real and imaginary parts of the wave numbers k and k_b is based on the perturbation-damping conditions as $x \longrightarrow \pm\infty$ and $z \longrightarrow -\infty$.

Substituting expression (7) into the boundary conditions of the set of Eqs. (6), we arrive at two sets of equations that connect the amplitudes $A_\pm$ and $B_\pm$ together:

$$2k^2A_\pm - (k_b^2 + k^2)B_\pm = 0,$$
$$k(\omega^2 - gk - \alpha k^3 + 2i\omega\nu k^2)A_\pm \tag{8}$$
$$+ (\omega^2 k_b - gk^2 - \alpha k^4 + 2i\omega\nu k_b(3k^2 - k_b^2))B_\pm = 0.$$

For them, the compatibility condition

$$2k(\omega^2 k_b - gk^2 - \alpha k^4 + 2i\omega\nu k_b(3k^2 - k_b^2))$$
$$-(k_b^2 + k^2)(\omega^2 - gk - \alpha k^3 + 2i\omega\nu k^2) = 0 \tag{9}$$

is the dispersion equation for capillary-gravity waves.

As follows from the set of Eqs. (8), waves and boundary layers appear or disappear simultaneously, whereas the amplitudes of the wave ($A_\pm$) and boundary-layer ($B_\pm$) parts of surface oscillations are rigidly bound together.

With allowance for the thermodynamic parameters of water (see [8]), Eq. (9) has the unique physically admissible solution:

$$k = k_* + \frac{4\omega\nu k_*^2}{g + 3\alpha k_*^2}\left[-k_*\sqrt{\frac{\nu}{2\omega}} + i\left(1 + k_*\sqrt{\frac{\nu}{2\omega}}\right)\right], \tag{10}$$

where k_* is the root of the dispersion equation $\omega^2 - gk - \alpha k^3 = 0$ for capillary-gravity waves in a perfect liquid. (The root is unique provided that the conditions $\mathrm{Re}k$, $\mathrm{Im}k > 0$ are true [7]; the dispersion curve is shown in the figure by the dashed line.) As also follows from expressions (8),

$$\frac{A_-}{A_+} = \frac{B_-}{B_+} = \beta = \frac{2\nu k^2}{i\omega - 2\nu k^2}. \tag{11}$$

The wave incident onto the convective zone

$$\Psi_{in} = (e^{kz} + \beta e^{k_b z})e^{ikx}$$

is in part reflected:

$$\Psi_r = R(e^{kz} + \beta e^{k_b z})e^{-ikx}$$

and in part transmitted:

$$\Psi_t = T(e^{kz} + \beta e^{k_b z})e^{ik(x-D)}.$$

Here, R and T are the coefficients to be determined.

Taking into account the smallness of ε and δ, we seek the solution to Eqs. (6) in the form of expansion

$$\Psi = \Psi_0 + \varepsilon\Psi_\nu + \delta\Psi_\alpha + \ldots, \quad (12)$$

$$\Psi_0 = \Psi_w + \Psi_b = e^{\tilde{k}_w z}(G_+ e^{i\tilde{k}x} + G_- e^{-i\tilde{k}x}) + e^{\tilde{k}_b z}(H_+ e^{i\tilde{k}x} + H_- e^{-i\tilde{k}x}), \quad (13)$$

$$\tilde{k} = k + \varepsilon\Delta k_\nu + \delta\Delta k_\alpha, \quad \tilde{k}_w = k + \varepsilon\Delta k_{w\nu} + \delta\Delta k_{w\alpha},$$

$$\tilde{k}_b = k_b + \varepsilon\Delta k_{b\nu} + \delta\Delta k_{b\alpha}.$$

In this case, the quantity k is determined by relationship (10).

Substituting expressions (12) and (13) into Eqs. (6) and separating terms of the same order of smallness in ε and δ, we arrive at two sets of equations with respect to the function Ψ_ν and Ψ_α, which, being too cumbersome, are not given here. The solutions to these equations depend on the relation between the wave number $\tilde{k}$ of the incident wave and the Bragg wave numbers μm, $m = 1, 2, \ldots$ of periodic distributions (3) (see [9]).

In the nonresonance case $\tilde{k} \neq \mu m$, when the relationships

$$\Delta k_{w\nu} = \Delta k_\nu, \quad k_b\Delta k_{b\nu} = k\Delta k_\nu, \quad \Delta k_{w\alpha} = \Delta k_\alpha, \quad k_b\Delta k_{b\alpha} = k\Delta k_\alpha$$

are fulfilled, secular terms do not appear in expansions (12), (13), and with allowance for the second boundary conditions, the latter relationships take the form

$$\Delta k_\nu = \Delta k_\alpha = \Delta k_{w\nu} = \Delta k_{w\alpha} = \Delta k_{b\nu} = \Delta k_{b\alpha} = 0. \quad (14)$$

Variations of the kinematic viscosity with temperature slightly affect the dynamics of the nonresonance wave scattering. Cumbersome calculations show that in this case, the amplitudes of the forward (G_+, H_+) and backward (G_-, H_-) waves are weakly bound and, in the zero approximation (over ε and δ), i.e., when

$$R \approx 0, \quad T \approx \exp(ikD) \longrightarrow |T| \approx 1, \quad (15)$$

the action of the convection zone on surface waves is small.

Near the resonance, when $\tilde{k} \neq \mu m$, we find the solution using the slowly varying amplitudes (see [9]):

$$\Psi = \Psi_w + \Psi_b,$$

$$\Psi_w = e^{\lambda_w z}e^{-sx}(G_+(x)e^{i(\mu m + \Delta)x} + G_-(x)e^{i(\mu m + \Delta)x}), \quad (16)$$

$$\Psi_b = e^{\lambda_b z}e^{-sx}(H_+(x)e^{i(\mu m + \Delta)x} + H_-(x)e^{i(\mu m + \Delta)x}),$$

where $s = \mathrm{Im}\,\tilde{k}$, $\Delta = \tilde{k} - \mu m$ is the detuning from the resonance, and parameters λ_w and λ_b should be determined.

In the first approximation over viscosity, the action of the operator $\frac{\partial}{\partial z}$ in the case of boundary conditions (6) is described by the relationships

$$\frac{\partial}{\partial z}(e^{\lambda_w z}e^{-sx}G_\pm(x)e^{\pm i(\sigma+\Delta)x}) \Rightarrow \left[(\sigma \pm is)G_\pm \mp iG'_\pm \mp \frac{2\nu\varepsilon c_m\sigma^3}{\omega}G_\mp \exp(\mp 2i\Delta x)\right]e^{\lambda_w z}e^{-sx}e^{\pm i(\sigma+\Delta)x},$$

$$\frac{\partial}{\partial z}(e^{\lambda_b z}e^{-sx}H_\pm(x)e^{\pm i(\sigma+\Delta)x}) \quad (17)$$

$$\Rightarrow \left[\sqrt{\sigma^2 - \frac{i\omega}{\nu}}H_\pm \mp i\frac{\sigma}{\sqrt{\sigma^2 - \frac{i\omega}{\nu}}}H'_\pm \mp \frac{2\nu\varepsilon c_m\sigma^2\sqrt{\sigma^2 - \frac{i\omega}{\nu}}}{\omega}H_\mp \exp(\mp 2i\Delta x)\right]e^{\lambda_b z}e^{-sx}e^{\pm i(\sigma+\Delta)x},$$

where $\lambda_w = \sigma \pm is$, $\lambda_b = \sqrt{(\sigma \pm is)^2 - \frac{i\omega}{\nu}}$, and $\sigma = \mu m$.

Substitution of (16) into boundary conditions (6) with allowance for (17) results in the set of equations linking $G_\pm$ and $H_\pm$. The solution to this set is of the form

$$G_\pm = G_\pm^0 \exp(\pm\zeta x)\exp(\mp i\Delta x),$$

$$H_\pm = H_\pm^0 \exp(\pm\zeta x)\exp(\mp i\Delta x),$$

$$\zeta = \sqrt{\delta^2|\Delta k_m|^2 - \Delta^2}, \quad |\Delta k_m| = \frac{c_m\alpha|\sigma|^3}{2(g + 3\alpha|\sigma|^2)}, \quad (18)$$

$$|\sigma| = \sqrt{(\mu m)^2 + s^2}, \quad s = \frac{4\omega\nu(\mu m)^2}{g + 3\alpha(\mu m)^2}.$$

The multiplier $\exp(-sx)$ that characterizes the viscous damping is identical for waves running in both the positive and negative directions; i.e., the distributions of amplitudes of incident and reflected waves are similar in the convective zone.

In the resonance case, the surface wave is efficiently reflected from convection domains. In the zero approximation with respect to ε and δ, the values of the reflection ($|R| \approx 1$) and transmission ($|T| \approx 0$) coefficients are typical of the Bragg scattering [9].

In the nonviscous limit, there exists a manifold of wave numbers $\sigma = \mu m$ near which the properties of surface waves change. Forbidden zones of the width $\Delta\omega_m = \dfrac{\delta\Delta k_m}{\mu m}\omega_{Bm}$, which are generated by the resonant scattering on a periodic structure, never overlap (they are shown by thick lines in the coordinate axes of the figure). The dispersion curve $k(\omega)$ for surface waves, which was calculated on the basis of formula (9), is plotted by solid lines. It is divided into separate segments inside which the Bragg frequencies ω_{Bm} are located. They are defined by the relation

$$\omega_{Bm}^2 = \mu m(g + \alpha(\mu m)^2).$$

The incident wave is efficiently reflected from the convection domain under the condition

$$\Delta^2 = (k - \mu m)^2 < \delta^2|\Delta k_m|^2.$$

As follows from solution (18), the viscosity expands the opacity zones. In low-viscosity media, relationships (18) take the form

$$\zeta = \pm\sqrt{\delta^2|\Delta\sigma|^2(1 + \nu^2\varphi(\sigma)) - \Delta^2},$$
$$\varphi(\sigma) = \frac{24(g + \alpha(\mu m)^2)^2(\mu m)^3}{(g + 3\alpha(\mu m)^2)^3}, \qquad (19)$$

where $\Delta\sigma = \pm\dfrac{c_m(\alpha)(\mu m)^3}{2(g + 3\alpha(\mu m)^2)}$.

The shorter the wavelength of the incident wave, the larger the number m of the resonance harmonic and the stronger the manifestation of the viscosity effect in the resonance case. A part of the incident packet of surface waves, which satisfies the Bragg resonance condition, is efficiently reflected from the convection zone and generates standing waves in the domain $x < 0$. The rest part of the packet escapes from the convection zone with the thinned out spectral characteristic. Thus, the Marangoni convection domain plays the role of an efficient band-pass filter.

The approximation of the quasi-stationary temperature distribution, which was used in the calculations, is true when u, $\chi k \ll c_{ph}$, where k and c_{ph} are the wave number and wave phase velocity, u is the characteristic rate of the convective temperature transfer, and χ is the thermal-diffusivity coefficient of the medium. For water ($u \sim 1$–10 cm s^{-1}, $\chi \approx 1.43 \times 10^{-3}$ cm^2 s^{-1}), these conditions are always fulfilled.

REFERENCES

1. C. P. Summerhayes and S. A. Thorpe, *Oceanography* (Manson, Southhampton, 1996).
2. K. N. Fedorov and A. I. Ginzburg, *Near-Surface Layer in Ocean* (Gidrometeoizdat, Leningrad, 1988) [in Russian].
3. V. Yu. Raĭzer and I. V. Chernyĭ, *Microwave Diagnostics of the Near-Surface Layer of Ocean* (Gidrometeoizdat, St. Petersburg, 1994) [in Russian].
4. F. Dias and C. Kharif, Annu. Rev. Fluid Mech. **31**, 301 (1999).
5. M. Perlin and W. W. Schultz, Annu. Rev. Fluid Mech. **32**, 241 (2000).
6. A. A. Lazarev, K. V. Pokazeev, and N. K. Shelkovnikov, *Physico-Chemical Inhomogeneity of Ocean Surface and Surface Waves* (Mos. Gos. Univ., Moscow, 1987) [in Russian].
7. L. D. Landau and E. M. Lifshitz, *Fluid Mechanics*, 2nd ed. (Nauka, Moscow, 1986; Pergamon Press, Oxford, 1987).
8. *Tables of Physical Data: Reference Book*, Ed. by I. K. Kikoin (Atomizdat, Moscow, 1976) [in Russian].
9. M. B. Vinogradova, O. V. Rudenko, and A. P. Sukhorukov, *The Theory of Waves* (Nauka, Moscow, 1979) [in Russian].

Translated by G. Merzon

Doklady Physics, Vol. 50, No. 9, 2005, pp. 463–466. Translated from Doklady Akademii Nauk, Vol. 404, No. 2, 2005, pp. 188–191.
Original Russian Text Copyright © 2005 by Malashin.

MECHANICS

Longitudinal and Torsional Waves and Vibrations in Stressed Thin-Walled Tubes

A. A. Malashin

Presented by Academician E.I. Shemyakin March 28, 2005

Received April 4, 2005

In this study, differential equations for the torsional and longitudinal motions of thin-walled tubes are obtained with allowance for the interference of motions. General solutions to these equations are found for the case of the torsion of an infinitely long tube under action at a constant angular velocity. Linearized equations for torsional and longitudinal vibrations are obtained. The contributions of torsional and longitudinal components to dynamic loading are shown to be of the same order of magnitude. The longitudinal components of the velocities and strains exhibit a break on torsional waves. The equation for longitudinal vibrations is inhomogeneous, torsional components playing the role of a stimulating force for longitudinal ones. The appearance of torsional motions gives rise to the formation of longitudinal ones. Vibrations in the longitudinal direction occur at both natural frequencies and at the frequencies of torsional vibrations.

DERIVATION OF DIFFERENTIAL EQUATIONS FOR TORSIONAL–LONGITUDINAL MOTIONS

We consider a thin-walled (cylindrical) tube of average radius R and of wall thickness h. (Because in this case $h \ll R$, we can consider R to be the radius of the middle surface and use it to describe the position of tube components.) We direct the OX axis along the tube axis. Using the laws of variation of the kinetic momentum and of the moment of momentum to a tube element of length Δs, we can, by analogy with [1], derive equations for the longitudinal and torsional motions of a thin-walled tube in the form

$$\rho_l \frac{\partial^2 \mathbf{l}}{\partial t^2} = \frac{\partial \mathbf{Q}}{\partial s} + \mathbf{q}, \quad J\frac{\partial^2 \boldsymbol{\varphi}}{\partial t^2} = \frac{\partial \overline{M}}{\partial s} + \boldsymbol{\mu}. \qquad (1)$$

Here, s is the Lagrangian coordinate that coincides with the longitudinal Cartesian coordinate x of the undeformed tube; ρ_l is its linear density; $\mathbf{Q}$ and $\mathbf{M}$ are the vectors of forces and of moments acting on the cross-section area; $\mathbf{l}$ and $\boldsymbol{\varphi}$ are, respectively, the vectors of the linear and angular displacements for the given cross section; J is the polar moment of inertia for the tube cross section; and $\mathbf{q}$ and $\boldsymbol{\mu}$ are the linear densities of external forces and moments.

For simultaneous torsional and longitudinal motions, a linear element of length Δs of a thin-walled tube transforms into an element of length

$$\Delta l = \sqrt{(\Delta s + x(s+\Delta s, t) - x(s,t))^2 + r^2(\varphi(s+\Delta s, t) - \varphi(s,t))^2}$$

and thereby, has the relative elongation

$$e = \frac{\Delta l - \Delta s}{\Delta s} = \sqrt{\left(1 + \frac{\partial x}{\partial s}\right)^2 + r^2\left(\frac{\partial \varphi}{\partial s}\right)^2} - 1.$$

The inclination angle of the given element to the cylindrical generatrix of the tube's middle surface is determined by the formulas

$$\cos\gamma = \frac{1 + \frac{\partial x}{\partial s}}{1+e}, \quad \sin\gamma = \frac{r\frac{\partial \varphi}{\partial s}}{1+e}.$$

In this case, the longitudinal and torsional (angular) strains are written as

$$e_x = e\cos\gamma, \quad e_\varphi = (1+e)\sin\gamma.$$

In the case of a decomposition into the longitudinal

Moscow State Forest University, Mytishchi, Moscow oblast, Russia

1028-3358/05/5009-0463$26.00 © 2005 Pleiades Publishing, Inc.

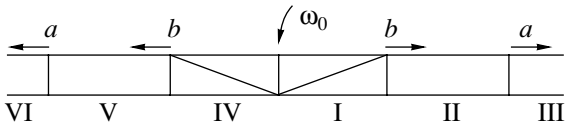

Figure.

and torsional components, Eqs. (1) can be represented in the form

$$J\frac{\partial^2\varphi}{\partial t^2} = \frac{\partial}{\partial s}\left(2\pi\int\limits_{R-h/2}^{R+h/2} G\frac{r\dfrac{\partial\varphi}{\partial s}}{1+e}r^2dr\right),$$

$$\rho D\frac{\partial^2 x}{\partial t^2} = \frac{\partial}{\partial s}\left(2\pi\int\limits_{R-h/2}^{R+h/2} Ee\frac{1+\dfrac{\partial x}{\partial s}}{1+e}rdr\right),$$

where E and G are elastic and shear moduli, respectively; ρ is the material density; and D is the cross-section area.

By virtue of the condition $h \ll R$ and of the mean-value theorem, we arrive at the equations for the torsional–longitudinal motion of a thin-walled tube:

$$\rho\frac{\partial^2\varphi}{\partial t^2} = \frac{\partial}{\partial s}\left(G\frac{\partial\varphi}{\partial s}\right), \quad \rho\frac{\partial^2 x}{\partial t^2} = \frac{\partial}{\partial s}\left(Ee\frac{1+\dfrac{\partial x}{\partial s}}{1+e}\right), \quad (2)$$

where

$$e = \sqrt{\left(1+\frac{\partial x}{\partial s}\right)^2 + R^2\left(\frac{\partial\varphi}{\partial s}\right)^2} - 1. \quad (3)$$

SOLVING EQUATIONS IN THE CASE OF A PERMANENT TUBE-TWISTING VELOCITY

At a certain instant of time, let a tangent action begin to twist a tube at a constant angular velocity ω_0. Here we imply a point action, i.e., an action that can be represented by a zero-width line tangent to the tube surface.

We now introduce the dimensionless variables

$$\bar{x} = \frac{x}{R\omega_0 t}, \quad \bar{\varphi} = \frac{\varphi}{\omega_0 t}.$$

The quantities $\bar{x}$ and $\bar{\varphi}$ can depend only on dimensionless parameters $z = \dfrac{s}{R\omega_0 t}$.

Equations (2) written out in terms of the given variables are

$$z^2\bar{x}'' = \frac{d}{dz}\left(A\bar{e}\frac{1+\bar{x}'}{1+\bar{e}}\right), \quad z^2\bar{\varphi}'' = \frac{d}{dz}(B\bar{\varphi}'), \quad (4)$$

where

$$1+\bar{e} = \sqrt{(1+\bar{x}')^2 + \bar{\varphi}'^2}, \quad A = \frac{E}{\rho R^2\omega_0^2}, \quad B = \frac{G}{\rho R^2\omega_0^2}.$$

The general integrals of this set of equations can be represented in the form

$$R\varphi = C_3 s + C_4 t, \quad x + s = C_1 R\varphi + C_2 t,$$
$$x + s = C_5 s + C_6 t,$$

$$\left(\frac{s}{t}\right)^2 = a^2 = \frac{E}{\rho}, \quad \left(\frac{s}{t}\right)^2 = \frac{G}{\rho}.$$

The solutions obtained imply that only domains of permanent strains arise in the tube. Two elastic waves propagate along the tube at a velocity $b < a$. At an arbitrary instant of time, the tube shape has the following form (see figure): I and IV are the regions of torsional and longitudinal strains (in this case, the inclination angle of linear elements to the tube cylindrical generatrix remains constant); II and V are the regions of longitudinal-strain propagation (back of the elastic wave); and III and VI are the rest regions.

The solutions obtained make it possible to determine the relationships for the torsional-wave front (by analogy with the relationships for the transverse-wave front [2]).

The mass conservation law

$$\rho_2 D_2(b+u) = \rho_1 D_1(b+V_l)$$

with the relation

$$\rho_0 = \rho_1(1+e_1)\cos\gamma = \rho_2(1+e_2)$$

taken into account lead to the equation

$$\frac{b+u}{1+e_1} = \frac{b+V_l}{(1+e_2)\cos\gamma}. \quad (5)$$

Here, b is the velocity of the torsional-wave front; ρ_i and e_i are, respectively, the density and strain of elements in the corresponding regions of the figure; $V_l = V\cos\beta$ is the longitudinal component of the linear velocity for the tube particle's velocity within region I; and β is the inclination angle of the tube-particle's velocity vector to the tube cylindrical generatrix. In this case, $V\sin\beta = R\omega$.

Application of the conservation laws for both the kinetic momentum and moment of momentum results in the following relations on the torsional wave:

$$\rho_0(b+u)(V\cos\beta - u) = E(e_1\cos\gamma - e_2)(1+e_2), \quad (6)$$

$$\rho_0(b+u)V\sin\beta = G\sin\gamma(1+e_1)(1+e_2). \quad (7)$$

The following kinematic relationship takes place:

$$V\sin(\beta-\gamma) = b\sin\gamma. \quad (8)$$

Combined with the relationship $u = a(e_2 - e_0)$ at the longitudinal wave, Eqs. (5)–(8) form a closed set of equations for the determination of the velocities and strains, i.e., quantities b, γ, u, e_1, and e_2.

In the framework of this study, we solve the problem of an action on a tube (under the presence of a certain stretching stress) at a constant velocity ω_0 of the angular rotation in the transverse direction to its generatrices (under the condition $\omega_0 R \ll b$ and, hence, small angles γ). For short time intervals, in which the waves do not attain the tube edges, the wave pattern is analogous to that presented in the figure. The set of Eqs. (5)–(8) admits the solution

$$b \approx \sqrt{\frac{G}{\rho_0}}(1+e_0), \quad \tan\gamma = \frac{\omega_0 R}{b}, \quad e_1 - e_0 \sim \left(\frac{\omega_0 R}{b}\right)^2, \quad e_2 - e_0 \sim \frac{(\omega_0 R)^2}{ab}. \quad (9)$$

DERIVATION OF LINEARIZED EQUATIONS FOR TORSIONAL AND LONGITUDINAL WAVES AND VIBRATIONS

Let a tube be preliminarily stressed in the longitudinal direction, its initial strain being e_0. We consider the case of small-angle rotation and low angular velocities. The longitudinal displacement can be represented as $x = e_0 s + \hat{x}$, where $\hat{x}$ is the dynamic component of the longitudinal displacement. The strain can be described in the form

$$e = \sqrt{\left(1 + e_0 + \frac{\partial\hat{x}}{\partial s}\right)^2 + R^2\left(\frac{\partial\varphi}{\partial s}\right)^2} - 1.$$

With allowance for $e_0 \gg \frac{\partial\hat{x}}{\partial s}$ and $e_0 \gg R\frac{\partial\varphi}{\partial s}$, this expression is linearized:

$$e = e_0 + \frac{\partial x}{\partial s} + \frac{R^2}{2(1+e_0)}\left(\frac{\partial\varphi}{\partial s}\right)^2. \quad (10)$$

After taking into account this fact, the set of Eqs. (2) is written out in the form

$$\rho\frac{\partial^2\varphi}{\partial t^2} = G\frac{\partial^2\varphi}{\partial s^2}, \quad (11)$$

$$\rho\frac{\partial^2 x}{\partial t^2} = E\frac{\partial}{\partial s}\left(\frac{\partial x}{\partial s} + \frac{R^2}{2(1+e_0)}\left(\frac{\partial\varphi}{\partial s}\right)^2\right). \quad (12)$$

The set of Eqs. (2) can also be linearized by asymptotic methods. To this end, we choose the dynamic component of the total strain $\varepsilon = \tilde{e} = e - e_0$ as a small parameter. With due regard for expressions (9) and (10), the torsional and longitudinal components can be written in the form of the asymptotic series in terms of the chosen small parameter:

$$\varphi(s,t) = \varepsilon^{1/2}\Phi_1(s,t) + \varepsilon^{3/2}\Phi_2(s,t) + \ldots,$$
$$\hat{x}(s,t) = \varepsilon X_1(s,t) + \varepsilon^2 X_2(s,t) + \ldots$$

With the given expansion taken into account, the equations written in the first-order approximation are analogous to Eqs. (11), (12):

$$\rho\frac{\partial^2\Phi_1}{\partial t^2} = G\frac{\partial^2\Phi_1}{\partial s^2},$$

$$\rho\frac{\partial^2 X_1}{\partial t^2} = E\frac{\partial}{\partial s}\left(\frac{\partial X_1}{\partial s} + \frac{R^2}{2(1+e_0)}\left(\frac{\partial\Phi_1}{\partial s}\right)^2\right).$$

At the same time, in the second-order approximation, the equations take the form

$$\rho\frac{\partial^2\Phi_{21}}{\partial t^2} = G\frac{\partial^2\Phi_2}{\partial s^2},$$

$$\rho\frac{\partial^2 X_2}{\partial t^2} = E\frac{\partial}{\partial s}\left(\frac{\partial X_2}{\partial s} + \frac{R^2}{1+e_0}\frac{\partial\Phi_1}{\partial s}\frac{\partial\Phi_2}{\partial s} + \frac{1}{2(1+e_0)}\left(\frac{\partial X_1}{\partial s}\right)^2 - \frac{R^2}{2(1+e_0)^2}\left(\frac{\partial\Phi_1}{\partial s}\right)^2\frac{\partial X_1}{\partial s} - \frac{R^4}{2(1+e_0)^3}\left(\frac{\partial\Phi_1}{\partial s}\right)^4\right).$$

It is evident that Eq. (11) is the conventional equation of torsional vibrations [3], whereas Eq. (12) for the longitudinal component is inhomogeneous. In this case, the torsional components play the role of an inhomoge-

neity (or of a stimulating force). According to the analysis of both expression (10) for the total strain and nonlinear Eqs. (2), the longitudinal and torsional components that contribute to dynamic loading under tension turn out to be of the same order of magnitude. The solutions to Eq. (12) are superpositions of natural longitudinal waves and vibrations, as well as of stimulated longitudinal waves and vibrations acting at the frequency of torsional ones, resonance phenomena being possible in this case.

In the framework of the theory of plane cross sections, the results presented above can be generalized for the case of the torsional-longitudinal motions of thin strings and rods.

ACKNOWLEDGMENTS

This work was supported by the Russian Foundation for Basic Research, project no. 03-01-00131.

REFERENCES

1. V. A. Svetlitskiĭ, *Mechanics of Rods* (Vysshaya Shkola, Moscow, 1987), Vol. 1/2 [in Russian].
2. Kh. A. Rakhmatulin and Yu. A. Dem'yanov, *Strength under Intense Short-Term Loads* (Fizmatgiz, Moscow, 1961) [in Russian].
3. A. Ya. Sagomonyan, *Stress Waves in Continua* (Mosk. Gos. Univ., Moscow, 1985) [in Russian].

Translated by G. Merzon

Doklady Physics, Vol. 50, No. 9, 2005, pp. 467–472. Translated from Doklady Akademii Nauk, Vol. 404, No. 2, 2005, pp. 192–197.
Original Russian Text Copyright © 2005 by Seyranian, Yabuno, Tsumoto.

MECHANICS

Instability and Periodic Motion of a Physical Pendulum with a Vibrating Suspension Point (Theoretical and Experimental Approach)

A. P. Seyranian*, H. Yabuno, and K. Tsumoto****

Presented by Academician S.S. Grigoryan May 12, 2005

Received May 14, 2005

In nonlinear dynamics, the motion of a pendulum represents a classical paradigm. The vibrations and stability of a pendulum with a vibrating support were studied by many authors (see, e.g., [1–12]). In spite of many publications, there were few experiments devoted to the analysis of the stability and nonlinear behavior of the pendulum. Among the well-known experimental studies, we point to the experiments made by Kapitza [1, 2] in connection with the stabilization of an inverted pendulum by the high-frequency excitation of the support, as well as those made by Chelomeĭ [3] on the stability of an inverted rod with a sliding washer under the vibrating suspension point. Experiments on the stabilization of a pendulum with a vibrating suspension point about a tilted axis were described in [4, 5]. The routes from the lower vertical position to the chaotic motion of the parametrically excited pendulum were investigated experimentally in [6]. We note that those experiments were mostly qualitative.

In this study, the nonlinear behavior of a physical pendulum with a vibrating suspension point is investigated both theoretically and experimentally. Instability conditions for the lower vertical position of the pendulum are found. Periodic motions corresponding to the swinging of the pendulum are obtained for various parameters, and their stability with respect to the parameters is investigated. The frequency–response curve is obtained for periodic motion with small amplitude. Theoretical and experimental results are in good agreement with each other.

BASIC RELATIONS

The plane oscillations of a physical pendulum about the lower vertical position with the periodically varying displacement of the suspension point and viscous damping (see Fig. 1) are governed by the equation

$$I\ddot{\theta} + c\dot{\theta} + mr(g - \ddot{z})\sin\theta = 0. \quad (1)$$

Here, I and m are the moment of inertia and the mass of the pendulum, respectively; θ is the angle measured from the lower vertical position; c is the viscous-friction coefficient; r is the distance between the suspension point and the center of gravity of the pendulum; g is the acceleration of gravity; z is the vertical displacement of the suspension point; and the dot stands for differentiation with respect to time t. It is assumed that the displacement of the suspension point of the pendulum is governed by the law

$$z = a\phi(\Omega t), \quad (2)$$

where a and Ω are the excitation amplitude and frequency, respectively, and $\phi(\tau)$ is an arbitrary smooth

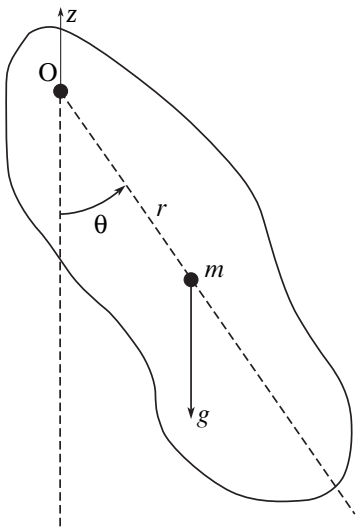

Fig. 1. Physical pendulum.

* *Institute of Mechanics, Moscow State University, Michurinskiĭ pr. 1, Moscow, 119192 Russia*
e-mail: seyran@imec.msu.ru

** *Institute of Engineering Mechanics and Systems, University of Tsukuba, Tsukuba, Japan*

1028-3358/05/5009-0467$26.00 © 2005 Pleiades Publishing, Inc.

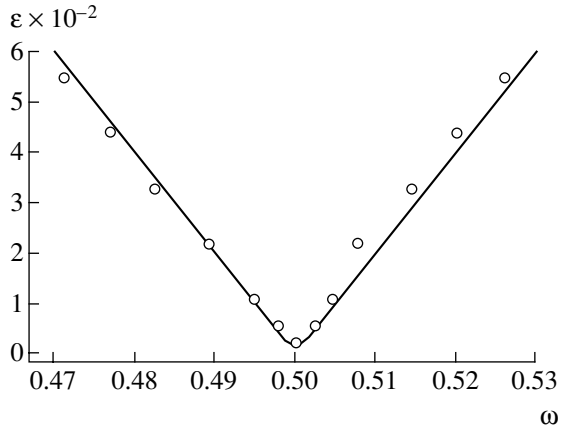

Fig. 2. Instability region of the vertical position of the pendulum ($\theta = 0$).

periodic function with the period 2π. The amplitude a and friction coefficient c are assumed to be small.

For the sake of convenience, we introduce the function $\varphi = -\ddot{\phi}$. Then, we obtain

$$\ddot{z} = -a\Omega^2\varphi(\Omega t). \tag{3}$$

It is assumed that the mean value of the 2π-periodic function $\varphi(\tau)$ is zero:

$$\int_0^{2\pi}\varphi(\tau)d\tau = 0.$$

We now introduce the dimensionless variables and parameters

$$\tau = \Omega t, \quad \varepsilon = \frac{a\Omega_0^2}{g}, \quad \omega = \frac{\Omega_0}{\Omega}, \quad \beta = \frac{c}{I\Omega_0}; \qquad \Omega_0 = \sqrt{\frac{mrg}{I}}. \tag{4}$$

Note that Ω_0 is the eigenfrequency of the pendulum with the immobile suspension point. With this notation, Eq. (1) takes the form

$$\ddot{\theta} + \beta\omega\dot{\theta} + [\omega^2 + \varepsilon\varphi(\tau)]\sin\theta = 0, \tag{5}$$

where the dots stand for differentiation with respect to τ. The coefficients of Eq. (5) depend explicitly on the periodic function $\varphi(\tau)$ and on the three independent parameters ε, β, ω, where ε and β are small.

INSTABILITY REGIONS

According to Lyapunov's theorem, the stability or instability of the trivial solution $\theta = 0$ of nonlinear equation (5) with periodic coefficients is governed by the stability or instability of the linearized equation

$$\ddot{\theta} + \beta\omega\dot{\theta} + [\omega^2 + \varepsilon\varphi(\tau)]\theta = 0. \tag{6}$$

This is Hill's equation with damping. It is known that instability (parametric resonance) occurs near the values $\omega = \frac{k}{2}$, $k = 1, 2, \ldots$. According to [11], the instability regions for Eq. (6) in the three-parameter space are given by half of the cone

$$\frac{\beta^2k^2}{4} + (2\omega - k)^2 < \frac{(a_k^2 + b_k^2)\varepsilon^2}{k^2}, \quad \beta \geq 0, \tag{7}$$

where

$$a_k = \frac{1}{\pi}\int_0^{2\pi}\varphi(\tau)\cos k\tau\, d\tau, \quad b_k = \frac{1}{\pi}\int_0^{2\pi}\varphi(\tau)\sin k\tau\, d\tau, \quad k = 1, 2, \ldots \tag{8}$$

are the Fourier coefficients of the function $\varphi(\tau)$.

Formulas (7) describe the first-order approximations of instability regions and show that the kth resonance region depends only on the kth Fourier coefficients of the periodic function $\varphi(\tau)$.

The cross section of half-cone (7) by the plane $\beta = \text{const} \geq 0$ yields the zones of parametric resonance bounded by hyperbolas (see Fig. 2). The asymptotes of these hyperbolas are found from Eq. (7) with $\beta = 0$. When damping is included ($\beta > 0$), the minimum excitation amplitude of the resonance according to (7) is equal to

$$\varepsilon_{\min} = \frac{\beta k^2}{2\sqrt{a_k^2 + b_k^2}}. \tag{9}$$

With an increase in the resonance number k, the Fourier coefficients a_k and b_k tend to zero. This implies that, for a fixed damping coefficient β, the minimum excitation amplitude tends to infinity with increasing k. This explains why it is easier to observe the parametric resonance at small numbers $k = 1, 2, \ldots$, because, at higher resonance numbers, essential efforts and high excitation amplitudes are needed to set the system into unstable motion.

For the function $\varphi(\tau) = \cos\tau$, we have $a_1 = 1$, $b_1 = 0$. Thus, the first resonance region $\left(\omega \approx \frac{1}{2}\right)$ for this periodic function is given by the inequality

$$\frac{\beta^2}{4} + (2\omega - 1)^2 < \varepsilon^2, \quad \beta \geq 0. \tag{10}$$

In dimensional quantities, we obtain from Eqs. (4) that the swinging of the pendulum occurs near excitation frequencies close to the critical values

$$\Omega_k = \frac{2\Omega_0}{k}, \quad k = 1, 2, \ldots. \tag{11}$$

In dimensional quantities, inequalities (4), (7) yield the

instability regions as

$$\frac{c^2}{4I^2\Omega_0^2} + \left(\frac{\Omega}{\Omega_k} - 1\right)^2 < \frac{(a_k^2 + b_k^2)a^2\Omega_0^4}{k^4 g^2}, \quad (12)$$
$$\beta \geq 0, \quad k = 1, 2, \ldots.$$

When the problem parameters satisfy inequalities (12), the lower vertical equilibrium position of the pendulum $\theta = 0$ becomes unstable, and the pendulum begins to swing. Then, both regular and chaotic motions are possible.

The solid line in Fig. 2 shows the boundary of the first resonance region $\left(\omega \approx \frac{1}{2}\right)$ for the function $\varphi(\tau) = \cos\tau$ and damping coefficients $\beta = 2.61 \times 10^{-3}$, given by formula (10), and experimental points are shown by circles.

PERIODIC SOLUTIONS

Assuming that the angle θ is small, we replace $\sin\theta$ in (5) by the first two terms of the Taylor expansion, $\sin\theta \approx \theta - \frac{\theta^3}{6}$. Neglecting higher-order terms, we arrive at the equation with small nonlinearity:

$$\ddot{\theta} + \beta\omega\dot{\theta} + [\omega^2 + \varepsilon\varphi(\tau)]\theta - \frac{\omega^2\theta^3}{6} = 0. \quad (13)$$

Here, it is assumed that ε and β are small quantities on the order of $o(1)$ [12].

We can estimate the amplitude of oscillations at which Eq. (13) is valid. The absolute value of the nonlinear term $\frac{\omega^2\theta^3}{6}$ in Eq. (13) is necessarily much less than the absolute value of the linear term $\omega^2\theta$. Thus, we have the condition $\frac{\theta^2}{6} \sim O(\varepsilon)$. For example, $|\theta| < \frac{\pi}{4}$ for $\varepsilon \approx 0.1$. This is a rough estimate of the validity of Eq. (13). Equation (13) with $\varphi(\tau) = \cos\tau$ is sometimes called the nonlinear Mathieu–Hill equation [8, 12].

Let us study the behavior of nonlinear system described by Eq. (13) and parametrically excited by the periodic function $\varphi(\tau) = \cos\tau$ near the first resonance frequency $\omega \approx \frac{1}{2}$ ($\Omega \approx 2\Omega_0$). Using the method of averaging [7, 8], we seek an approximate solution of the system in the form $\theta(\tau) = \Theta\cos\left(\frac{\tau}{2} + \psi\right)$, where the amplitude Θ and phase ψ are slow variables. As a result,

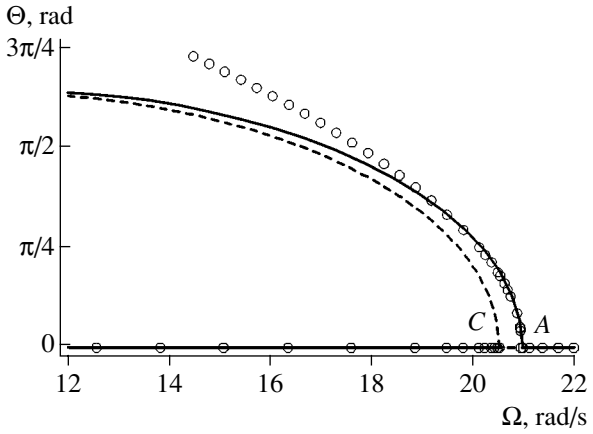

Fig. 3. Frequency–response curve for $\varepsilon = 1.098 \times 10^{-2}$ and $\beta = 2.61 \times 10^{-3}$.

for these variables, we arrive at the set of differential equations

$$\frac{d\Theta}{d\tau} = -\frac{\Theta\beta\omega}{2} + \frac{\Theta\varepsilon}{2}\sin 2\psi,$$
$$\frac{d\psi}{d\tau} = \omega - \frac{1}{2} - \frac{\Theta^2\omega^2}{8} + \frac{\varepsilon}{2}\cos 2\psi. \quad (14)$$

For steady motion, we have

$$\frac{d\Theta}{d\tau} = 0, \quad \frac{d\psi}{d\tau} = 0. \quad (15)$$

From Eqs. (14) and (15), in addition to the trivial solution $\Theta = 0$, we find the nontrivial amplitude

$$\Theta^2 = \frac{4}{\omega^2}(2\omega - 1 \mp \sqrt{\varepsilon^2 - \beta^2\omega^2}) \quad (16)$$

and the phase

$$\psi = \frac{1}{2}\arctan\left(\mp\frac{\beta\omega}{\sqrt{\varepsilon^2 - \beta^2\omega^2}}\right) + \pi j, \quad j = 0, 1, \ldots. \quad (17)$$

We insert the denominator of expression (16) inside the parentheses and express the amplitude as a function of the ratio $\frac{1}{\omega} = \frac{\Omega}{\Omega_0}$:

$$\Theta^2 = 4\left(\frac{2\Omega}{\Omega_0} - \frac{\Omega^2}{\Omega_0^2} \mp \sqrt{\frac{\varepsilon^2\Omega^4}{\Omega_0^4} - \frac{\beta^2\Omega^2}{\Omega_0^2}}\right). \quad (18)$$

The frequency–response curve for the fixed damping parameter $\beta = 2.61 \times 10^{-3}$ and amplitude $\varepsilon = 1.098 \times 10^{-2}$ ($a = 1$ mm) is presented in Fig. 3. The minus and

plus signs in formula (18) correspond to the lower (dashed line) and upper (solid line) branches of the curve, respectively, and experimental points are given by circles.

To find the width of the resonance zone *AC* (see Fig. 3), it is necessary to equate the right-hand side of expression (18) to zero. Then, we find that the width *AC* in the first approximation is determined by inequality (10) in terms of the variable $\frac{\Omega}{\Omega_0}$. This is not surprising, because *AC* specifies the instability zone of the trivial solution $\theta = 0$.

The lower and higher branches of the frequency–response curve given by Eq. (18) meet at the point *B* with the vertical tangent at the frequency

$$\frac{\Omega}{\Omega_0} = \frac{\beta}{\varepsilon}. \tag{19}$$

With increasing damping, the frequency–response curve becomes narrower and shorter, and as $\frac{\beta}{\varepsilon} \longrightarrow 2$, the curve disappears tending to the point $\frac{\Omega}{\Omega_0} = 2, \Theta = 0$. We note that the point *B* (with the vertical tangent) according to (18) obeys the parabolic law.

Thus, according to Eqs. (10) and (19), periodic solutions (16)–(18) exist within the frequency interval

$$\frac{\beta}{\varepsilon} \le \frac{\Omega}{\Omega_0} \le 2 + \sqrt{4\varepsilon^2 - \beta^2}. \tag{20}$$

It should be noted that the method of multiple scales [12] yields another form of the frequency–response curve

$$\Theta^2 = 8\left(2 - \frac{\Omega}{\Omega_0} \mp \sqrt{\frac{\varepsilon^2\Omega^4}{4\Omega_0^4} - \beta^2}\right). \tag{21}$$

However, near the resonant frequency $\Omega \approx 2\Omega_0$, formulas (18) and (21) yield similar results.

STABILITY OF PERIODIC SOLUTIONS

In this section, we analyze the stability of periodic solutions $\theta_0(\tau) = \cos\Theta\left(\frac{\tau}{2} + \psi\right)$, the amplitude and phase of which are given by relations (16)–(18). We take a small increment to the periodic solution $\theta(\tau) = \theta_0(\tau) + u(\tau)$ and substitute this function into Eq. (13) with the periodic function $\varphi(\tau) = \cos\tau$. Then, in the first approximation, we obtain a linear equation in terms of $u(\tau)$:

$$\ddot{u} + \beta\omega\dot{u} + \left(\omega^2 + \varepsilon\cos\tau - \frac{\omega^2\theta_0^2(\tau)}{2}\right)u = 0. \tag{22}$$

According to Lyapunov's stability theorem based on the linear approximation, the stability and instability of periodic solutions is determined by the stability and instability of the solutions of the corresponding linearized equation for the increment function $u(\tau)$, i.e., of Eq. (22). This is Hill's equation with damping [11], the coefficients of which depend on the three independent parameters ω, ε, β with $\omega \approx \frac{1}{2}$, $\varepsilon, \beta \ll 1$ and on the 2π-periodic function

$$\Phi(\tau) = (1 - \omega^2)\cos\tau - \frac{\Theta^2\omega^2}{2\varepsilon}\cos^2\left(\frac{\tau}{2} + \psi\right). \tag{23}$$

The instability region for Eq. (22) near the values $\omega = \frac{1}{2}$, $\varepsilon = \beta = 0$ is given by [11]

$$\frac{\beta^2}{4} + (2\omega - 1 + a_0\varepsilon)^2 < \varepsilon^2(a_1^2 + b_1^2), \tag{24}$$

where a_0, a_1, and b_1 are first Fourier coefficients of the function $\Phi(\tau)$. The asymptotic stability region is correspondingly given by inequality (24) with the opposite sign.

For Fourier coefficients, we find

$$a_0 = -\frac{\Theta^2\omega^2}{2\varepsilon}, \quad a_1 = 1 - \omega^2 - \frac{\Theta^2\omega^2\cos 2\psi}{4\varepsilon}, \quad b_1 = \frac{\Theta^2\omega^2\sin 2\psi}{4\varepsilon}. \tag{25}$$

Since $\omega \approx \frac{1}{2}$, the first term in inequality (24) can be replaced by $\omega^2\beta^2$. Thus, near the values $\varepsilon = \beta = 0$, $\omega = \frac{1}{2}$, the following inequality is valid:

$$\omega^2\beta^2 + (2\omega - 1 + a_0\varepsilon)^2 - \varepsilon^2(a_1^2 + b_1^2) < 0. \tag{26}$$

Substituting coefficients (25) into (26), expressing $\cos 2\psi$ from Eqs. (14) and (15), and using relations (16), we obtain

$$\Theta^2\omega^2\left(\frac{\Theta^2\omega^2}{4} - 2\omega + 1\right) = \mp\Theta^2\omega^2\sqrt{\varepsilon^2 - \beta^2\omega^2} < 0. \tag{27}$$

From the last inequality, it follows that the periodic solution (16)–(18) with the plus and minus signs is, respectively, stable and unstable. These solutions are shown in Fig. 3 by the solid and dashed lines, respectively. The experimental points in Fig. 3 correspond to stable periodic solutions, while unstable solutions are not observed in the experiment. It is seen in Fig. 3 that

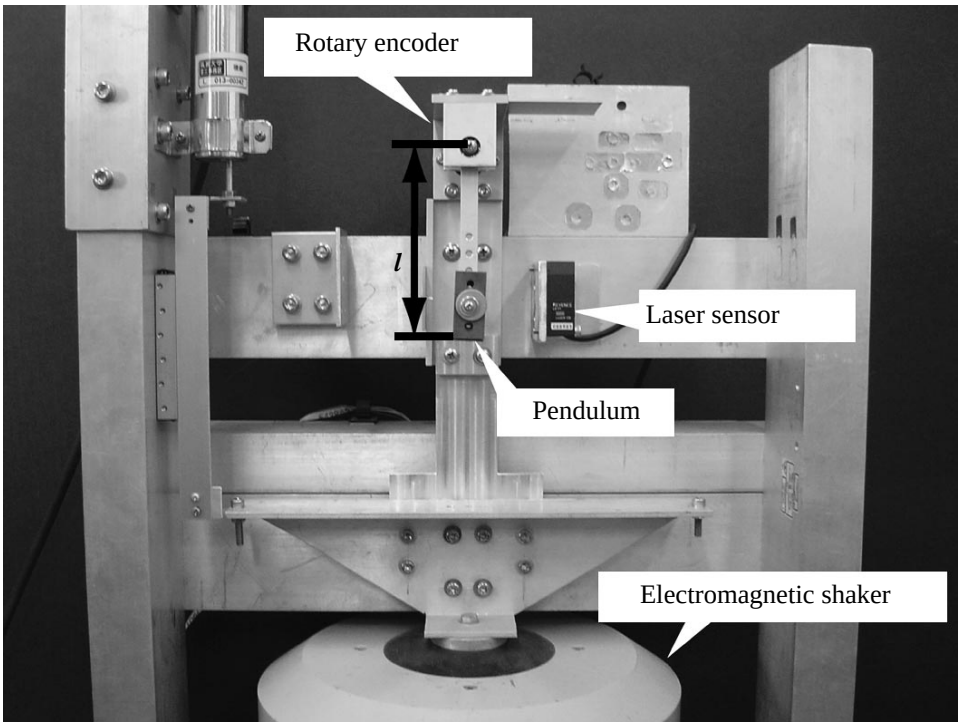

Fig. 4. Experimental setup.

the results of the experiment are in good agreement with theoretical results up to the periodic-motion amplitude $\Theta \approx \frac{\pi}{4}$. Note that, for higher amplitudes, Eq. (13) and formulas (16)–(18) are not valid.

Thus, it follows from Fig. 3 and the above consideration that, when the suspension point is excited at a frequency $\Omega \approx 2\Omega_0$, the pendulum oscillates according to the harmonic law $\theta_0(t) = \Theta\cos\left(\frac{\Omega t}{2} + \psi\right)$, and the frequency $\frac{\Omega}{2}$ can be higher or lower than the eigenfrequency Ω_0 of the pendulum with the immobile suspension point. This conclusion contradicts the important conclusion made by Kapitza [1, 2] according to which vibrations of the support always reduce the period of the pendulum. This erroneous conclusion was caused by an oversimplification of the analysis.

DESCRIPTION OF THE EXPERIMENT

As shown in Fig. 4, the experimental setup consists of a pendulum with the length $l = 108$ mm whose pivot (radial bearing) is vertically excited by an electromagnetic shaker. The deflection angle of the pendulum is measured with a rotary encoder, and the vertical motion of the pivot is measured with an LB-60 laser sensor (KEYENCE Corp.) with the spatial resolution of 40 μm. To study unstable regions and frequency–response curves, we monitored the angular deflections and frequency components of the excitation of the pendulum by a DS-2100 Multichannel Data Station (ONO SOKKI Corp.). The frequency resolution for the excitation and response of the pendulum was 0.02 Hz, and the experimental angular resolution for the pendulum was 1.57×10^{-3} rad. The eigenfrequency of the pendulum was equal to $\Omega_0 = 10.374$ rad/s, and the range of the pivot excitation amplitude was $a = 0.5$–5 mm. The damping coefficient calculated from the decay of free oscillations of the pendulum with the immobile suspension point was equal to $\beta = 2.61 \times 10^{-3}$.

For a fixed damping coefficient and excitation amplitude, the instability range of the vertical position of the pendulum in Fig. 2 is equal to the interval *AC* of the frequency–response curve. The experimental points on the upper part of the frequency–response curve in Fig. 3 were obtained by the excitation of the pivot of the pendulum with the given amplitude at the near-critical frequency $\Omega \approx 2\Omega_0$, with the subsequent small-step increase in frequency until point *A* with the zero amplitude is reached. Thus, the points of the left boundary of the instability region in Fig. 2 were obtained for different excitation amplitudes. The experimental points on the frequency axis in Fig. 3 correspond to the stability of the vertical position of the pendulum $\theta = 0$. The right boundary of the instability region in Fig. 2 was obtained by the excitation of the pendulum from the equilibrium position $\theta = 0$ at different amplitudes and frequencies with Coulomb friction preventing paramet-

ric resonance. For this reason, the left and right boundaries of the instability region in Fig. 2, obtained experimentally by different methods, differ in the degree of their agreement with the theoretical curves. Nevertheless, Figs. 2 and 3 demonstrate rather good consistency of theoretical and experimental results.

ACKNOWLEDGMENTS

We are grateful to A.A. Maĭlybaev for fruitful discussions. This work was supported by the Japanese Society for the Promotion of Science (JSPS) and the Russian Foundation for Basic Research, project no. 03-01-00161.

REFERENCES

1. P. L. Kapitza, Zh. Éksp. Teor. Fiz. **21**, 588 (1951).
2. P. L. Kapitza, Usp. Fiz. Nauk **24**, 7 (1951).
3. V. N. Chelomeĭ, Dokl. Akad. Nauk SSSR **270** (1), 62 (1983) [Sov. Phys. Dokl. **28** (5), 387 (1983)].
4. T. G. Strizhak, *Asymptotic Method of Normalization* (Vishcha Shkola, Kiev, 1984) [in Russian].
5. H. Yabuno, M. Miura, and N. Aoshima, J. Sound Vib. **273**, 493 (2004).
6. R. W. Leven, B. Pompe, C. Wilke, and B. P. Koch, Physica D (Amsterdam) **16**, 371 (1985).
7. N. N. Bogolyubov and Yu. A. Mitropol'skiĭ, *Asymptotic Methods in the Theory of Nonlinear Oscillations* (Nauka, Moscow, 1974; Gordon and Breach, New York, 1962).
8. A. H. Nayfeh and D. T. Mook, *Nonlinear Oscillations* (Wiley, New York, 1979).
9. V. I. Arnold, *Mathematical Methods of Classical Mechanics*, 2nd ed. (Nauka, Moscow, 1978; Springer-Verlag, New York, 1989).
10. I. I. Blekhman, *Vibration Mechanics: Nonlinear Dynamic Effects, General Approach, Applications* (Fizmatlit, Moscow, 1994; World Sci., Singapore, 1998).
11. A. P. Seyranian, Dokl. Akad. Nauk **376** (1), 44 (2001) [Dokl. Phys. **46**, 41 (2001)].
12. J. J. Thomsen, *Vibrations and Stability. Advanced Theory, Analysis and Tools* (Springer, Berlin, 2003).

Translated by A. Seyranian

Doklady Physics, Vol. 50, No. 9, 2005, pp. 473–477. Translated from Doklady Akademii Nauk, Vol. 404, No. 3, 2005, pp. 339–343.
Original Russian Text Copyright © 2005 by Zubin, Ostapenko, Chulkov.

MECHANICS

One Feature of Conical Gas Flows with Shock Waves and Boundary-Layer Separation

M. A. Zubin, N. A. Ostapenko, and A. A. Chulkov

Presented by Academician G.G. Chernyĭ March 17, 2005

Received March 22, 2005

In this paper, some numerical and experimental results are presented for supersonic conical gas flows over V-shaped wings with a bow shock wave attached to the leading edges. These results are related to one of the features of the flow in the inner elliptic region of the disturbed flow, which is bounded by an extensive system of shock waves. According to calculations for an inviscid flow over a wing and experiments with corresponding parameters, different structures of the flow are observed for cases in which the developed separation of the boundary layer is induced by a shock wave in the actual flow. This separation leads to the appearance of an additional surface of an intense contact discontinuity, which is attributed to the λ configuration of shock waves. In other words, the results indicate that the inviscid-origin features of the flow structure that are manifested in experiments can be attributed to new boundary conditions that arise for the inner inviscid problem due to the developed separation of the boundary layer.

The existence of this feature of conical flows is demonstrated for an airflow with the Mach number M = 3 over a V-shaped wing. The wing has the opening angle $\gamma = \frac{2\pi}{3}$ and the angle $\beta = \frac{\pi}{2}$ at the vertex of the wing struts. Regular interaction between plane shock waves propagating from the leading edges is realized near the wing with such geometric parameters for small angles of attack α and angles of sideslip ϑ. In this paper, we present examples of flow regimes in the canonical variables $\eta = \frac{y}{x}$ and $\zeta = \frac{z}{x}$ (the *x* axis coincides with the central chord and *z* = 0 is the wing symmetry plane), where the shock wave structure is far from that of linearly perturbed regular interaction [1].

The region of angles α and ϑ between the axis ϑ = 0 and curve *1* (Fig. 1) corresponds to the flow regimes with asymmetric or Mach interaction of shock waves attached to the leading edges of the wing. Curve *1* is determined by numerical calculations according to the condition $\frac{\partial p}{\partial \zeta} = 0$ for pressure applied from the inner side of the Mach cone of the uniform flow on the surface of the windward strut. In this curve, the flow with a shock wave on the surface of the windward strut transforms to a shock-free flow. In these cases, the corresponding inner shock wave of the Mach configuration on the windward-strut surface has zero intensity. Curve *2* corresponds to the condition $\tan\alpha = \sin\vartheta \cot\frac{\gamma}{2}$ under which the leeward strut does not introduce perturbations to the incident flow. To the right of this curve, flow regimes with a centered rarefaction wave at the leading edge of the leeward strut occur. Curve *3* is determined from the condition that the Mach cone of the uniform flow over the leeward strut passes through the intersection line of the plane shock waves attached

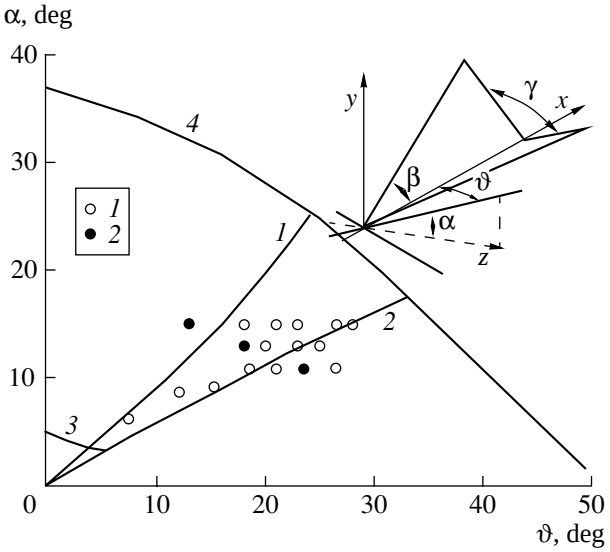

Fig. 1. Variation regions of the angle of attack α and of the angle of sideslip ϑ for various regimes of an asymmetric flow over a V-shaped wing (curves *1–4*); γ is the opening angle; β is the angle at the vertices of the wing struts; and open and closed circles (*1*, *2*) correspond to experimental parameters.

Institute of Mechanics, Moscow State University, Michurinskiĭ pr. 1, Moscow, 119992 Russia

1028-3358/05/5009-0473$26.00 © 2005 Pleiades Publishing, Inc.

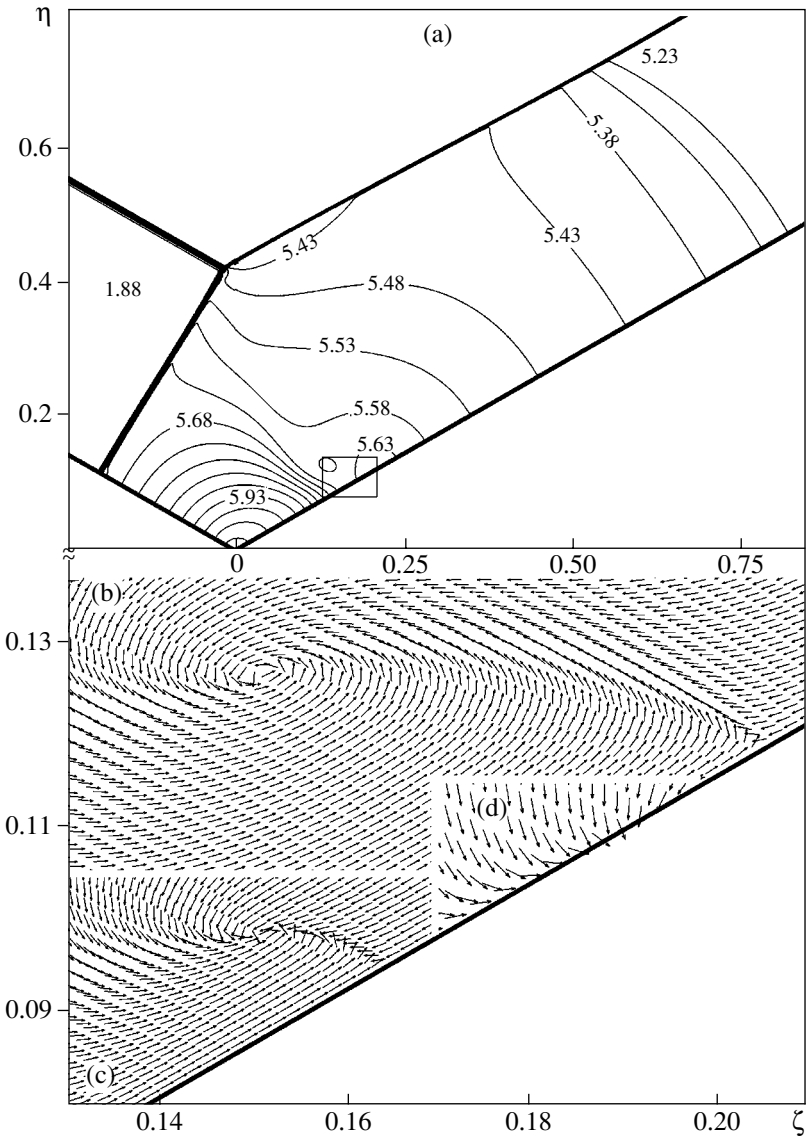

Fig. 2. (a) Isobars and (b–d) fragments of the transverse velocity-direction fields for various regimes of gas flow around a wing.

to the leading edges. Therefore, flow regimes with the Mach configuration of shock waves are inevitably realized above curves *2* and *3*. The selection rule for a certain regime exists only for the symmetric flow around the wing [2]. Curve *4* corresponds to the separation of the shock wave from the leading edge of the windward strut.

For a qualitatively new type of conical flow, which is realized in an asymmetric stream of ideal gas around the wing ($\alpha = 20^\circ$ and $\vartheta = 18^\circ$), Fig. 2a shows the isobars in the region bounded by the unperturbed flow (from above) and uniform flows behind plane shock waves attached to the leading edges. Figure 2b shows the fragment of the transverse-velocity direction field (on a sphere) projected on the $x = 1$ plane (a rectangle in Fig. 2a). According to the direction field, the classical Ferry singularity (a node of conical streamlines) [3] that coincides with the position of the drain line on the windward strut is absent. Streamlines coming from the two leading edges to the drain point pass upward from the wall and, together with other streamlines, are rolled into a spiral with a low absolute value of the transverse velocity as compared to its value in peripheral regions.

Thus, Ferry singularities that can be called vortex singularities exist in an asymmetric flow around V-shaped wings. In these cases, streamlines other than those beginning at the leading edges of leeward and windward struts do not enter the drain point on the wall. The vortex Ferry singularity is formed inside the shock layer at the vertex of the contact discontinuity passing upward from the drain point on the wall.

According to calculations for both asymmetric Mach interaction (Fig. 2a) and flow regimes with a shock-free flow on the windward strut surface (between

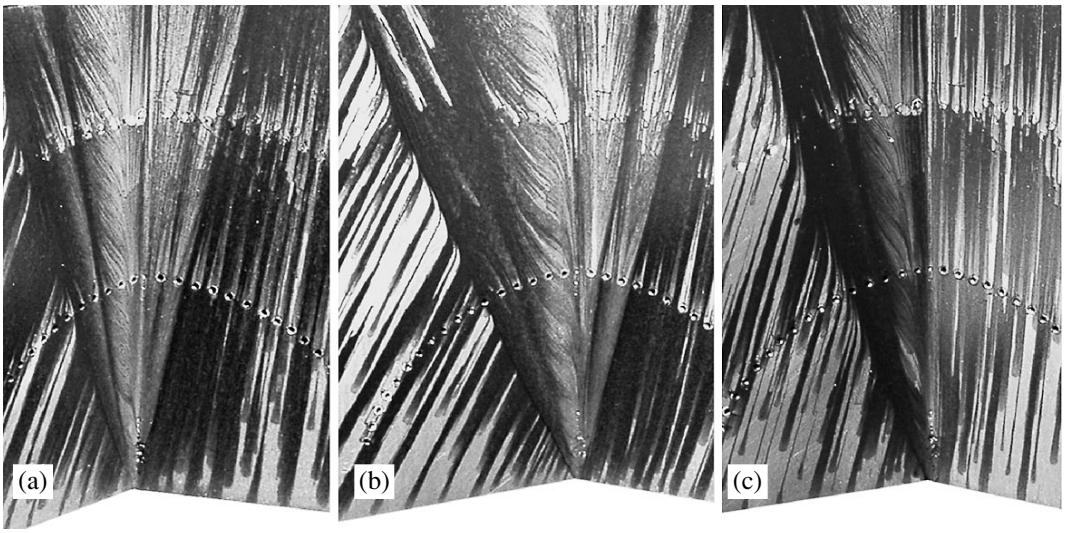

Fig. 3. Patterns of limiting streamlines near the central chord, which are obtained in experiments with various regimes of flow around a wing.

lines *1* and *2* in Fig. 1), a vortex Ferry singularity is formed above the windward strut. In this case, the height of a "leg" (contact discontinuity) at whose vertex the vortex Ferry singularity is formed depends on the distance from the regime image point to line *2* [see fragments of velocity-direction fields in Fig. 2 for α = 15° and ϑ = (c) 18° and (d) 26.5°]. For the regime corresponding to almost zero intensity of the compression shock at the leading edge of the leeward strut (Fig. 2d), the standard structure of the flow with the Ferry singularity on the wall of the leeward strut is observed.

According to analysis of the total-pressure recovery factor $K(\vartheta) = S^k$ (S is the entropy and $k = \frac{1}{1-\gamma}$, where γ is the specific-heat ratio), the jump ΔK at the contact discontinuity, e.g., for α = 20° ($0.17 < \Delta K < 0.25$ and $\vartheta < 25°$) and 15° ($0.1 < \Delta K < 0.16$ and $\vartheta < 20°$) is large on both sides of the contact discontinuity beginning at the branch point of the bow shock wave over the leeward strut. This contact discontinuity enters the Ferry point along with the contact discontinuity coming from the branch point over the windward strut if the latter point exists. The values of K on both sides of the contact discontinuity approach each other when the regime image point approaches curve *2* (Fig. 1). In contrast to the above data on ΔK for α = 20° and 15°, losses of the total pressure in shock waves are relatively low for, e.g., α = 8°, and the jump of $K(\vartheta)$ at the contact discontinuity is small ($\Delta K < 0.05$). In this case, a standard Ferry singularity is observed on the windward strut surface.

Analysis shows that the existence of the vortex Ferry singularity in an asymmetric flow of an ideal gas around the V-shaped wing depends on the distribution of the parameters at the boundary of the elliptic region determined in the conical flow by the system of shock waves, which bounds this region and can be accompanied by intense contact discontinuities.

The prediction of new structures that are formed in conical flows by the stream surfaces should be tested experimentally. These qualitatively new types of flow exist at intensities of internal shock waves over the leeward strut, which exceed the critical value p_k = 1.6 corresponding to the initiation of separating the turbulent boundary layer [4]. Points *1* and *2* in Fig. 1 are the image points for the regimes of flow around wings, which are realized in the experiments in the A3 wind tunnel at the Institute of Mechanics, Moscow State University. The values of Mach number M = 2.96 and of the Reynolds number $\mathrm{Re} = 6 \times 10^6$ were calculated on the basis of the model length. We note that the intensity of the compression shock incident onto the leeward strut for α = const increases with ϑ. Analysis shows that the critical value of the intensity for, e.g., α = 8° and 10° is attained at $\vartheta \approx 9°$ and 7.5°, respectively.

Figure 3 shows patterns of the limiting streamlines near the central chord of the wing, which are obtained by the oil–soot visualization [α = 15° and ϑ = (a) 18° and (b) 26.5°]. According to these data and pressure distribution on the wall, the separation of the turbulent boundary layer occurs on the leeward strut. In addition to the separation lines of the boundary layer and attachment (spreading) of the flow, the internal separation of the boundary layer is observed [4, 5]. New features in the flow are observed on the windward strut, and they become more pronounced as the angle of sideslip increases (Figs. 3a and 3b). These features are represented by two regions that are lighter than the general background and where the flow is conical. Each of these regions contains the spreading line and is separated by drain lines (dark bands formed by oil coating carried from two sides) from the neighboring regions of

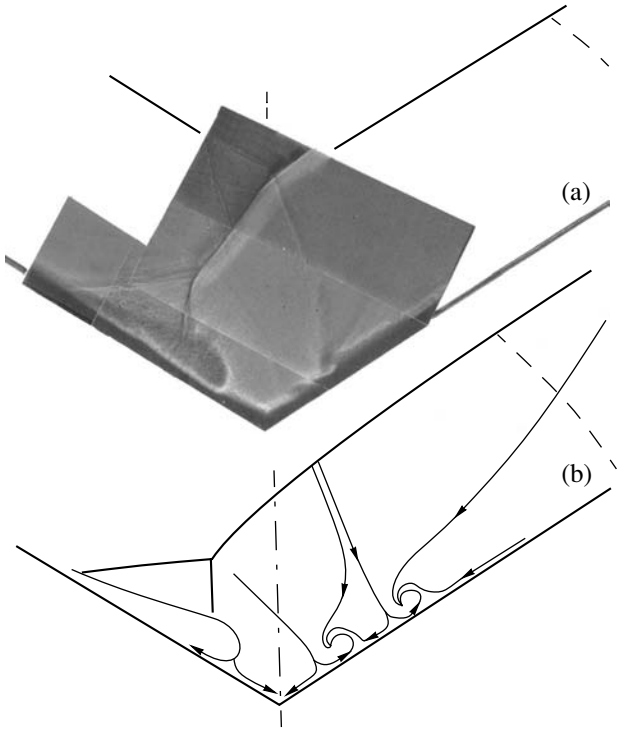

Fig. 4. (a) Shadow pattern of the flow in a plane perpendicular to the central chord of the wing and (b) flow diagram.

the flow and from the flow beginning at the leading edge of the windward strut. The central chord of the wing is also a drain line. Such structures introduce fundamental changes to the elliptic region of the conical flow, which are accompanied by increased thermal fluxes on the wall. It is important to reveal the reasons of the origin of such structures, because the ideal-gas model realization of various Ferry singularities on the surface of the windward strut, where only the drain line exists (Figs. 2b–2d), does not exhibit experimentally observed structures.

The results obtained using special laser technology for studying supersonic conical flows [6] indicate the cause of the existence of two conical domains of the flow with the spreading lines of the flow on the windward strut. Figure 4a shows the shadow pattern of the flow in a plane perpendicular to the central chord of the wing. The pattern consists of several fragments obtained in various experiments at $\alpha = 15°$ and $\vartheta = 18°$. The separation of the boundary layer on the leeward strut that is accompanied by the developed λ configuration of shock waves is observed in the pattern, where two intense contact discontinuities are also seen. One of these discontinuities begins at the triple point of the λ configuration of shock waves, and the other, at the branch point of the compression shock over the leeward strut. According to the calculations, the latter discontinuity is observed when $K(\vartheta)$ undergoes a noticeable jump on the contact discontinuity. Both contact discontinuities (or streamlines close to them) arrive at different points on the windward strut surface. Regions that can be identified as conical vortex ones are observed to the right of their attachment points. The contact discontinuity coming from the branch point of the bow shock wave over the windward strut is seen on the pattern. It approaches the contact discontinuity originating from the branch point over the leeward strut and is immersed in the region of the vortex rotating counterclockwise. The vortex that arises to the right of the attachment point of the contact discontinuity belonging to the λ configuration of shock waves rotates in the same direction. Ferry singularities exist inside these vortices.

We note that, for $\alpha = 15°$ and $\vartheta = 26.5°$ (Fig. 3b), when the contact discontinuity originating from the branch point of the bow shock wave over the leeward strut is of low intensity and is not observed in experiment, the conical vortex region that is associated with the attachment of the contact discontinuity for smaller angles of sideslip and is attributed to the indicated branch point (Fig. 4a) continues to exist. It is also realized for regimes whose image points lie to the right of curve *3* (Fig. 1), when the leading edge of the leeward strut becomes a generator of the centered rarefaction wave and only the triple point of the λ configuration of shock waves exists. Therefore, the existence of a conical vortex structure that is farther from the central chord and consists of two vortices observed in experiment (Figs. 3b and 4a) is not generally associated with the attachment of the contact discontinuity (or neighboring streamlines) generated by the branch point of the bow shock wave over the leeward strut. The assumed flow diagram realized in such cases is shown in Fig. 4b.

The features experimentally observed in the shock layer of the flow imply the following hypothesis. Structures differing from those predicted within the framework of ideal-gas theory are realized in an actual flow due to special boundary conditions for the inner elliptic region of the conical inviscid-gas flow. These boundary conditions are characterized by the existence of the surface of the intense contact discontinuity generated due to the separation of the boundary layer on the leeward strut. To verify this hypothesis, we carried out experiments using various methods for $\alpha < 15°$ (Fig. 1). The investigation shows that, if the intensity p_w of the shock wave incident on the leeward strut is insufficient for the formation of the developed separation of the turbulent boundary layer, when $p_w > 2.5$ [5], the contact discontinuities generated by the branch point in the wave structure (realized when the boundary layer becomes thicker and the boundary layer is separated) are not observed on shadow patterns due to low intensity and give rise to the formation of no special structures on the windward strut. We note that, for the indicated value of p_w, which changes slightly with the Mach number of the preceding uniform flow, the contact discontinuity intensity depending on $\Delta K > 0.06$ becomes more noticeable.

As an example, Fig. 3c shows the pattern of limiting streamlines on the wing surface for $\alpha = 9.2°$, $\vartheta = 15.2°$

($p_w \approx 2.25$). In this case, the central chord is the stagnation line for the transverse flow rather than the drain line as, e.g., in Figs. 3a and 3b. The drain line composing angle $\varphi \approx 3.5°$ with the central chord is revealed in both simulation and experiment. This property indicates that the intensity of the contact discontinuity generated by the λ configuration of shock waves in the undeveloped separation of the boundary layer is insufficient for generating the boundary conditions responsible for the existence of two conical vortex structures on the windward strut.

Analysis of the function $K(\vartheta)$ that is calculated for $\alpha = 15°$ on both sides of the contact discontinuity that originates from the triple point of the λ configuration of shock waves in terms of the coordinates of the branch point on the shadow patterns (Fig. 4a) and the plateau pressure in the separation region shows that the jump ΔK increasing with the angle of sideslip is very small (~0.02) at $\vartheta = 13°$. This property agrees with the oil–soot visualization of the flow. Comparison of the patterns for the limiting streamlines at $\alpha = 15°$ and at various ϑ values shows that the existence of two conical regions on the windward strut with the flow spreading lines becomes less pronounced at $\vartheta = 13°$. The approximate boundary of the transition from flow regimes with the drain line on the windward strut to regimes with the two indicated regions is shown by closed circles in Fig. 1.

On the whole, experimental results corroborate the hypothesis of the origin of particular vortex structures on the windward strut that are not revealed in ideal-gas calculations. However, since the concept of the developed separation of the turbulent boundary layer has no formal description, the determination of the region of parameters in which these structures are realized presents a particular problem for each case.

ACKNOWLEDGMENTS

This work was supported by the Russian Foundation for Basic Research, project no. 03-01-00041, and by the Council of the President of the Russian Federation for the Support of Young Russian Scientists and Leading Scientific Schools, project no. NSh-2001.2003.1.

REFERENCES

1. N. A. Ostapenko and A. M. Simonenko, Izv. Akad. Nauk, Mekh. Zhidk. Gaza, No. 1, 97 (2004).
2. N. A. Ostapenko, Trudy Mat. Inst. Ross. Akad. Nauk **223**, 238 (1998).
3. A. Ferry, NASA Tech. Memo., No. 1045 (1951).
4. M. A. Zubin and N. A. Ostapenko, Izv. Akad. Nauk SSSR, Mekh. Zhidk. Gaza, No. 6, 43 (1983).
5. M. A. Zubin and N. A. Ostapenko, Izv. Akad. Nauk SSSR, Mekh. Zhidk. Gaza, No. 3, 51 (1979).
6. A. L. Gonor, M. A. Zubin, and N. A. Ostapenko, *Application of Lasers in Optical Methods of Experimental Aerodynamics* (Mosk. Gos. Univ., Moscow, 1982) [in Russian].

Translated by R. Tyapaev

Doklady Physics, Vol. 50, No. 9, 2005, pp. 478–482. Translated from Doklady Akademii Nauk, Vol. 404, No. 3, 2005, pp. 344–347.
Original Russian Text Copyright © 2005 by Monakhov.

MECHANICS

Contact Problems of Filtration Theory in Curvilinear Domains

Academician V. N. Monakhov

Received May 3, 2005

An explicit representation is provided for solutions of gravity-filtration problems for a liquid through porous media, when a given part of the boundary of a filtration domain is curvilinear. Similar to problems with polygonal boundaries, the construction of their solutions is reduced to the determination of numerical parameters that are analogous to constants in the Schwarz–Christoffel formula for the conformal mapping of polygons. The solvability of a nonlinear set of equations with respect to parameters is determined using the method proposed by the author in 1967 on the basis of *a priori* estimates of the solutions to this set.

1. CONFORMAL MAPPING REPRESENTATION

Two-dimensional stationary problems of the filtration of an incompressible liquid through homogeneous isotropic media are described by the complex potential of a flow $w = w(z) = \varphi + i\psi$, which is an analytical function, where ψ is the stream function and $\varphi = p(\rho g)^{-1} + x$ is the hydrostatic pressure. The derivative of the complex potential is related to the filtration rate $\mathbf{v} = (u, v)$ as $\frac{dw}{dz} = u - iv$ [1, 2]. The Ox axis is assumed to be opposite to the gravitational acceleration $\mathbf{g} = (-g, 0)$.

The method proposed in this study is applicable to numerous problems of the theory of gravity filtration for a liquid in porous media [3–8]. For definiteness, we consider the general problem of the filtration of a liquid in a finite aquifer (embankment dam) with a free boundary. The boundary ∂D of the filtration domain D consists of an unknown free surface L ($\psi = Q = \text{const}$, $\varphi + x = \text{const}$) and a given curve $\Gamma = \Gamma^0 \cup \Gamma^1 \cup \Gamma^2$ including an aquifuge Γ^1 ($\psi = \text{const}$) and boundaries with the immobile liquid Γ^k ($\varphi = \varphi_k = \text{const}$, $k = 0$ and 2).

Boundary conditions for the desired analytic function $w(z) = \varphi + i\psi$ are specified as the image of the boundary $\partial D = L \cup \Gamma$ of the filtration domain D. This image is a rectangle $\partial D^* = w(\partial D)$ whose height $Q > 0$ (fluid-flow rate) is unknown.

We first consider the curve Γ as a polygon P with vertices z_k and the corresponding angles $\alpha_k\pi$, where $k = 0, 1, \ldots, n+1$, and side lengths $l_k = |z_k - z_{k-1}|$, where $k = 1, 2, \ldots, n+1$.

Let us carry out the conformal mappings z: $E \longrightarrow D$ and w: $E \longrightarrow D^*$ of the upper half-plane E: $\operatorname{Im}\zeta > 0$ onto the domains $D(P)$, $\partial D = P \cup L$ and D^*, respectively, and let t_k, where $k = 0, 1, \ldots, n+1$ ($t_0 = -1 < t_1 < \ldots < t_{n+1} = 1$), be the preimages of points z_k, and τ_j, where $j = 1, 2, 3, 4$, be the preimages of vertices $w_j \in \partial D^*$. Each τ_j obviously coincides with one of t_k.

In this case, the derivative $\frac{dz}{d\zeta}$ of the conformal mapping z: $E \longrightarrow D(P)$ satisfies the boundary value problem [3–8]

$$\arg\frac{dz}{dt} = \pi\bar{\theta}(t), \quad |t| < 1; \quad \operatorname{Re}\frac{dz}{dt} = h(t), \quad |t| > 1. \quad (1)$$

Here, $h = N\prod_{j=1}^{4}|t - \tau_j|^{-1/2} \equiv \left|\frac{dw}{dt}\right|$, $N = \text{const}$, $\bar{\theta} = \bar{\delta}_k$, and $t \in [t_k, t_{k+1}]$, $\pi\bar{\delta}_k$ is the angle between the kth side of the polygon P and the Ox axis.

Some filtration flows of an incompressible liquid that have contact (free) boundaries with immobile liquids of different densities (water–air, sweet water–salt water) are also described by boundary conditions (1), where $h = q(t)\left|\frac{dw}{dt}\right|$ for $|t| > 1$, $q(t) = 1$ on the preimages of the free boundaries and $q(t) = 0$ on the preimage of the horizontal drain [6]. The technique given in this study is also applicable to such filtration problems.

The solution of the Hilbert boundary value problem given by Eq. (1) is represented in the form

$$\frac{dz}{d\zeta} = \frac{\Pi(\zeta)}{\pi i}\int_{|t|>1}\frac{h(t)dt}{\Pi(t)(t-\zeta)} \equiv \Pi(\zeta)M(\zeta), \quad (2)$$

Lavrent'ev Institute of Hydrodynamics, Siberian Division, Russian Academy of Sciences, pr. Akademika Lavrent'eva 15, Novosibirsk, 630090 Russia

1028-3358/05/5009-0478$26.00 © 2005 Pleiades Publishing, Inc.

where

$$\Pi(\zeta) = \prod_{k=0}^{n+1}(\zeta - t_k)^{\beta_k}, \quad \beta_k = \alpha_k - 1, \quad \sum_{k=0}^{n+1}\beta_k = -1.$$

Canonical solution $\Pi(\zeta)$ of the homogeneous problem given by Eq. (1) ($h \equiv 0$) is the derivative of the conformal mapping Z: $E \longrightarrow D(\bar{P})$, $\Pi = \dfrac{dZ}{d\zeta}$ of the upper half-plane onto a domain bounded by a polygon $\bar{P} = P \cup P_0 \cup P_{n+1}$, where P_0 and P_{n+1} are rays that are parallel to the Oy axis and begin at the vertices z_0, z_{n+1} of the polygon P.

Each vector $T = (t_1, t_2, \ldots, t_n)$ ($N = 1$, $t_0 = -1$, and $t_{n+1} = 1$) appearing in Eq. (2) corresponds to a certain polygon $P(T)$ with links $P_k(T)$ parallel to $P_k \subset P$. The desired constants t_k, where $k = 1, 2, \ldots, n$, are determined from the following conditions of coincidence of $P(T)$ with given P:

$$l = g(T, \beta); \quad l = (l_1, l_2, \ldots, l_n), \quad \beta = (\beta_0, \beta_1, \ldots, \beta_{n+1}), \tag{3}$$

where

$$l_k = \int_{t_{k-1}}^{t_k} |\Pi(t)||M(t)|dt \text{ for } k = 1, 2, \ldots, n.$$

Since the drainage-domain width $|z_{n+1} - z_n| = y_{n+1} - y_n > 0$ (z_n is fixed and $\mathrm{Im} z_{n+1} = y_{n+1}$ is unknown) is unknown in problems of the filtration of the liquid through embankment dams, Eqs. (3) completely determine the geometry of the polygon P, and the system of equations (3) corresponding to P is solvable with certainty, as was proved in [4–8].

2. THE CURVILINEAR BOUNDARY

Our goal is to construct a certain Lyapunov curve $\Gamma(\mu) \subset C^{\alpha+1}$ for which $\alpha > 0$ and $\mu > 0$ is the approximation parameter that approximates the polygon P so that the explicit representation of form (2) is valid for the derivative $\dfrac{dz}{d\zeta}$ of the conformal mapping z: $E \longrightarrow D(\Gamma)$, $\partial D(\Gamma) = \Gamma \cup L$. We introduce the notation $t_k^{\pm} = t_k \pm r_k$, $r_k(\mu) = \mu \inf\{(t_k - t_{k-1}), (t_{k+1} - t_k)\}$, $k = 1, 2, \ldots, n+1$, $0 < \mu \le \dfrac{1}{3}$, $t_0^{\pm} = t_0 = -1$: $t_{n+1}^- = t_{n+1} = 1$, $\Delta_k = [t_k^-, t_k^+]$, $\Delta_k^+ = [t_k^+, t_{k+1}^-]$, and consider the function $\theta(t) = \bar{\theta}(t) - 1$: $\theta(t) = \delta_k \pi$, $t \in \Delta_k^+$; $\theta = 0$, $|t| > 1$;

$$\theta = [\delta_k(t - t_k^-) + \delta_{k-1}(t_k^+ - t)]|\Delta_k|^{-1} \equiv \theta_k(t), \quad t \in \Delta_k,$$

where $\delta_k = \bar{\delta}_k - 1$. The constructed function $\theta(t, \mu)$, where $|t| < 1$, is continuous and uniformly bounded for any arbitrary values $(t_{k+1} - t_k) \ge 0$, $k = 0, 1, \ldots, n$, $|\theta| \le \sup_k |\delta_k|$.

The canonical function $\Pi_\theta(\zeta)$ of the homogeneous problem given by Eq. (2) with the chosen function $\theta(t)$ is calculated using Gakhov's formula (see [3], p. 42)

$$\Pi_\theta(\zeta) = (1 - \zeta^2)^{-1/2}\exp\left(\int_{-1}^{1}\frac{\theta(t, \mu)dt}{t - \zeta}\right) \tag{4}$$

and is the derivative of the conformal mapping

$$Z = \int_{-1}^{\zeta}\Pi_\theta(\zeta)d\zeta, \quad Z: E \to D(\bar{\Gamma}),$$
$$\bar{\Gamma}(\mu) = \Gamma \cup P_0 \cup P_{n+1}.$$

The domain $D(\bar{\Gamma})$, which is a half-strip, is bounded by a certain approximating curve $\Gamma(\mu)$, whose tangent has the slope angle $\pi\bar{\theta}(t)$ to the Ox axis, and rays P_0 and P_{n+1} introduced in the first section. Calculating the Cauchy integral appearing in Eq. (4), we arrive at the following representation for the function $\Pi_\theta(\zeta)$ with an arbitrary extension constant:

$$\Pi_\theta = (1 - \zeta^2)^{-1/2}\prod_{k=0}^{n}\left(\frac{t_k^+ - \zeta}{t_k^- - \zeta}\right)^{\gamma_k(\zeta)}\left(\frac{t_{k+1}^- - \zeta}{t_k^+ - \zeta}\right)^{\delta_k}. \tag{5}$$

Here, $\gamma_k = (a_k + b_k\zeta)|\Delta_k|^{-1}$, $a_k = t_k^+\delta_{k-1} - \delta_k t_k^-$, $b_k = \delta_k - \delta_{k-1}$, $k = 1, 2, \ldots, n$, $\gamma_0 = 0$, $t_0^{\pm} = t_0 = -1$, $t_{n+1}^- = t_{n+1} = 1$, $|\Delta_k| = (t_k^+ - t_k^-)$, $k = 1, 2, \ldots, n$.

By the construction, $\theta(t, \mu) \longrightarrow \delta_k$, for $t \in [t_{k-1}, t_k]$ and $\mu \longrightarrow 0$, and the curve $\Gamma(\mu)$ is reduced to the given polygon P, and the derivative $\dfrac{dz}{d\zeta}(\mu) = \Pi_\theta(\zeta)M_\theta(\zeta)$ of the conformal mapping z: $E \longrightarrow D(\Gamma)$ is represented in the form of Eq. (2) with $\Pi(\zeta) = \prod_{k=0}^{n+1}(\zeta - t_k)^{\beta_k}$.

Similar to the problem for a polygon, we consider Eq. (3) for determining the vector $T = (t_1, t_2, \ldots, t_n)$, where

$$g_k(T, \beta) = \left| \int_{t_{k-1}}^{t_k} \Pi_\theta(t) M_\theta(t) dt \right| = |z_k - z_{k-1}|, \quad k = 1, 2, \ldots, n. \tag{6}$$

Here, M_θ in Eq. (2) is calculated in terms of $\Pi_\theta(\zeta)$ given by Eq. (5).

The definition of the curve $\Gamma(\mu)$ contains the *given* geometric characteristic (l, β), where $l = (l_1, l_2, \ldots, l_n)$ and $\beta = (\beta_0, \beta_1, \ldots, \beta_{n+1})$ of the basic polygon P with which $\Gamma(\mu)$ coincides for $\mu = 0$. It is assumed that the vector (l, β) satisfies the conditions under which the polygon P is nondegenerate [4–8]

$$|\ln l_k| \le \delta^{-1}, \quad \delta - 1 \le \beta_k \le 1, \quad k = 1, 2, \ldots, n;$$

$$-\frac{1}{2} \le (\beta_0, \beta_{n+1}) \le \frac{1}{2} - \delta, \quad \delta > 0.$$

The conformal mapping

$$z = \int_{-1}^{\zeta} \Pi_\theta(\zeta) M_\theta(\zeta) d\zeta \equiv F_\theta(\zeta), \quad F_\theta: E \longrightarrow D(\Gamma)$$

transforms t_k, where $k = 0, 1, \ldots, n+1$, into the points $z_k(\mu) = F_\theta(t_k) \in \Gamma(\mu)$ that are the vertices of a certain polygon $P(\mu)$ approximated by the curve $\Gamma(\mu)$. In this case, the lengths $l_k(\mu)$ of the sides of $P_k(\mu)$ coincide with the respective lengths l_k of the sides of P, whereas the exterior angles $\pi\beta_k(\mu)$ generally differ from the respective exterior angles $\pi\beta_k$.

An arbitrary vector T substituted into Eq. (3) corresponds to a certain curve $\Gamma(\mu, T)$ approximating the polygon $P(\mu, T)$. Equations (3) are the conditions of the coincidence of $\Gamma(\mu, T)$ with $\Gamma(\mu)$ and, therefore, the coincidence of $P(\mu, T)$ with $P(\mu)$.

3. *A PRIORI* ESTIMATES OF SOLUTIONS TO THE PROBLEM ON PARAMETERS

Let us prove that the desired constants t_k, where $k = 1, 2, \ldots, n$, in Eq. (3) satisfy the *a priori* estimates

$$t_{k+1} - t_k \ge \varepsilon > 0, \quad k = 0, 1, \ldots, n, \tag{7}$$

where $\varepsilon = \varepsilon(\delta)$ is the function of a single constant δ in the definition of the nondegenerate polygon P [4].

Let τ_k, where $k = 1, 2, 3, 4$, be the preimages of the vertices of the rectangle ∂D^* in the conformal mapping $w: E \longrightarrow D^*$. We define τ_k as follows: $\tau_1 = t_0 = -1$, $\tau_2 = t_s$, $\tau_3 = t_m$, $\tau_4 = t_{n+1} = 1$, $0 < s < m < n + 1$. In this case, using the method of the extreme lengths of families of curves [8], we obtain

$$\tau_{k+1} - \tau_k \ge \varepsilon > 0, \quad k = 1, 2, 3,$$

i.e., the rectangle ∂D^* is nondegenerate.

To prove estimates (7) for the remaining t_k ($k = 0, 1, \ldots, n+1$), we assume that the opposite property is valid, i.e., that a part of them can approach each other. In view of Eq. (7) for τ_k, constants $t_s = \tau_2$ and $t_m = \tau_3$ cannot simultaneously be approaching parameters. Let $t_0 = -1$ and $t_{n+1} = 1$ be absent among approaching parameters t_k; i.e., $1 - t_k^2 \ge \xi > 0$, where $k = 1, 2, \ldots, n$.

Substituting $\Pi_\theta(t)$, where $|t| > 1$, in the form

$$\Pi_\theta = \prod_{k=0}^{n} \left(\frac{t_k^+ - t}{t_k^- - t} \right)^{\gamma_k} \left(\frac{t_{k+1}^- - t}{t_{k+1} - t} \frac{t_k - t}{t_k^+ - t} \right)^{\delta_{kn+1}} \prod_{k=0}^{\beta_k} (t_k - t)^{\beta_k},$$

we arrive at the relation

$$|M_\theta(\tau)| = \frac{1}{\pi} \int_{|t|>1} \frac{h(t) dt}{|\Pi_\theta(t)||t - \tau|}, \quad |\tau| \le 1,$$

which provides the inequalities

$$0 < a \le |M_\theta(\tau)| \le K(\xi), \quad |\tau| \le 1 - \xi, \quad \xi > 0.$$

Let constants t_k, $k = \nu, \nu + 1, \ldots, p$, $0 < \nu < p < m$ be approaching parameters. The second possible case $s < \nu < p < n + 1$ is similarly considered ($t_s = \tau_2 \ne \tau_3 = t_m$). We set $2r = t_p^+ - t_\nu^-$ and $t_* = t_\nu + r$ and consider semicircle $K_r = \{|\zeta - t_*| = r, \operatorname{Im}\zeta > 0\}$. In this case,

$$r \le |t_k^\pm - \zeta| < 2r, \quad k = \nu, \nu + 1, \ldots, p \text{ for } \zeta \in K_r.$$

For $r \ll 1$, the inequalities $|t_k^\pm - \zeta| \ge \xi > 0$ are valid at $k = 0, 1, \ldots, \nu - 1$ and at $k = p + 1, p + 2, \ldots, n + 1$. Taking into account the latter inequalities, we obtain

$$|\Pi_\theta(\zeta)| \le C \prod_{k=\nu}^{p} |R_k|, \quad R_k = \left(\frac{t_k^+ - \zeta}{t_k^- - \zeta} \right)^{\beta_k/q_k},$$

$$q_k = \frac{|\Delta_k|}{t_k^- - \zeta},$$

where $\beta_k\pi = (\delta_{k-1} - \delta_k)\pi$ is the exterior angle in the vertex $z_k \in P$. Thus,

$$|R_k| \le C_0 \left| (1 + q_k)^{\beta_k/q_k} \right|.$$

If $q_k(t) \longrightarrow 0$ for $r \longrightarrow 0$, then

$$\lim_{r \to 0}(1 + q_k)^{\beta_k/q_k} = e^{\beta_k}, \quad |R_k| \le C_1 < \infty.$$

If $|q_k| \ge a > 0$ for $\forall r \ll 1$, then $|R_k| \le C_3 < \infty$ and, thereby, $|\Pi_\theta(\zeta)| \le C_4$, $\zeta \in K_r$.

We consider the curve $F_\theta(K_r) \equiv \Lambda_r$ that is the image of a semicircle, lies in the domain $D(\Gamma)$, and connects inner points $(z_\nu^*, z_p^*) \in \Gamma$, $|z_p^* - z_\nu^*| \ge \xi > 0$.

The length of the curve Λ_r is estimated as

$$|\Lambda_r| = \left|\int_{K_r} \frac{dF_\theta}{d\zeta} d\zeta\right| \le \pi C_5 r.$$

Therefore, $|\Lambda_r| \longrightarrow 0$ for $r \longrightarrow 0$. Thus, $l_k = |z_k - z_{k-1}| \longrightarrow 0$, where $k = \nu + 1, \nu + 2, \ldots, p$, which contradicts the condition that the basic polygon P is nondegenerate.

We now assume that, e.g., t_0 and $2r = (t_p^+ - t_0) \longrightarrow 0$, where $0 < p < m$, are among approaching parameters. Let $K_r = \{|\zeta - t_*| = r, \operatorname{Im}\zeta > 0\}$, $t_* = t_0 + r$. We represent $\Pi_\theta(\zeta)$ in the form

$$\Pi_\theta(\zeta) = (1 + \zeta)^{\beta_0}\prod_{k=1}^{p} R_k \Pi_*(\zeta), \quad |\ln \Pi_*| \le C_7,$$

where $R_k = (1 + q_k)^{\beta_k/q_k}$ and $q_k = |\Delta_k|\,(t_k^- - \zeta)^{-1}$. As above, $|R_k| \le C_3$ for $\zeta \in K_r$, and, therefore,

$$|\Pi_\theta(\zeta)| \le C_8|1 + \zeta|^{\beta_0} - \frac{1}{2} < \beta_0 \le 0.$$

Similarly, for $\zeta = t \in L_1$, where $L_1 = (-2, -1 - r)$ with $0 < r \ll 1$, we have

$$h(t)\left|\Pi_\theta^{-1}(\zeta)\right| \equiv \rho(t)(1 + t)^{-\beta_0}, \quad \rho(t) \le C_9.$$

We set

$$M_r(\zeta) = \left(\int_{L_1} + \int_{L_2}\right)\frac{\rho(t)(1 + t)^{-\beta_0} dt}{t - \zeta} \equiv M_r^1 + M_r^2,$$

where $L_2 = (-\infty, -2) \cup (1, \infty)$.

Then, for $\zeta \in K_r$ we obtain

$$\left|M_r^2\right| \le C_{10}; \quad \left|M_r^1\right| \le C_{11}|1 + \zeta|^\delta, \quad 0 < \delta \ll 1 \quad (\delta = 0 \text{ for } \beta_0 < 0);$$

$$|\Lambda_r| = \left|\int_{K_r} \Pi_\theta M_r d\zeta\right| \le C_{12} r^{1/2 - \delta}.$$

Thus, $|\Lambda_r| \longrightarrow 0$ as $r \longrightarrow 0$, which contradicts the nondegeneracy of P. A similar estimate for the integral

$$I_r = \int_{-1-r}^{-1} |\Pi_\theta||M_r| dt$$

shows that $I_r \longrightarrow 0$ as $r \longrightarrow 0$. The case in which $2r = (t_{n+1}^- - t_\nu^+) \longrightarrow 0$, for $m \le \nu \le n$ is similar to the above case. Thus, the validity of *a priori* estimates (7) has been proved.

4. SOLVABILITY OF THE PROBLEM

Similar to [3], after reducing integration intervals in Eq. (6) to [0, 1], the functions $g_k(T, \beta)$ are continuously differentiable with respect to t_i, where $i = 1, 2, \ldots, n$.

We set $u_k = t_{k+1} - t_k$, where $k = 1, 2, \ldots, n$, and transform Eq. (3) with $g = (g_1, g_2, \ldots, g_n)$ written as (6) to the form

$$u = f(u, l, f), \quad f_k = l_k^{-1} u_k g_k(T, \beta), \tag{8}$$

where the vectors T and u are unambiguously expressed in terms of each other.

A priori estimates (7) for Eq. (8) can be represented in the form of the implication

$$u \in \Omega(\varepsilon) = \{u | u_k \ge \varepsilon, k = 1, 2, \ldots, n\}. \tag{9}$$

Since the operator f: $R^n \longrightarrow R^n$, which is continuously differentiable on the set $\Omega(\omega)$ and at its boundary, has no stationary points in view of Eq. (9), Eq. (8) has at least one solution according to the Shauder theorem. Thus, the following statement has been proved.

Theorem (of existence). *Let the basis polygon P be nondegenerate. Then, Eq.* (8) *for the corresponding curve* $\Gamma(\mu)$ *has at least one solution* $u = (u_1, u_2, \ldots, u_n)$ *belonging to the set* $\Omega(\varepsilon)$ *as defined in Eq.* (9).

ACKNOWLEDGMENTS

This work was supported by the Russian Foundation for Basic Research, project no. 05-01-00131.

REFERENCES

1. P. Ya. Polubarinova-Kochina, *Theory of Groundwater Flow* (Nauka, Moscow, 1977) [in Russian].
2. P. Ya. Polubarinova-Kochina, V. G. Pryazhinskaya, and V. N. Émikh, *Mathematical Methods in Irrigation Problems* (Nauka, Moscow, 1969) [in Russian].
3. V. N. Monakhov, *Boundary Value Problems with Free Boundaries for Elliptic Systems of Equations* (Nauka, Novosibirsk, 1977; Am. Math. Soc., Providence, 1983).
4. V. N. Monakhov, Sib. Mat. Zh. **41** (5), 106 (2000).
5. E. V. Gubkina and V. N. Monakhov, Prikl. Mekh. Tekh. Fiz. **41** (5), 188 (2000).
6. V. N. Monakhov, Prikl. Mekh. Tekh. Fiz. **42** (5), 98 (2001).
7. V. N. Monakhov, Sib. Mat. Zh. **43** (3), 629 (2002).
8. E. V. Gubkina and V. N. Monakhov, Prikl. Mekh. Tekh. Fiz. **44** (1), 83 (2003).

Translated by R. Tyapaev